Performance Studies of CMS Resistive Plate Chambers at $\sqrt{s} = 13\ TeV$ and Measurement of Inclusive $t\bar{t}$ Cross section at $\sqrt{s} = 5.02\ TeV$

by

Mehar Ali Shah

SUBMITTED IN PARTIAL FULFILLMENT OF THE
REQUIREMENTS FOR THE DEGREE OF
PHILOSOPHY OF DOCTORATE
AT
QUAID-I-AZAM UNIVERSITY
ISLAMABAD, PAKISTAN
DECEMBER, 2018

Author's Declaration

I Mehar Ali Shah hereby state that my Ph.D thesis titled "**Performances Studies of CMS Resistive Plate Chambers at $\sqrt{s}$ = 13 *TeV* and Measurement of Inclusive $t\bar{t}$ Cross section at $\sqrt{s}$ = 5.02 TeV**" is my own work and has not been submitted previously by me for taking any degree from this university Quaid-i-Azam University, Islamabad or any else in the country/world.

Any time if my statement is found to be incorrect even after my Graduate the university has the right to withdraw my Ph.D. degree.

Mehar Ali Shah

December 28, 2018

Plagiarism Undertaking

I solemnly declare that research work presented in the thesis titled "**Performances Studies of CMS Resistive Plate Chambers at $\sqrt{s}$ = 13 *TeV* and Measurement of Inclusive $t\,\bar{t}$ Cross section at $\sqrt{s}$ = 5.02 TeV**" is solely my research work with no significant contribution from any other person. Small contribution/help wherever taken has been duly acknowledged and that complete thesis has been written by me.

I understand the zero tolerance policy of the HEC and Quaid-i-Azam University Islamabad towards plagiarism. Therefore, I as an Author of the above titled thesis declare that no portion of my thesis has been plagiarized and any material used as reference is properly referred/cited.

I undertake that if I am found guilty of any formal plagiarism in the above titled thesis even after award of Ph.D. degree, the university reserves the rights to withdraw/revoke my Ph.D. degree and that HEC and the University has the right to publish my name on the HEC/University Website on which names of students are placed who submitted plagiarized thesis.

Student/Author Signature: 

Name: Mehar Ali Shah

Certificate of Approval

This is to certify that the research work presented in this thesis, entitled "**Performances Studies of CMS Resistive Plate Chambers at $\sqrt{s}$ = 13 *TeV* and Measurement of Inclusive $t\bar{t}$ Cross section at $\sqrt{s}$ = 5.02 TeV**" was conducted by Mr. Mehar Ali Shah under the supervision of Dr. Shamona Fawad Qazi.

No part of this thesis has been submitted anywhere else for any other degree. This thesis is submitted to the Department of Physics, Quaid-i-Azam University Islamabad, Pakistan in partial fulfillment of the requirements for the degree of Doctor of Philosophy in Field of Experimental High Energy Physics, Department of Physics Quaid-i-Azam University Islamabad.

Student Name: **Mr. Mehar Ali Shah** Signature:_____

Examination Committee:

a) Dr. Farida Tahir,
Department of Physics,
COMSATS University,
Chak Shahzad, Islamabad. Signature:_____

b) Dr. Rizwan Khalid,
Assistant Professor,
School of Natural Sciences (SNS),
NUST, Islamabad. Signature:_____

c) Prof. Dr. Arif Mumtaz
Chairman,
Department of Physics
QAU, Islamabad. Signature:_____

Dr. Shamona Fawad Qazi
Supervisor, Signature:_____

Prof. Dr. Hafeez R. Hoorani
Co-supervisor, Signature:_____

Chairman Signature:_____

To my family.

Abstract

The CMS experiment at the CERN Large Hadron Collider (LHC) has a redundant muon system composed of three different detector technologies: Cathode Strip Chambers (CSC, in the endcap regions), Drift Tubes (DT, in the barrel region), and Resistive Plate Chambers (RPC, both in the barrel and endcap). The RPC are designed mainly as a trigger detector but they contribute to the muon reconstruction as well. Thus the monitoring and analysis of the system performance are necessary and essential for the final data quality. The main detector characteristics and the hit efficiency and cluster size are presented in this thesis. The stability of the system in the conditions of high instantaneous luminosity and high number of pile up (PU) events are presented in a view of history monitoring and stable trend. RPC background, currents and charge was studies in depth with increasing luminosity and data driven estimations of all these parameters are reported at the extreme conditions of High Luminosity LHC (HL-LHC).

First measurement of the top quark pair production cross section ($\sigma_{t\bar{t}}$) in proton proton collisions at a center-of-mass energy of 5.02 TeV is presented as a second part of this document for 27.4 pb^{-1} data collected by the CMS experiment at LHC. The measurements are performed by studying events containing at least one charged lepton. The measured cross section is $\sigma_{t\bar{t}}$= $69.5 \pm 6.1\ (stat) \pm 5.6\ (syst) \pm 1.6\ (lumi)\ pb$, with a total relative uncertainty of 12%. The result is in agreement with the expectation from the standard model. The impact of the presented measurement on the determination of the gluon distribution function is investigated.

Acknowledgment

It is my immense pleasure to acknowledge all my colleagues who have supported me to achieve this milestone, which manifests itself in this thesis.

I would like to thank my supervisor, **Shamona Fawad Qazi** and co-supervisor **Hafeez R Hoorani** , and CMS RPC Collaboration for providing me the extraordinary opportunity to work in the CMS experiment at CERN. Without their support, it was not possible for me to participate in cutting-edge physics and learning from and contributing to the most extra ordinary experiment of the history. I would like to thank also **Higher Education Commission (HEC)** and **CMS RPC collaboration** for providing financial support during my studies.

I would like to say a special thanks to Pierluigi Polucci, Gabriella Pugliese, Roumyana Milevs Hadjiska, S. Buontempo, M. Isabel Pedraza, Mariana Shopova, Karol Bunoski , Anton Dimitrov, Aleksander Aleksandrov, Irfan Asghar Bhutta, Waqar Ahmad, Ashfaq Ahmad, Ahmad Abbasi, Taimoor Khurshid and all other colleagues in EHEP NCP and RPC group for all their technical and moral support during my PhD. I would also like to say thanks to my close friends Saad Sultan, Arshad Abbasi and Qasim Warraich for being my strength and source of motivation during the entire period.

I would like to have a special acknowledgment to CMS TOP group for all support, feedback, and direction that has lead to the results discussed in this thesis. Thanks

to E. Eren, A. Giammanco, J. Gonzalez, Q.-ul-Hassan, G. Krintiras, K. Lipka, E. Palencia, P.Silva, M. Verweij and Muhmammad Gul for their help and support during the analysis.

I would congratulate our colleagues in the CERN accelerator departments for the excellent performance of the LHC and thank the technical and administrative staffs at CERN and at other CMS institutes for their contributions to the success of the CMS effort. In addition, I gratefully acknowledge the computing centers and personnel of the Worldwide LHC Computing Grid for delivering so effectively the computing infrastructure essential to our analyses. Finally, I acknowledge the enduring support for the construction and operation of the LHC and the CMS detector provided by the following funding agencies: BMWFW and FWF (Austria); FNRS and FWO (Belgium); CNPq, CAPES, FAPERJ, and FAPESP (Brazil); MES (Bulgaria); CERN; CAS, MoST, and NSFC (China); COLCIENCIAS (Colombia); MSES and CSF (Croatia); RPF (Cyprus); SENESCYT (Ecuador); MoER, ERC IUT, and ERDF (Estonia); Academy of Finland, MEC, and HIP (Finland); CEA and CNRS/IN2P3 (France); BMBF, DFG, and HGF (Germany); GSRT (Greece); OTKA and NIH (Hungary); DAE and DST (India); IPM (Iran); SFI (Ireland); INFN (Italy); MSIP and NRF (Republic of Korea); LAS (Lithuania); MOE and UM (Malaysia); BUAP, CINVESTAV, CONACYT, LNS, SEP, and UASLP-FAI (Mexico); MBIE (New Zealand); PAEC (Pakistan); MSHE and NSC (Poland); FCT (Portugal); JINR (Dubna); MON, RosAtom, RAS, RFBR and RAEP (Russia); MESTD (Serbia); SEIDI, CPAN, PCTI and FEDER (Spain); Swiss Funding Agencies (Switzerland); MST (Taipei); ThEPCenter, IPST, STAR, and NSTDA (Thailand); TUBITAK and TAEK (Turkey); NASU and SFFR (Ukraine); STFC (United Kingdom); DOE and NSF (USA).

Mehar Ali Shah

Table of Contents

List of Tables

List of Figures

Chapter 1

Introduction

In this thesis the first results of the performance of the RPC muon system during 2015 and 2016 with the LHC running at 13 TeV are presented. The stability of the RPC system performance, in terms of efficiency, cluster size and intrinsic noise after running in extreme conditions is reported. Muons provide a clean signal to detect interesting events over complicated backgrounds at the LHC. The muon spectrometer in the Compact Muon Solenoid (CMS) experiment has the key functions of muon triggering, transverse momentum measurement, muon identification and charge determination. The muon system allows to identify the muons produced in several Standard Model processes, for example top quark decay, W and Z decay, and the well-known Higgs Boson. Therefore a robust and redundant muon system is required to provide efficient muon reconstruction.

The CMS muon system consist of three different technologies namely drift tubes (DT) in the barrel (central) region, cathode strip chambers (CSC) in the endcap region, and resistive plate chambers (RPC) in both the barrel and endcap, and it covers a pseudorapidity region $|\eta| < 2.4$. The DTs and RPCs in the barrel are installed upto eta region $|\eta| < 1.2$, while the CSCs and the RPCs in the end-caps cover the eta region $0.9 < |\eta| < 2.4$. There are 1056 RPC detectors (chambers) installed which cover an area of about 3950 m^2, equipped with about 123,688 readout

channels (strips). The resistive plate chambers are double-gap detectors with gas gap of 2 mm each and copper readout strips placed in between the gaps. The bakelite bulk resistivity of CMS RPC is in the range of 10^{10-12} Ωcm and detectors are operated in avalanche mode with a gas mixture of 95.2% $C_2H_2F_4$, 4.5% iC_4H_{10} and 0.3% SF_6. Radiation background levels, currents and intergrated charge on the entire RPC system have been studied in depth with increasing LHC luminosity and data driven extrapolations to the High Luminosity LHC conditions are reported.

The pair production ($t\bar{t}$) cross section ($\sigma_{t\bar{t}}$) of the top quark: the heaviest elementary particle in the standard model (SM), as a function of center-of-mass energy is of interest for the extraction of the top quark pole mass [17] and can be used to constrain the gluon distribution function at large fractions x of the proton longitudinal momentum carried by the gluon, where the gluon distribution is poorly known. Precise measurements of $\sigma_{t\bar{t}}$ in proton-proton (pp) collisions have been published at $\sqrt{s}$ values of 7 and 8 [18, 9, 10] and 13 TeV [19, 20, 11, 12] by the ATLAS and CMS Collaborations at the LHC.

The analysis presented in this thesis is done using $t\bar{t}$ candidate events with ℓ+jets, where leptons are either electrons or muons, and dilepton final states. In the former case, the cross section is extracted by a fit in different categories, while in the latter a simpler but more robust event-counting experiment approach is used. The two results are then combined in the final measurement. Top-quark pair production probes the gluon distribution in the proton. In particular, $t\bar{t}$ production at $\sqrt{s} = 5.02$ TeV accesses the high-x region at which the gluon distribution is not well understood. Improvements of our understanding of the high x gluon distribution are essential for accurate theoretical predictions for cross sections in the SM interactions and those beyond the SM at hadron colliders. The impact of the $t\bar{t}$ cross section measurement on the uncertainty in the gluon distribution is illustrated through a next-to-next-to leading order (NNLO) QCD analysis.

Chapter 2 provides a brief introduction of the SM, top quark production, its properties and motivation to study the top quark pair production cross section. Chapter 3 provides an in depth overview of the CMS experiment at the LHC. Chapter 4 describes the working principles of resistive plate chambers detectors and avalanche production. Chapter 5 describes the performance results of RPC during 2015, and 2016 data taking at 13 TeV and data driven estimations of current results at HL-LHC conditions. Chapter 6 describes the datasets, both the data and Monte Carlo (MC) samples for the top pair process and event selection procedures. Chapter 7 explains the cross-section measurement of top pair with one charged lepton in the final state and impact of the $t\bar{t}$ cross section measurement on the uncertainty in the gluon distribution through a next-to-next-to leading order (NNLO) QCD analysis.

Chapter 2

Physics at Hadron Colliders

All known matter in the universe is made of atoms - a collection of neutrons and protons and electrons. Quarks and electrons are fundamental particles since they have no sub-structures. Protons and neutrons, on the other hand, can be defined as composite state of quarks and hence are not fundamental particles.

Our present understanding of elementary particle physics is the result of theoretical and experimental progress going hand in hand over the last century. Early on, collisions were an essential asset in the discovery and understanding of particles, starting with the observation of the positron and muon from highly energetic cosmic rays collisions with nuclei in the earth's atmosphere. Soon various accelerators were developed to explore the world of particle physics through an abundance of man-made particle collisions, increasing precision and energies over the years.

A succession of theoretical predictions and experimental discoveries in this area of research led to the development of the Standard Model of Particle Physics (SM) during the sixties and seventies. Ever since, this theory of elementary particles and their interactions has been challenged, and it proved to accurately describe measurements as well as successfully predicted for instance top quark and the tau neutrino's discovery. More recently, a Higgs boson was added to this list [3, 4] using the ATLAS and CMS detectors at the Large Hadron Collider (LHC).

This chapter will provide a short introduction to the main characteristics of the Standard Model of Particle Physics and the challenges it holds. Top quark physics will be shortly explained in the second half of this chapter.

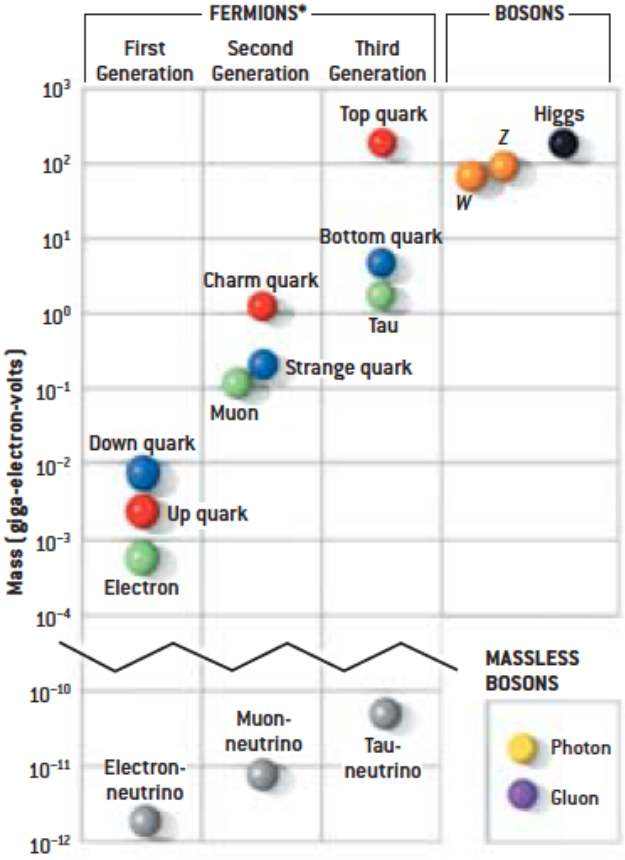

Figure 2.1: Elementary particles and their masses as presented in the Standard Model of Particle Physics [1].

2.1 The Standard Model

The Standard Model of Particle Physics is basically a Quantum Field Theory (QFT) which narrates the known particles and their interactions [21, 22, 23, 24]. Within the SM, all matter consists of fermions, namely the quarks and leptons (Fig. 2.1).

Quarks are commonly found in colorless bound states [25] called hadrons. These spin1/2 particles are grouped in three generations, with particles differing only in mass (Fig. 2.2). Stable matter consists only of particles from the first generation, due to the unstable nature of the heavier variants. Each generation adds two leptons and two quarks to the equation, along with their antiparticles.

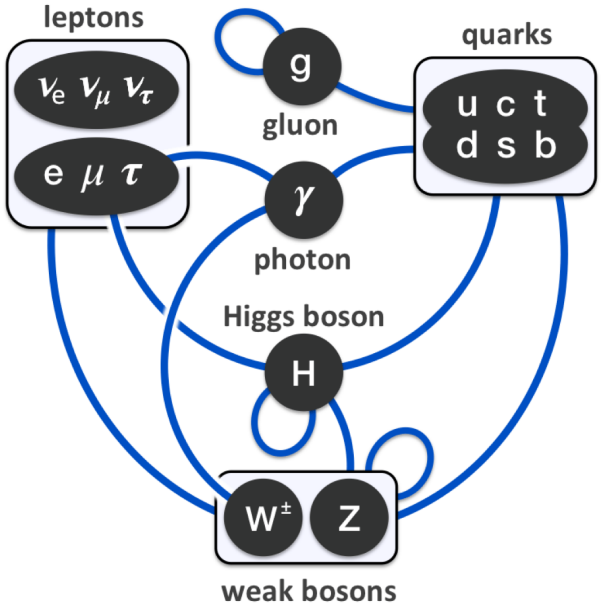

Figure 2.2: Interactions (blue lines) of the fermions (ovals) through the bosons (circles) [2].

The leptons come in six flavours: the first, second and third generations consist of electron and its neutrino (e^-, ν_e), the muon and its neutrino (μ^-, ν_μ), and the tau and its neutrino (τ^-, ν_τ) respectively. For each lepton, there is an antiparticle with opposite charge. The quarks consist of the up and down (u, d) quarks in the first generation, the strange and charm (s, c) in the second, and the bottom and top (b, t) quarks in the third generation.

With the exchange of gauge bosons the fundamental interactions take place between particles that carry an interaction specific charge. A weak isospin charge is

required for the weak interaction and is mediated by the neutral Z^0 and charged W^+ and W^- bosons. The photon (γ) is responsible for the electromagnetic interaction, and interacts with the particles which are electrically charged. Finally, the gluon (g) is the gauge boson for the strong force. Only the the gluon itself and quarks possess the color charge associated with this interaction.

The fourth known fundamental interaction, gravity, is not part of the SM. While it is experienced as a strong force at human scale and above, it becomes negligible at the scale of particle physics experiments when compared to the other three interactions. These particles and interactions are contained in a relativistic Quantum Field Theory. Electroweak (EWK) theory combines the electromagnetic and weak interactions, and Quantum Chromodynamics (QCD) describes the strong interaction. The mass of particles is added to the SM by the electroweak symmetry breaking via Higgs mechanism, which gives rise to the Higgs boson (H) and adds mass to the weak gauge bosons and fermions gain mass through Yukawa couplings with the H boson.

2.2 Beyond the Standard Model

While successful at the observed collision energy ranges, there is a general consensus that the Standard Model of Particle Physics can't be the ultimate description of nature. From a somewhat aesthetic point of view, many physicists believe a unified theory should exist from which the known interactions emerge after spontaneous symmetry breaking. While the SM establishes this for the electromagnetic and weak interactions, no theory has been devised to add the strong interactions. At present the gauge couplings do not meet at higher energies, making unification impossible in this framework. Also the gravitational interaction should be added from this point of view, as its strength becomes relevant towards the Planck scale ($O(10^{19}$ GeV)).

SM Higgs introduction also opens the fear for excessive fine-tuning to constrain the

Higgs mass's quantum corrections which is known as the famous Hierarchy problem. Also from other fields challenges to the SM arise: astrophysical and cosmological measurements strongly suggest the actuality of dark energy and dark matter. Neither can at present be explained using the constituents of the SM. Inspired by these known challenges, several theories have been devised to extend or replace the SM. As an example, a promising set of models considers a broken Super Symmetry (SUSY).With the introduction of these bosons, previously mentioned quantum corrections to the Higgs boson mass would cancel out naturally, solving the Hierarchy problem. It also provides the means to unify the strong and electroweak interactions. Like other theory candidates, it comes with a spectrum of new particles, including some dark matter candidates. One of the key purpose of the Large Hadron Collider and its experiments is to probe for the range of new particles that are introduced with these theories, through their discovery or their influence on known interactions.

2.3 Top Physics

To date, top quark is the heaviest elementary particle in the SM which was observed by the CDF [26] and D0 [27] Collaborations at the Tevatron collider in 1995 in Chicago. From the combined measurements of the Tevatron and LHC experiments, the present most precise determination of the top mass is $m_t = 173.3$ [28]. Life time of top quark is $\approx 10^{-25}$ sec, that is an order of ten less than the time needed for hadrons formation. Therefore, it decays before forming any bound states. Thus the study of its decay provides a unique chance of exploring quasi-free quarks.

The production of top quark , its decays and few more features have been described briefly in the next sections.

2.4 The Top Quark Production

Single top quark production and $t\bar{t}$ production are two major processes responsible for top quark production in the hadron colliders. Production processes of single top quark at leading order are mediated by the electroweak interaction while the $t\bar{t}$ production is characterized by a larger cross section and is mainly induced by the strong force as a result of annihilation of $q\bar{q}$ and gluon-gluon fusion.

2.4.1 Top Quark Pair Production

The $t\bar{t}$ pair production through quarks annihilation ($q\bar{q} \rightarrow t\bar{t}$) and gluon-gluon fusion ($gg \rightarrow t\bar{t}$) are shown in Fig. 2.3. The gluon-gluon fusion is a dominant channel in LHC. In the QCD perturbative expansion the production of top quark pair by

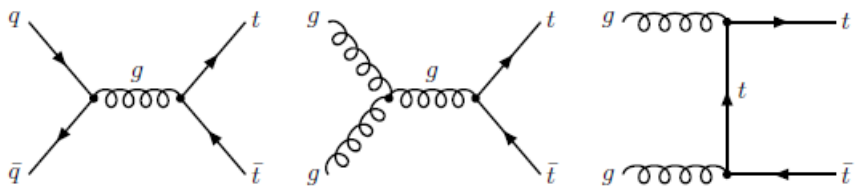

Figure 2.3: Feynman diagrams of leading Order (LO) top quark pair production: (left) illustrate quark-antiquark annihilation, (middle) and (right) illustrate gluons fusion.

quark-gluon scattering process ($qg/\bar{q}g \rightarrow t\bar{t}$) only appears in the Next to Leading Order (NLO) terms . The inclusive $t\bar{t}$ cross section at 8 TeV center-of-mass energy using pp collisions, exploiting the Next-to-Next-to-Leading Order (NNLO) accuracy, has been calculated as, $\sigma_{tt^-} = 245.8\_^{+8}{}_{10}{}^{.8}{}_{.6}\, pb$ [29], using 173.3 GeV top quark mass. While, by resuming the soft-gluon emission processes near the partonic production threshold, the differential production cross-sections is calculated up to approximate NNLO accuracy[30].

2.4.2 Top Quark Properties

Top quark has shorter lifetime ($\approx\ 10^{-25}$ sec) and very large mass as compared to the characteristic QCD hadronization scale. Top quark is the only quark that decays before making any bound state, thus provides the opportunity to study it in bare state. Top quark decays via electroweak process to a W boson and a quark is shown in the equation 2.4.1 below.

$$t \rightarrow q + W^{+}(q = d, s, b) \tag{2.4.1}$$

where q can be a d (down type) quark. Since $V_{td} < V_{ts} << V_{tb}$, allows the top quark to decay into W boson and a bottom quark (approximately 99.8%) (see Fig. 2.4). Hence $t \rightarrow b + W^{+}$ is the dominant decay mode of the top quark in SM. Any observed deviation could be a major hint about the fourth generation of quarks. The top quark's total decay rate is given by the following formula

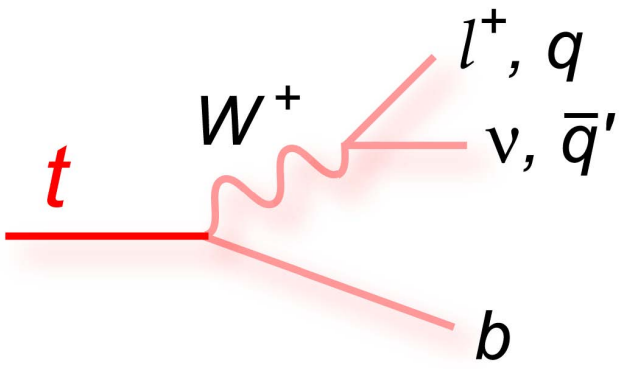

Figure 2.4: The top quark decay

$$\Gamma(t \rightarrow Wb) = \frac{G_F m_t^3}{8\sqrt{(2\pi)}}(1 - \frac{m_W^2}{m_t^2})^2(1 + 2\frac{m_W^2}{m_t^2}), \tag{2.4.2}$$

here G_F is the Fermi constant. The top quark total decay width (Γ_t) with the

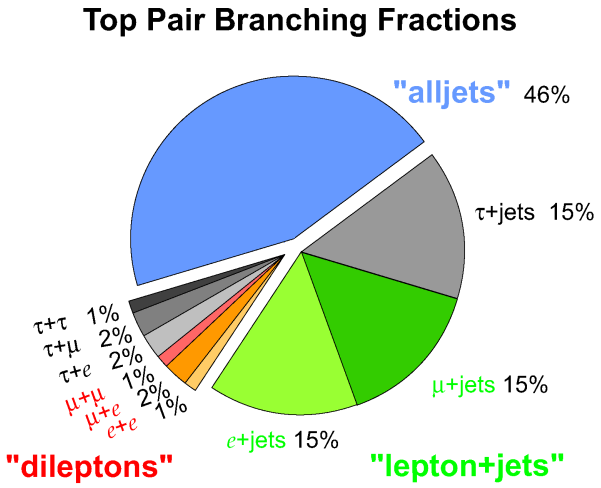

Figure 2.5: The branching ratio of the top quark in different decay channels.

experimentally measured value of top mass $m_t = 173.3$ GeV and $m_W = 80.37$ GeV is

$$\Gamma_t = 1.5\ GeV \tag{2.4.3}$$

Most allowed decays in the SM, with the exception of the $t \to Wb$ decay, are rare and quite arduous to identify by experimentation.

In the global electroweak fits, top quark mass is used as input variable which probe the self consistency of the SM and its value has inference to the stability of the SM vacuum [31]. The top quark's mass is a key parameter of the SM which places constraints on the mass of Higgs boson and electroweak symmetry breaking.

The top quark spin has been measured to be 1/2 using the angular momentum

conservation and the well-measured spins of the *bottom*-quark and the vector boson. Given the fact that top quark doesn't hadronize, spin polarization and correlation are passed to the decay products resulting in characteristic angular distributions. The strength of the spin correlation measured by ATLAS and CMS comes out to be $A^{SM}_{helicity} = 0.34^{+0.15}_{-0.11}$ [32] and $A^{SM}_{helicity} = 0.24^{+0.02}_{-0.08}$ [33] respectively. Both results are well in agreement within the uncertainties with the SM prediction $A^{SM}_{helicity} = 0.31$.

2.5 Motivation of top analysis at 5.02 TeV

The pair production ($t\bar{t}$) cross section ($\sigma_{t\bar{t}}$) of the top quark (the heaviest elementary particle in the SM) as a function of center-of-mass energy is of interest for the extraction of the top quark pole mass [17] and can be used to constrain the gluon distribution function at large fractions x of the proton longitudinal momentum carried by the gluon, where the gluon distribution is poorly known. Precise measurements of $\sigma_{t\bar{t}}$in proton-proton (pp) collisions have been published at $\sqrt{s}$ values of 7 TeV, 8 TeV [18, 9, 10] and 13 TeV [19, 20, 11, 12] by the ATLAS and CMS Collaborations at the LHC

In November 2015, LHC delivered pp collisions at center of mass energy of 5.02 TeV. The fraction of $t\bar{t}$ events initiated by gluon-gluon collisions grows monotonically with $\sqrt{s}$. It is around 73% at 5.02 TeV, as calculated with *POWHEG* (v2) [34, 35] at next-to-leading order (NLO) using the NNPDF3.0 NLO [14] parton distribution functions (PDFs), and increases to around 86% at 13 TeV, making this new data set partially complementary to the higher-energy samples. Measurements of $t\bar{t}$ production at various $\sqrt{s}$ probe different values of x and thus can provide complementary information on the gluon distribution. In addition, future measurements of $\sigma_{t\bar{t}}$ in nuclear collisions at the same nucleon-nucleon center-of-mass energy [36, 37] would profit from

the availability of a reference measurement in pp collisions at $\sqrt{s}$= 5.02 TeV, without the need to extrapolate from measurements at different $\sqrt{s}$. This has already been demonstrated with the first observation of the $t\bar{t}$ process using proton-nucleus collisions at a higher nucleon-nucleon center-of-mass energy.

Top quarks in pp collisions are commonly produced in $t\bar{t}$ pairs. Each top quark eventually decays to a W boson and a bottom (b) quark. The $t\bar{t}$ events are categorized in accordance with the decay of the two W bosons which it decays into. In $t\bar{t}$ events where one of the W bosons decays leptonically and the other hadronically (ℓ+jets channel), the final state contains a signature of one isolated lepton, missing transverse momentum, two jets from the W boson hadronic decay, and two jets coming from the hadronization of the b quarks ("b jets"). On the other hand, in $t\bar{t}$ events where both W bosons decay leptonically (dilepton channel), the final state represents two leptons of opposite electric charge, missing transverse momentum, and at least two b jets. The ℓ+jets channel has a large branching ratio with a moderate amount of background, while the dilepton channel is characterized by a high purity, thus compensating for its smaller branching ratio.

The analysis presented in chapter 7 is done using $t\bar{t}$ candidate events with ℓ+jets, where leptons are either electrons or muons, and dilepton final states. In the former case, the cross section is extracted by a fit in different categories, while in the latter a simpler but more robust event-counting experiment approach is used. The two results are then combined in the final measurement. Top-quark pair production probes the gluon distribution in the proton. In particular, $t\bar{t}$ production at $\sqrt{s}$ = 5.02 TeV accesses the high-x region at which the gluon distribution is not well understood. Improvements of our understanding of the high x gluon distribution are essential for accurate theoretical predictions for cross sections in the SM interactions and those beyond the SM at hadron colliders. The impact of the $t\bar{t}$ cross section measurement on the uncertainty in the gluon distribution is illustrated through a next-to-next-to

leading order (NNLO) QCD analysis.

Chapter 3

The Compact Muon Solenoid(CMS) Experiment

The studies of the performance of Resistive Plate Chambers and $t\bar{t}$ cross section measurements reported in this document were done by using data taken by CMS detector. In this chapter the detector and its components will be described in some detail and the emphasis will be made on the muon system.

3.1 Large Hadron Collider(LHC) at CERN

Installed in the tunnels of the former Large Electron-Positron Collider (LEP) accelerator at the European Organization for Nuclear Research (CERN) (Geneva, Switzerland), the Large Hadron Collider (LHC) accelerates two proton beams in opposite directions along a 26.7 km path, some 100 m underground.

3.1.1 A Discovery Machine

Considering the challenges the SM poses at present, the Large Hadron Collider was designed as a discovery machine. This implies colliding at high energy, to increase the cross section for the heavy resonances. The loss of energy through synchrotron radiation excludes the use of the lighter electron and positron for this purpose. Using

protons does however mean that the collisions have complex final states: the partons taking part only carry a variable fraction of the proton momentum leading to interactions of variable center-of-mass energy. The use of proton-proton collisions (pp), rather than proton-antiproton ($p\bar{p}$), allows for high intensity beams, increasing the collision rates and as such decreasing the minimal cross section that can be probed.

The LHC cannot accelerate the protons from the ground up. Instead, it relies on a chain of accelerators present at CERN (see Fig.3.1). Fig.3.2 shows cross sections and production rates of some interesting processes as a function of the center-of-mass energy.

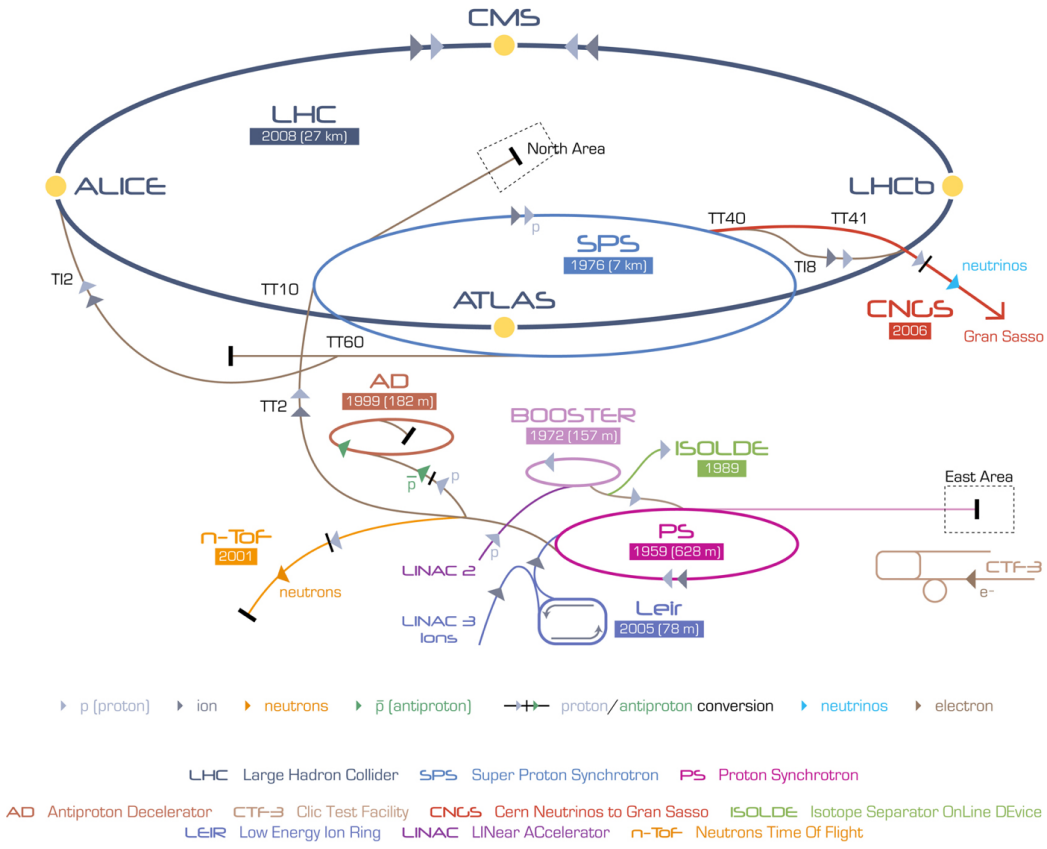

Figure 3.1: Overview of the CERN accelerator complex [3]

The LHC finally accelerates the beams in separate beam pipes for each direction

to a maximum energy of 6.5 TeV per proton, before starting collisions with a center-of-mass energy of up to $\sqrt{s} = 13\ TeV$ at the different experiments. The acceleration takes place in four straight sections along its circumference in Radio Frequency (RF) cavities. Along the eight arcs, 1232 superconducting dipole magnets producing an 8T magnetic field bend the protons to their circular trajectory, and 392 superconducting quadrupole magnets focus the beams to counteract dispersion. The proton bunches, each containing 10^{10} protons, are arranged in 3564 bunches per beam, commonly referred to as one Bunch Crossing (BX). At the nominal $f_{rev} = 11.246\ kHz$, the 3564 bunches per beam give rise to a 24.95 ns BX separation, which makes for a 40.08 MHz BX frequency. For most of the 2015 fills, 2500 bunches of protons, each with 10^{10} protons were used for collisions.

3.1.2 Luminosity

A key parameter of a particle collider is its instantaneous luminosity, L $(cm^{-2}s^{-1})$. It gives access to the expected number of events $\langle \mathcal{N} \rangle$ for a cross section under investigation through

$$\mathcal{N}_{event} = \mathcal{L}\sigma_{event} \tag{3.1.1}$$

The instantaneous luminosity is defined by the LHC proton beam parameters. Assuming a Gaussian beam distribution, it is given by

$$\mathcal{L} = \frac{\gamma f k_B N_p^2 F}{4\pi\epsilon_n \beta^*} \tag{3.1.2}$$

where γ is called Lorentz factor, f is the revolution frequency, k_B is total number of bunches, N_p is the number of protons per bunch, β^* is the betatron function at the interaction point(IP).

The summary of 2015 and 2016 luminosity delivered by LHC and recorded by CMS is presented in Fig. 3.3.

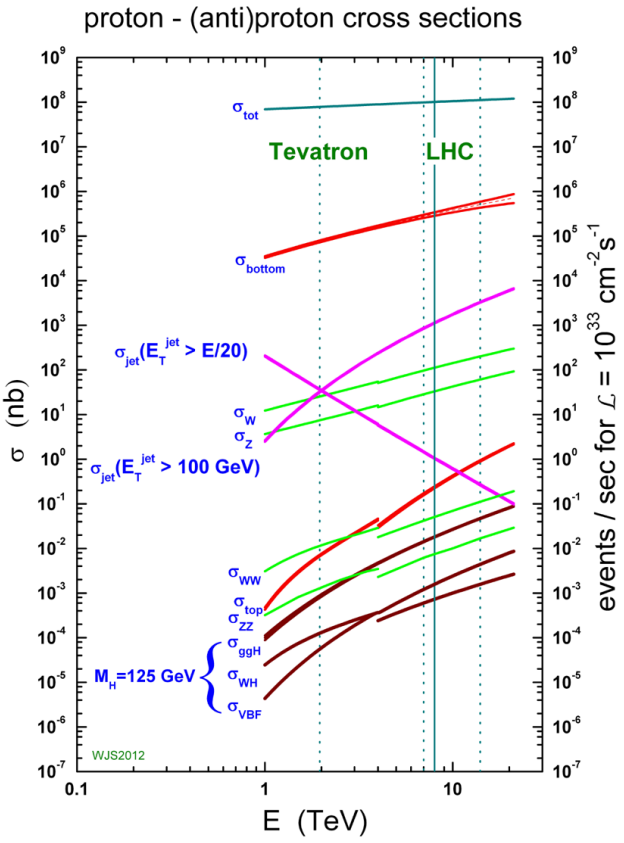

Figure 3.2: Predicted Standard Model of Particle Physics cross sections at the Tevatron collider (dashed line at $\sqrt{s} = 1.96\ TeV$) and the LHC collider (lines at $\sqrt{s} = 7\ TeV(2011)$, $8\ TeV(2012)$ and $14TeV$ (design)) as a function of the centre-of-mass energy $\sqrt{s}$ [4]. The discontinuities at 4TeV are due to the switch from $p\bar{p}$ to pp collisions at that energy.

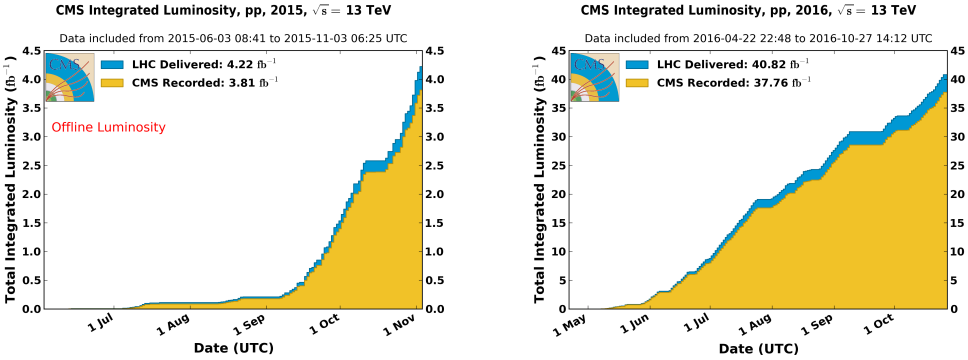

(a) (b)

Figure 3.3: Integrated luminosity plot for 2015 (a) and 2016 (b) data, delivered by LHC and collected by CMS [5]

3.1.3 The LHC Experiments

Considering the complexity and the cost of the LHC accelerator complex, it is important to make the most of its scientific reach. For this reason, the accelerated protons collide at four points along its circumference, as illustrated in Fig.3.1.

Two independent general-purpose experiments have been set up to investigate the proton-proton collisions: at P1, ATLAS [38] has been installed, and at P5 one finds the Compact Muon Solenoid (CMS) [39]. They have been designed to address the aforementioned challenges, starting with the Higgs boson discovery and searching for physics beyond the SM.

In the ALICE experiment [40], lead-ion collisions are studied to improve our understanding of the quark-gluon plasma. While bottom-quark physics and CP violation are thoroughly studied in the Beauty Experiment (LHCb) [41].

.

3.2 Compact Muon Solenoid (CMS)

Built as a general-purpose collider experiment, CMS [39] follows a classic layout with an inner tracking detector, followed by Electromagnetic and Hadronic Calorimeters, and muon chambers on the outside. These layers are organized in a barrel region, consisting of cylindrical coaxial layers around the beam pipe, and two endcap regions with disks closing the barrel region. The detector components were chosen to meet the LHC physics programme requirements, which translates into a tracker close to the Interaction Point (section 3.2.3) to provide high charged particle momentum resolution, and allow and b jet tagging, a hermetic Electromagnetic Calorimeter (section 3.2.4) to ensure good electromagnetic energy resolution, with significant material thickness in radiation lengths over a short distance, and with the granularity to achieve sufficient π^0 rejection and a hermetic Hadronic Calorimeter (section 3.2.5) to measure the energy of charged and neutral hadrons with significant material thickness in nuclear interaction lengths, allowing for good missing transverse energy resolution. Precise muon detection and identification that allows the measurement of momenta up to 1TeV is achieved with an extensive muon system (section 3.2.6) outside a significant amount of absorber material, and a single 3.8T superconducting magnet (section 3.2.2) allows the momentum assignment of charged particles throughout CMS.

An overview of these detectors and their key characteristics is shown in Fig. 3.4 with cross-sectional view shown in Fig. 3.4, and the most relevant features are explained in the following paragraphs.

3.2.1 The Coordinate System

The global coordinate system of CMS has its origin in the IP. A right handed coordinate system is used with the X-axis pointing towards the center of the LHC ring, the Y -axis pointing upwards, and the Z-axis along the beam pipe. Throughout this

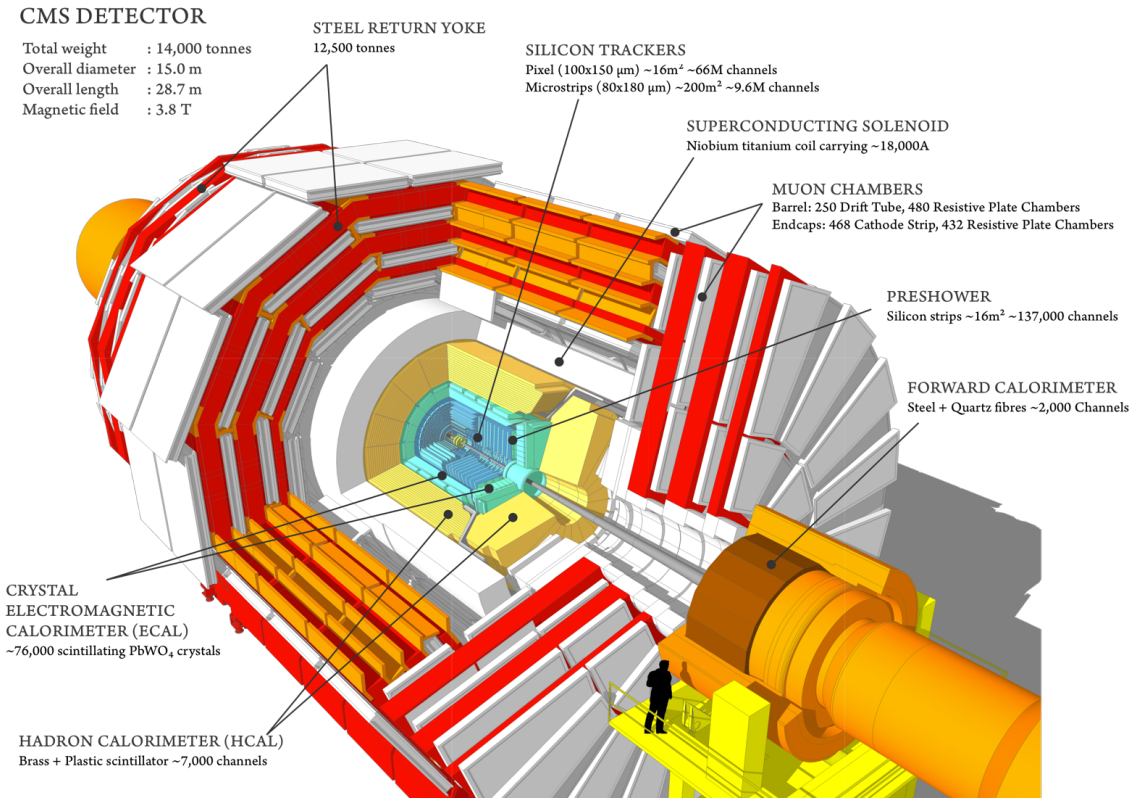

Figure 3.4: Full overview of Compact Muon Solenoid (CMS) at LHC

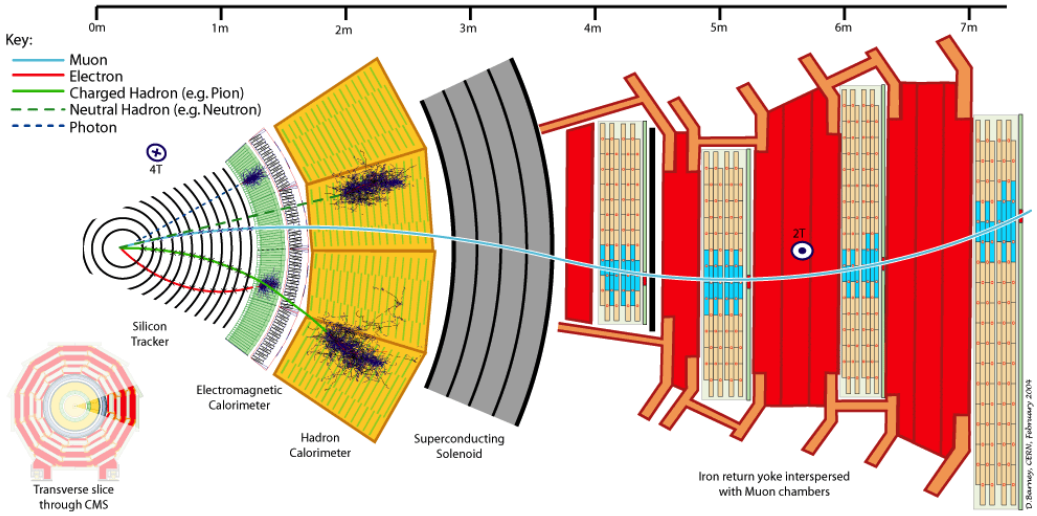

Figure 3.5: A cross sectional view of CMS sub detectors.

thesis, capitals will be used for these coordinates to differentiate them from the local coordinate systems of single detectors.

Because the LHC provides hadron collisions, the different energy fraction of the parton leads to an unknown total energy. Because of this, one is mainly interested in the transverse components of the total and missing energy. This same feature also leads to a potentially longitudinally boosted center of mass. As a consequence, quantitities invariant under such boosts are used, such as the transverse momentum P_T. Along the beam pipe, the Z-direction, the difference in pseudorapidity

$$\eta = -\ln(tan(\theta/2)) \tag{3.2.1}$$

between two particles is approximately invariant under such a boost for ultra-relativistic particles. Here, θ is the polar angle between the particle momentum and the Z axis. It is accompanied by the azimuthal angle ϕ, with the X-axis at ϕ= 0, to form a spherical coordinate system.

3.2.2 Superconducting Magnet

As suggested by its name, the Compact Muon Solenoid uses a superconducting solenoid to achieve accurate P_T measurements for charged particles crossing the detector. This 12.5 m long solenoid produces a magnetic field of 3.8 T, and to contain it outside its 6m diameter, it is surrounded by a 12500 tonnes steel return yoke. The three coaxial yoke layers of the barrel are interspersed with the muon detectors, allowing for significant muon track bending between them. Outside the magnet, the barrel yoke is organized in five separate dodecagonal wheels along Z (YB-2 to YB+2), which can be moved on high-pressure air pads to create space between them and give access to the installed detectors. The same is true for the three steel endcap disks on each side of the experiment (YE-1 to YE-4 and YE+1 to YE+4).

3.2.3 CMS Inner Detector

The CMS inner tracking system is a silicon-based detector, designed to measure the trajectories of charged particles very precisely. It consists of an inner silicon pixel detector within a distance of 200 mm from the beam pipe, providing 100 by 150 μm pixels arranged in three barrel and two endcap layers. The resulting 66 million active elements span a length of 98 cm. Surrounding the pixel detector are 10 barrel layers and 12 forward layers of silicon strip detector, covering the region up to 116 cm from the beampipe, along 5.6 m with 9.3 million channels. Several strip layers (barrel) and rings (endcap) are instrumented with a second micro-strip detector module. The strip detector also provides two-coordinate measurements in at least ≈ 4 hits for $\eta < 2.4$.

3.2.4 The Electromagnetic Calorimeter

In the next layer, the energy of the electrons and photons is measured by the Electromagnetic Calorimeter (ECAL). The ECAL subdetector covers the pseudorapidity range $\eta < 3.0$ with 61200 lead tungstate ($PbWO_4$) crystals in the barrel, read out by

Avalanche Photodiodes (APDs), and 7324 crystals in the endcap region, read out by Vacuum Phototriodes (VPTs).

The barrel region consists of 36 supermodules with 20×85 crystals each, covering $\Delta\eta \times \Delta\phi = 0.0174 \times 0.0174$ or a 22 by 22 mm^2 front-face cross section. The endcaps feature two Dees each, holding 3662 crystals with a front-face cross section of 28.62 by 28.62 mm^2.

An additional sampling calorimeter in the endcaps, the Preshower (PS), is installed to improve the resolution in order to resolve the two photons of a π^0 decay: behind a two lead radiators of 2 and 1 X_0 each, two layers of silicon strip sensors are configured orthogonally to measure the electromagnetic showers.

3.2.5 The Hadronic Calorimeter

The Hadronic Calorimeter (HCAL) initiates a cascade of secondary particles for the high-energy hadrons by alternating layers of non-magnetic brass absorbers and fluorescent scintillators. It consists of a coaxial barrel region up to $\eta < 1.3$ (HB, 5.4 to 10.6 λ_I), an endcap region up to $\eta < 3$ (HE) and a forward region further down the beam pipe at 11.2 m that increases the coverage up to $\eta < 5.2$ (HF). The limited space for stopping power in the barrel region is overcome with an additional calorimeter outside the solenoid up to $\eta < 1.3(HO)$ that uses the coil and a 19.5 cm layer of steel yoke as absorber.

Between the brass absorber plates ($\approx$ 5 cm for HB, $\approx$ 8 cm for HF), scintillator tiles with a segmentation depending on η from $\Delta\eta \times \Delta\phi = 0.087 \times 0.087$ to 0.17 $\times$0.17 produce the optical signal that embedded wavelength-shifting fibres take to Hybrid Photodiodes (HPDs). The total amount of light summed over the layers of tiles within a given region is a measure for the passing particle's energy.

3.2.6 CMS Muon System

Another key feature of the CMS experiment is its extensive muon system. As a powerful handle to the signature of interesting events, the trigger and reconstruction capabilities for muons are very important. The hermetic design of the calorimeters means that very little of the hadronic showers leaks into the system, leaving a clean muon identification system.

The CMS muon system comprise of three different technologies shown in Fig. 3.6. The Drift Tubes are installed in the barrel (central region) ($\eta < 1.2$), where the occupancy and background noise are lower. In the endcap regions, muon rate and neutron-induced background rates dictate the use of Cathode Strip Chambers ($0.9 < \eta < 2.4$). Both systems consist of gaseous drift chambers, and provide precise space and time measurements. The Resistive Plate Chamber (RPC) system covers both the barrel and endcap regions ($\eta < 1.61$) and provides an independent measurement for triggering purposes with a coarser space resolution but a fast time response for unambiguous BX assignment. RPC working mechanism and construction is described in detail in chapter 4.

3.2.6.1 Drift Tube Chambers

The Drift Tube (DTs) are gaseous particle detectors built with 13 by 42 mm^2 rectangular drift cells (3.7b). A 50 µm gold-plated stainless steel wire serves as the anode at 3.6 kV, and two 50μm thick aluminum electrodes on the short edges of the drift cells serve as cathodes ($-1.8\ kV$). The long edges contain 50 µm thick aluminum field electrodes at $1.8kV$. The cells span the full length or width of the chamber of $\approx 2.4\ m$.

The full barrel region is equipped with 4 coaxial layers of DTs (*stations* MB1 to MB4), with one DT in each of the 12 sides of each dodecagonal wheel (*sector*), and an additional separation in the outer layer of the top and bottom sector. Inside a

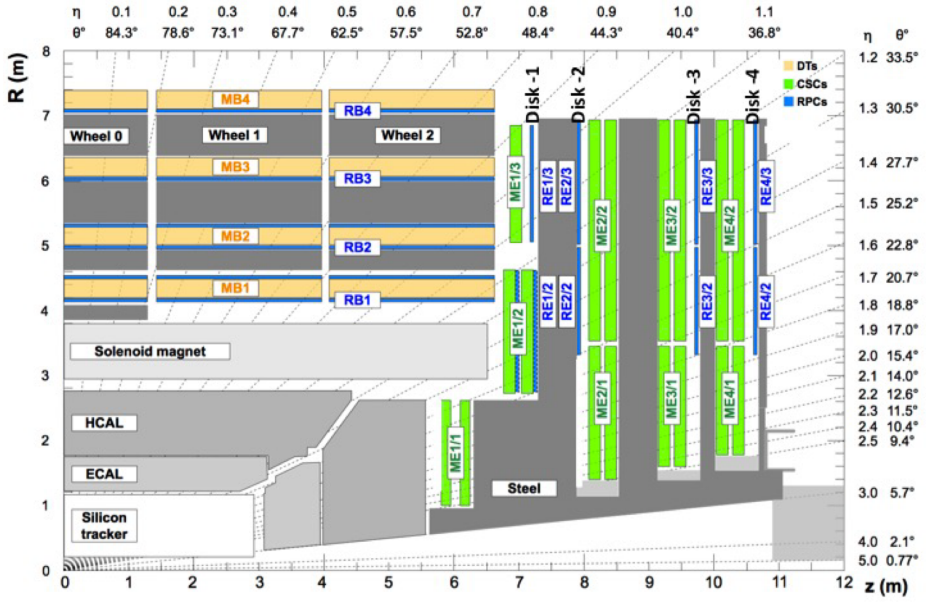

Figure 3.6: Quadrant illustration of the muon spectrometer with DT chambers (yellow), RPC (blue), and CSC (green) [6].

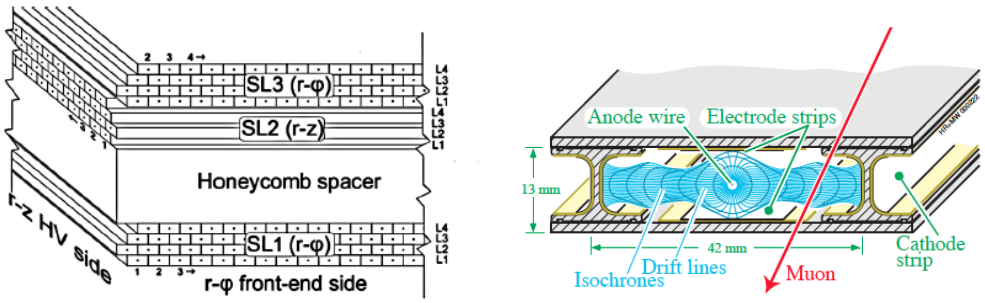

(a) (b)

Figure 3.7: llustration of the Drift Tube Chamber chambers. (a) shows a schematic view of a DT chamber [7]. Two superlayers measure the $\eta-$coordinate, and one superlayer measures the $\phi-$coordinate. A honeycomb plate separates the two $\phi-$superlayers and provides rigidity. (b) shows a single DT cell and its drift lines and isochrones [7].

DT, the position of the passing muons is measured in 3 superlayers consisting of four staggered layers each, with wires along Z in the outer superlayers, and along ϕ in the middle suyperlayer [1] (3.7a). Combining the information from the different layers, a DT achieves a 100 µm resolution.

3.2.6.2 Cathode Strip Chambers

The Cathode Strip Chambers (CSCs) are also gaseous particle detectors, this time combining cathode strips running along η, and perpendicular anode wires measuring the η coordinate. These multiwire proportional chambers consist of seven cathode panels, interleaved with six anode wire planes in the 9.5mm gaps (3.6). They are operated at an anode wire voltage of 2.9 to 3.6 kV, in a 50% CO_2, 40% Ar, and 10% CF_4 gas mixture. Using a 8.4 to 16 mm strip pitch and a wire-distance of 2.5 to 3.16mm depending on their location, they provide a 75 to 150 µm resolution.

They are installed over the full 360^0 $\Delta\phi$ span in 4 layers ($ME1$ *to* $ME4$) and up to three rings as illustrated in Fig. 3.8.

3.2.7 The CMS Trigger and Data Acquisition System

The high luminosity and collision rate provided by the LHC, arriving in trains of several MHz, mean the CMS sub-detectors produce the equivalent of several TBs of data after zero suppression. Data at these rates can not be fully processed and stored at this rate.

Since only a fraction of these events provide insight into the physics processes under investigation, the CMS Trigger and Data Acquisition System (TriDAS) is designed to reduce this rate by selecting events based on their content (Fig. 3.9). This selection is made in two steps. First, the Level One Trigger (section 2.2.1) selects relevant events at a rate of (100 kHz) [20] using dedicated hardware, after which

[1] MB4 only has the 8 layers measuring the ϕ coordinate

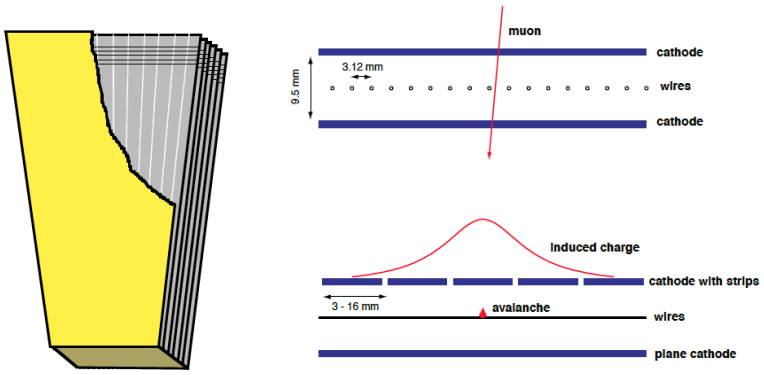

(a) (b)

Figure 3.8: Illustration of the Cathode Strip Chamber chambers. (a) shows a cut-away diagram of a CSC chamber with few of its anode wires, indicating the cathode strip and anode wire directions [7]. (b) shows a cross-sectional view of the gas gap in a CSC, with a schematic illustration of the gas ionization avalanche and induced charge distribution on the cathode strips [7].

the detector channels have to be read out and sent to a commercial processor farm. There, the High Level Trigger further reduces the event rate to (100 to 800 Hz) [21, 22]. Selected events are then written to disks and tapes, and distributed among the data tiers across the globe to be processed by end-users.

3.2.7.1 The Level One Trigger

L1 Trigger, the first step of online event selection system consists of dedicated electronics that receive data of a subset of the CMS detector channels every 25 ns, to process the full 40 MHz rate at which collisions may occur. The L1T traces back all particles, total and missing transverse energy E_T that gives an idea of the total energy involved and hints at high-energy neutral particles crossing the detector unnoticed.

During RUN-I the L1T system followed a tree-like structure, going from local detector specific processing, via regional triggers, to global triggers Using the local hits, segments and clusters, the regional systems attempt to locate particle passages throughout the detector. The global processors combine these objects, sort them and

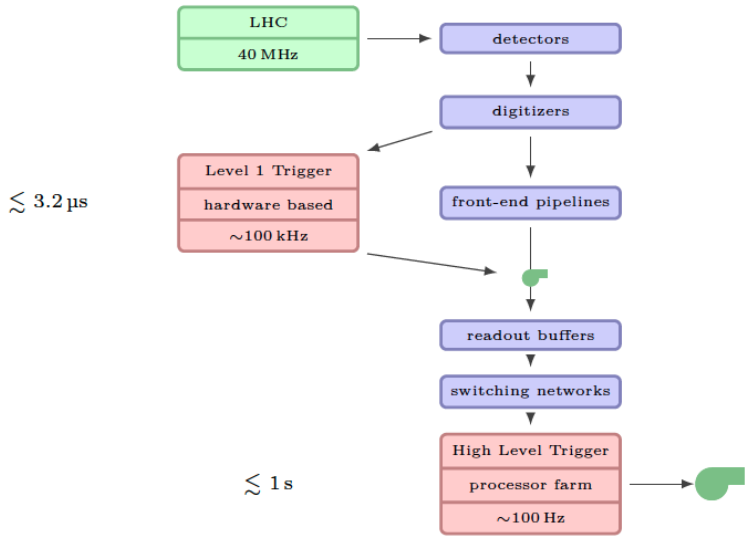

Figure 3.9: Outline of the CMS Trigger System.

provide them to the GT that takes a final decision, distributed as the Level One Accept (L1A) signal. This decision has to arrive 128 $BX(3.2\ \mu s)$ after the actual Bunch Crossing, the time during which readout buffers can contain the data corresponding to an event. A large portion of this time actually goes into the transmission to and from the Underground Service Cavern (USC55) where the Trigger-dedicated hardware is located.

3.2.7.2 The Level One Calorimeter Trigger

The Calorimeter Trigger System measures local energy deposition sums in the ECAL and the HCAL detectors for common $\eta - \phi$ regions, called the calorimeter towers, using dedicated circuits on the readout electronics. Then the Global Calorimeter Trigger (GCT) receives these trigger primitives and sends the four best candidates of each category to the GT.

To support the Global Muon Trigger (GMT), the regional calorimeter trigger (RCT) also transmits two bits indicating if energy deposits are comparable with the

passage of a least Ionizing Particle (MIP), or if a region is compatible with an isolated muon.

3.2.7.3 The Level One Muon Trigger During RUN-I

The different CMS muon detectors each have their own system for detecting and roughly reconstructing the passage of a muon. For the CSC and DT detectors, this process takes place in two phases: local triggers reconstruct track segments, and the track finders combine that information.

DT and CSC Local Triggers The first stage is performed in on-chamber electronics, and aims to reconstruct local track segments pointing towards the IP. The DT does this by finding drift cells with coincident aligned hits in three out of four layers of a super layer, within a group of nine drift cells. A mean-timer technique matches the hits to a straight-line segment, and a BX is assigned. These segments are matched between the two outer super layers comparing them with pre-computed patterns, and sorted by momentum. This information is combined with the segments from the middle layer where possible and up to two segments in each chamber are collected for the DT Track Finder (DTTF).

In the CSCs, signals on cathode strips are combined per layer to achieve a half-pitch resolution, and a coincidence of four layers is required to create a segment (Fig. 2.9). This is executed in a crate on the balconies. For the anode wires, 10 to 15 wires are there in a single channel, and again segments are selected using a four-out-of-six logic, this time in on-chamber electronics. To assign a BX, the coincidence takes place in two steps: when two layers have coincident hits, a segment pre-trigger is fired and the BX is assigned. The segment trigger is final if another two layers give a signal within the next 50 ns, to allow for the drift time. The η *and* ϕ segments are combined in Trigger Mother Boards (TMBs) on the balconies, where also the signals from the neighbouring RPCs arrive to resolve ambiguities. Up to three segments per

chamber can be transmitted to the CSC Track Finder (CSCTF).

DT and CSC Track Finders: The Track Finders build the segments into tracks, assign them their P_T and transmit up to four candidates to the GMT. For the DTTF, this is achieved by extrapolating the segments to neighbouring chambers using LUTs, and looking for matching segments within a given window around the projection. The matching segments are then linked in a series and joined into muon candidates. The CSCTF tries to match segments pairwise for consistency with a single track, and then tries to match the segment pairs into a single muon track. In the overlap region, local track segments are shared between DT and CSC.

The final muon candidates are assigned a P_T using LUTs, and the coordinates at the second station are used to assign η *and* ϕ coordinates. The muon candidates are assigned a quality that depends on the number and location of the contributing segments. Both Track Finders then send up to four muon candidates each to the GMT.

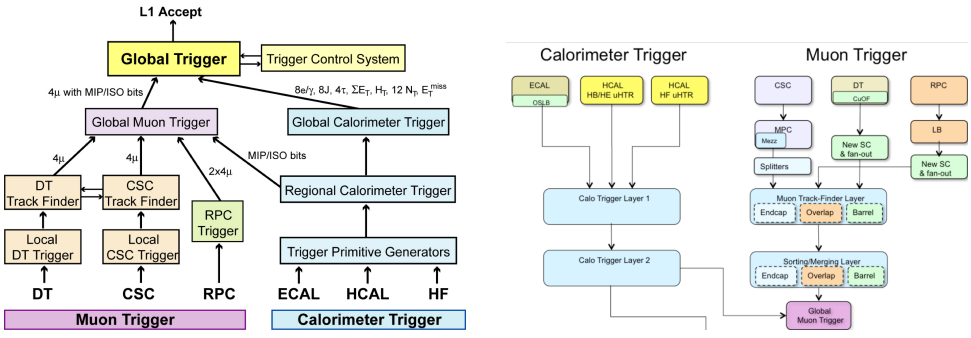

(a) (b)

Figure 3.10: Illustration structure of the legacy $L1$ Muon Trigger and Calorimeter Trigger (a) and upgraded Muon Trigger and Calorimeter Trigger (b) .

RPC Muon Trigger: For the RPC detectors spanning the η range up to ± 1.61 during RUN-I and up to 1.9 during RUN-II, up to four muon candidates are traced back in both regions.

The RPC Pattern Comparator Trigger (PACT) is based on the spatial and temporal coincidence of hits in RPCs lying on the possible path of a muon coming from the interaction point. Such coincidences of hits are called hit patterns or candidate tracks. Due to energy loss and multiple scattering, there are several possible hit patterns in the RPC muon stations to be identified. Fig. 3.11 illustrates pattern finding algorithms in the $r - \phi$ plane. Patterns allow to identify muons with at least four hits on six RPC layers in the barrel and three out of four in the endcaps (presently, the fourth RPC endcap stations are staged).

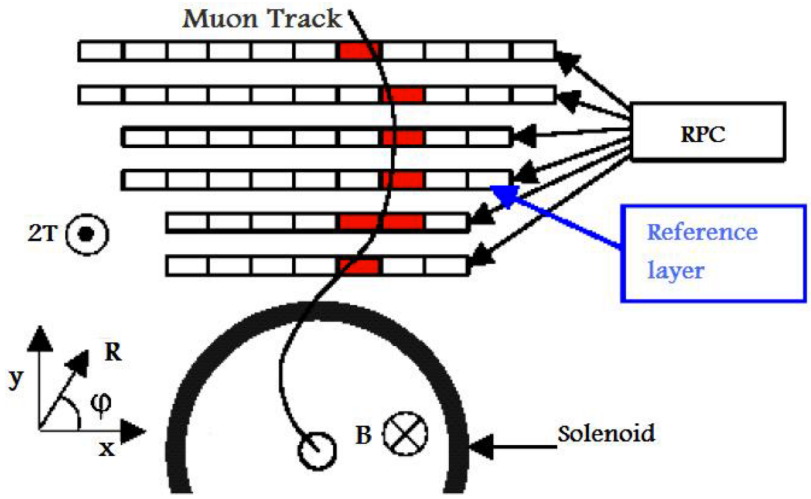

Figure 3.11: Overview of the RPC Pattern Comparator Trigger (PACT).

Tens of thousand of patterns are needed for the whole RPC system and were obtained from Monte Carlo simulations. Trigger electronics are based on Field Programmable Gate Array (FPGA) technology [98], which allows comparison of hits with all implemented patterns concurrently. Predefined patterns of hits have to be mutually exclusive with a unique transverse momentum assignment. Patterns are divided into groups with a sign and a code which denote the transverse momentum in the range 0 - 140 GeV assigned to each of them. The four highest P_T muon candidates in the barrel and four from the endcaps combined are then sent to the GMT.

CMS Upgraded Muon Trigger: The L1 trigger mechanism of the CMS experiment has been upgraded between 2015 and 2016 to maintain the performance of CMS trigger under the extreme conditions during Run-II. The newly developed system was commissioned by using data collected in 2015 running of LHC, and has been used during 2016 data taking period.

The upgraded L1 Muon Trigger was designed in a different way as compared to one used during RUN-I, idea was to exploit the redundancy of sub detectors at an earlier stage, resulting an improved overall performance. The upgraded CMS muon trigger system is composed of three muon track finders, each covers a different η region. The barrel muon track finder (BMTF) collects data from RPC and DT, covering $\eta < 0.83$ region. The endcap muon track finder (EMTF) receives data from RPC and CSC in the region $\eta > 1.24$. The overlap muon track finder (OMTF) receives data from all the three subdetectors in the central region $0.83 < \eta < 1.24$. The output of the three track finders is collected by the GMT, which then ranks the muons by their quality and transverse momentum, removing the fake reconstructions across the boundaries, and provides the collection of output muons to the global trigger (GT). The Calorimeter Trigger input is used to compute the isolation of muon candidates.

In the BMTF, information of track bending angle in every DT station permits the implementation of a road search extrapolation track finding: extrapolating the hits in each station to adjacent stations and matching them as a initial step for reconstruction of tracks and P_T assignment. RPC and DT information is collected and combined in the $TwinMUX$ system in the form of super-primitives. In the OMTF and EMTF, a system latency of around 750 ns, non-uniformities in the magnetic field and high background rates, impose the usage of a fast pattern-based track finding algorithm.

Global Muon Trigger: The three described muon triggers provide CMS with a two to three-fold redundancy, depending on the η region. By combining the information from the three muon triggers, the GMT attempts to improve the muon trigger

efficiency and purity, reduce the trigger rates and suppress the background.

To do so, the GMT collects up to four candidates from both the DTTF and the CSCTF, as well as four muons from both the RPC barrel and endcap regions. These muons are described by their P_T and charge, their η *and* ϕ coordinates at the second station and the aforementioned qualities. In addition, it receives quiet bits (to indicate the energy deposition in the calorimeters is below a given threshold) and MIP bits (to indicate an energy deposit compatible with a MIP crossing) from the GCT for $\Delta\eta \times \Delta\phi = 0.35 \times 0.35$ calorimeter regions. After synchronizing these inputs, barrel RPC and DT candidates are matched by calculating the distance at the second muon station, $\Delta r = \sqrt{w_\eta(\Delta\eta)^2 + w_\phi(\Delta\phi)^2}$ using appropriate weights for η *and* ϕ depending on the region.

The Global L1 and HLT Trigger: The Global Trigger (GT) is the final step of the Level One Trigger, and issues the L1A signal for selected events. This decision-taking is performed based on the candidate particles and quantities from the GCT and GMT, as well as a set of up to 64 Technical Triggers, special-purpose direct trigger signals from sub-detectors.

The core logic of the GT is performed by the Global Trigger Logic (GTL) module. This card applies up to 128 so-called algorithms intended to match different physics event signatures. For each algorithm, it tests if one or more candidate particles or quantities comply with a given set of restrictions, be it a lower threshold on P_T, quality, E_T, cuts on the allowed charge or the presence of MIP or isolation bit, η *and* ϕ ranges, or even cuts on the $\Delta\eta$ or $\Delta\phi$ between candidate particles. These restrictions form a condition, and the final algorithm is a logical expression of one or more condition results.

Inside the Final Decision Logic (FDL) card, each of these algorithm decisions can be deterministically prescaled, depending on the abundance of corresponding events at a given instantaneous luminosity, or even masked. A logical OR of the resulting

decisions with (potentially masked or prescaled) Technical Trigger decisions or vetos defines the final Level One Accept (L1A) decision.

The outcomes for the different algorithms go on to serve in logical expressions that initiate corresponding High Level Trigger paths. After the L1 accept signal, further event filtering is performed by the HLT. The HLT executes more complex physics selection algorithms on commercial computer, in order to accept only events with the most interesting physics content. The total processing time is $\approx 1s/event$, after which the accepted rate reaches the desired 100 Hz. In order to optimise data flow, event selections are made in progressive stages by applying a series of filters. The initial decision is made on a subset of data, from detector components such as calorimeter and muon systems (Level-2). Final HLT algorithms are then applied to the complete event (Level-3) and accepted events are sent to mass storage.

Chapter 4

Resistive Plate Chambers

Muons provide a clean signal to detect interesting events over complicated backgrounds at the LHC. The ability of muons reconstruction and triggering at the high luminosities are highly important concepts of CMS. Given the key role of muons in the selection of events, the fast Resistive Plate Chambers are a crucial part of the CMS experiment. This chapter goes through a brief introduction to gaseous detectors, the main features of RPC detector and trigger system. The author took an important role in the commissioning of services, operation, data quality monitoring and offline performance analysis of data recorded during LHC RUN-II, related to the RPCs in CMS.

4.1 Gaseous Particle Detectors

From the early stages in particle detection for High Energy Physics (HEP) experiments, gaseous particle detectors have played a crucial role. Throughout the years, they have evolved from the single-wire proportional counter introduced by Rutherford [42], to a wide range of fast, efficient detectors with a fine resolution at a reasonable cost [43]. They also brought the particle tracking detectors from photographic to fully electronic devices, a major step for the analysis capabilities of experiments. From the advent of the multi wire proportional chamber [44] onwards, they enabled

the discovery of a high number of particles. Despite the broad range of gaseous particle detectors, the principle remains broadly the same. As particles cross a gaseous medium, they ionize its constituents. The resulting electrons and ions are then accelerated by an electric field, and through secondary ionization the electrons may cause an avalanche. The avalanche can grow to a streamer or a spark from anode to cathode depending on the electric field, the geometry and the gas in use. The propagation of these free charge carriers induces a signal on readout electrodes, which depending on the layout and electronics can give a fine grained position and time information about the path of the particle.

4.2 Resistive Plate Chamber Development

In the last 30 years Resistive Plate Chambers (RPC) have been chosen for many cosmic-ray and collider experiments. The main characteristics that make RPC so appealing are: high gain, good time resolution, very simple design, and lower cost. Schematically (Fig. 4.1), RPCs are made by two resistive electrodes with a conductive coating, like graphite. Electrodes are generally made from phenolic resins, like bakelite, with a bulk resistivity of $\rho = 10^{10-12}\ \Omega cm$. For electrical and mechanical stability, these electrodes are mounted on rectangular plastic frames and kept at constant distance from each other by means of small plastic separators. The gap between the electrodes is filled with a gas mixture usually containing an organic gas with high UV absorption capability to reduce secondary avalanches and a strongly electronegative gas to control charge multiplication. A voltage difference is placed across the electrode. When an ionising particle crosses the active volume, free charges are accelerated by the external field and start an avalanche. Signal pick-up is realized by conductive strips, usually aluminium or copper, laying on top of the graphite coating and insulated by a mylar foil.

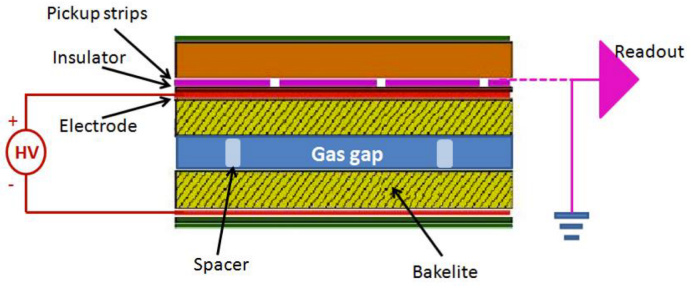

Figure 4.1: Schematic representation of RPC.

Traditionally, RPCs had been operated in streamer mode. With this configuration, charge developed within the gas gap at the passage of a ionizing particle is 100 pC. The use of resistive electrodes and a well thought gas mixture 4 limited the region interested in the discharge to an area of 0.1 cm^2. Thus the detector could withstand an incident flux of about 100 Hz/cm^2 (assuming a dead time of the order milliseconds). Streamer mode is not suitable for high-rate experiments and therefore inadequate for LHC environment. To increase rate capability, a possibility is to work in avalanche mode, i.e. keep the gas gain factor lower than 10^8. In this case the avalanche grows to a maximum of 25 pC allowing an incident rate of the order of kHz/cm^2 [45], but requiring robust signal amplification electronics. Because of high rate capability RPC are suitable in experiments like CMS at LHC.

4.3 Resistive Plate Chamber Working Principles

4.3.1 Passage of a Muon through an RPC

When a relativistic muon crosses the RPC gas volume, it predominantly interacts with the gas molecules through the electromagnetic interaction. The mean energy loss per length through ionization and excitation for relativistic heavy charged particles ($m \gg m_{electron}$) is described by the Bethe-Bloch equation [46] (4.3.1),

$$-\frac{dE}{dx} = 4\pi N_A r_e 2m_e c_0^2 z^2 \frac{Z}{A}\rho\frac{1}{\beta^2}\left[\frac{1}{2}\ln\frac{2m_e c^2\beta^2\gamma^2 T_{max}}{I^2} - \beta^2 - \frac{\delta}{2}\right] \tag{4.3.1}$$

- ρ is the density of the material,
- N_A the Avogadro number and r_e and m_e are classical radius and mass of electron,
- x the travelling distance into the target,
- c the speed of light,
- z the charge of the incident particle,
- Z the atomic charge number of the material and
- A the atomic number of the material,
- $\beta = v/c$ is the velocity of the particle in units c, and $\gamma = \frac{1}{\sqrt{1-\beta^2}}$,
- δ the density correction.

I represents the mean excitation energy, and T_{max} is the maximum energy transfer in a single collision of the particle with mass m and momentum p,

$$T_{max} = \frac{2m_e p^2}{m^2 + 2\gamma m_e m + m_e^2} \tag{4.3.2}$$

Polarisation of the medium screens the long-distance interaction of the particle, truncating the rise in energy loss expected from the extending electric field with higher energy.

It should be noted that Eq. 4.3.1 describes the mean energy loss. The energy loss through a given ρdx is a stochastic process following the long-tailed Landau distribution, which implies the most probable value is well below the predicted mean ([46]).

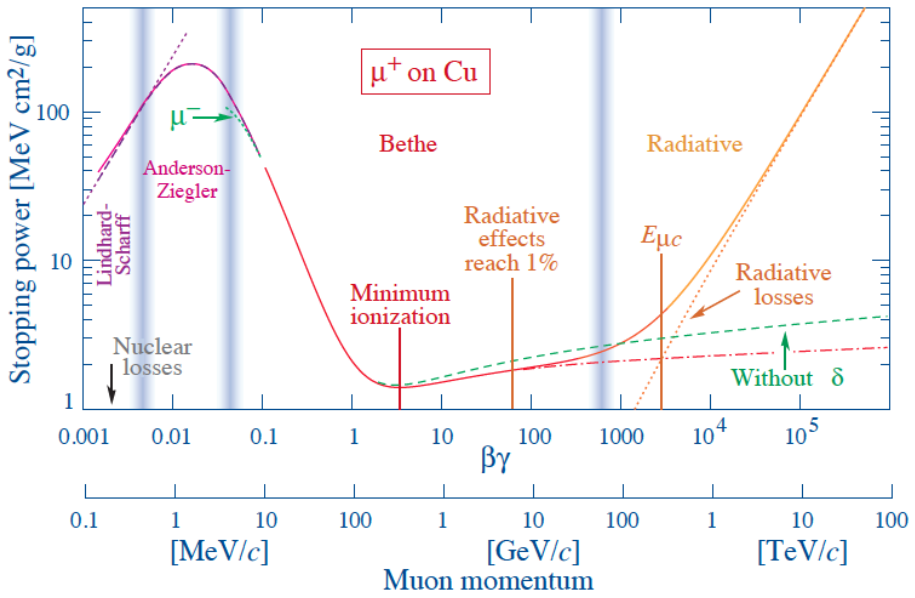

Figure 4.2: Energy loss $\frac{-1}{\rho}\frac{dE}{dx}$ for positive muons in copper as a function of $\beta_\gamma = \frac{p}{mc}$ [10]. The increasing contribution of the density effect with muon momentum is illustrated (δ, green dashed). E_{μ_c} represents the muon critical energy, at which energy losses due to radiation (orange, dotted) and ionization (red, dot-dashed) are equal. The energy of a MIP is also indicated..

While other effects contribute to the energy loss of the particle, it is the loss of kinetic energy through excitation and ionization of the gas atoms and molecules that enables the RPC to detect the passage of a muon. The excited atoms can either emit a photon when returning to the ground state, emit an Auger electron or cause ionization through collision (Penning effect). The photon can in turn either be absorbed by an atom if its energy exceeds the minimum ionizing potential, as such ionizing it through the photo-electric effect, or it can escape undetected.

4.3.2 Avalanche Development

4.3.2.1 Electron Multiplication

The electron-ion pairs along the muon track, the *primary clusters*, are the free charge carriers that initiate Townsend avalanches as the electrons are accelerated in the electric field E and cause further ionization.

Given the limited energy loss, consecutive ionizations are independent and the number of primary clusters n_c follows a Poisson distribution [47],

$$P(n_c) = \frac{(g\lambda_{eff})^{n_c}}{n_c!} e^{-g\lambda_{eff}} \tag{4.3.3}$$

for gap width g and $\lambda_{eff} = \lambda/cos\phi$, the effective number of primary clusters n_c per unit Z for a particle incident at angle ϕ with respect to the length z. This also defines the distributions of the positions z_j of primary cluster j,

$$P(z_j) = \lambda_{eff} \frac{(z\lambda_{eff})^{j-1}}{n_{j-1}!} e^{-z\lambda_{eff}} \tag{4.3.4}$$

The development of the electron cascades from these clusters is driven by the Townsend ionization coefficient α and the attachment coefficient β, respectively describing the average number of electron-ion pairs created, and the average number of electrons attached to form a negative ion according to [48]

$$\frac{dn_j}{dz} = (\alpha - \beta)n_j \tag{4.3.5}$$

where z is the position along the electric field and n_j the number of electrons from primary cluster j.

Different models exist to describe the fluctuations of the avalanche development and their impact on the signal induction [49, 47]. For constant α and β, one approximation assumes an exponential avalanche development with total charge [47]

$$q_e(z) = \sum_j^{n_j} q_e M_j n_{j,0} e^{(\alpha-\beta)(z-z_j)} \tag{4.3.6}$$

at position z for primary clusters j with initial number of electrons $n_j, 0$, where q_e is the electron charge. The factor M_j accounts for the stochastic fluctuation, and the Polya distribution is reported to give good agreement of simulation and experiment.

4.3.2.2 Signal Induction

Using Ramo's theorem [50], the current induced on an electrode by the movement of the resulting electrons in the electric field can thus be calculated as a function of the weighting field E_w and the drift velocity v_d [47]

$$i(d) = -v_d.E_w \sum_j^{n_j} q_e M_j n_{j,0} e^{(\alpha-\beta)(t-t_j)} \tag{4.3.7}$$

4.3.2.3 High Voltage Correction

The Townsend ionization coefficient α is reported to have a functional dependence on $\frac{E}{P}$, leading to an approximate High Voltage (HV) correction for the environmental pressure of [51, 52]

$$V_{eff} = \frac{P_0}{P}\frac{T}{T_0}V_{app} \tag{4.3.8}$$

with an additional term $\propto \ ln\frac{p}{p_0}$ suggested in [53] based on Eq. 4.3.6 and the Korff approximation for α,

$$\frac{\alpha}{P} = A\exp(-\frac{B}{P}E) \tag{4.3.9}$$

4.4 CMS Resistive Plate Chambers

RPC chambers [53] at the CMS detector are made by parallel resistive plates of phenolic resin (bakelite) treated with linseed oil [54] and separated by a gas gap of 2 mm. Mechanical stability is insured by mounting the electrodes on a rigid plastic frame and by using Poly-Vinyl Chloride (PVC) spacers to keep width constant throughout the gap. Read-out channels are conductive strips which are kept seperate from the graphite paint on the outer surface via an insulating Poly-Ethylene Terephthalate (PET). A higher rate capability compared to traditional RPCs is achieved by operating in avalanche mode rather than streamer mode: the electric field and consequently the gas multiplication is reduced requiring an improved electronic signal amplification. In order to increase the signal on the readout strips, a double-gap design is used in CMS, with two (Fig. 4.3) gas gaps of 2 mm width being read out by one group of strips in the center. The RPCs are operated at $9.3 - 9.5\ kV$ with a gas mixture of 95.2% $C_2H_2F_4$, 4.5% $i - C_4H_{10}$ and 0.3% SF_6. A rate capability of 1 kHz/cm^2 can be achieved.

4.4.1 Conditions and Requirements

Key requirements of RPC [8] are good timing, low cluster size (*i.e.* the number of contiguous strips fired by a moving muon), and good rate capability, high efficiency, and ability to withstand high background conditions.

Good and fast timing performance is highly important for triggering the events with a high efficiency. The trigger must identify muon candidates within a 25 ns

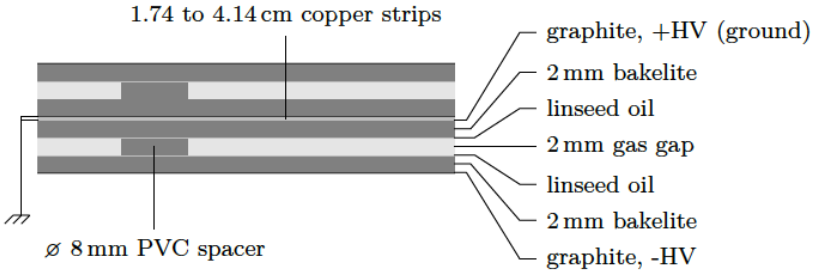

Figure 4.3: Cross-sectional view of a CMS RPC. The top gap mirrors the bottom gap.

window. This requires a time resolution of only a few nanoseconds.

One of the key requirements is a small cluster size ($<$ 2) which is crucial for achieving the required momentum resolution. Finally, rate capability is required to be 1 kHz/cm^2 with a detector efficiency of $>$ 95%. In fact, background hit rate is comparable to incident muon rate in high regions. Therefore, 1 kHz/cm^2 is a reasonably safe estimate of the highest rate at which the RPCs are expected to participate in the operation.

4.4.2 Electrode Resistivity

Electrode bulk resistivity ρ strongly influences detector rate capabilities. Two main effects may be identified: the time constant $\tau \propto \rho$ of the RPC region involved in an avalanche process decreases with ρ, additionally, at very high rates, the current owing through the bakelite plates produces a non-negligible voltage drop, V_d, across them [55]. V_d can be estimated as:

$$V_d = 2\langle q_e \rangle \, rs\rho \tag{4.4.1}$$

where r is the rate and s is the electrode thickness. Assuming $q_e = 25\ pC$ and $r = 10^3\ Hz/cm^2$, a value of $\rho \approx 10^{10} cm$ is to be used to limit V_d to a nominal voltage. Huge voltage drop reduces rate capability and influences the pulse delay due

to changes in drift velocity, which decreases with the effective voltage. This value of ρ yields $\tau \approx 31\ ms$.

4.4.3 Gas Mixture

Usual gas mixtures employed in RPCs have values of gas cluster density (λ) contained between 2 and 8 clusters/mm. Lower values would give rise to high inefficiency, due to lack of primary pairs. Total RPC gas volume, at CMS, is 10 m^3 for the barrel and 6 m^3 for both endcaps. All chambers operate on a non-flammable gas mixture of 95.2% $C_2H_2F_4$ (freon), 4.5% $i - C_4H_{10}$, and 0.3% SF_6 [56]. For this variety of freon [57] $\lambda \approx 5$. The effective ionizing coefficient, η, is 18. Freon acts as a strong quencher on the discharge, keeping the detector in avalanche mode. Isobutane instead is used to absorb photons and reduce the region interested by the discharge. Finally, it has been seen that a very small percentage of SF6 added to a binary mixture ($C_2H_2F_4, i - C_4H_{10}$) suppresses streamer probability. A percentage of SF_6 equal to 0.3% is enough to widen the operating plateau of almost 200 V [58].

4.4.4 Gap Width and Double Gap Structure

Gap width influences detector time resolution. Fig. 4.4 shows the simulated achievable time resolution w.r.t gap width and full width at the base (FWAB), which is defined to be the time interval with 95% of the events. Unfortunately, in narrow gas gaps total charge collected at the electrodes is lower compared to wider gaps and stronger signal amplification is needed. A 2 mm gap width seems best compromise.

CMS RPCs use a double-gap configuration. Two single gaps are mechanically coupled and signals are extracted from a plane of strips located in the middle. It maximizes the induced signal which is the analogue sum of the seperate signals developed in each chamber.

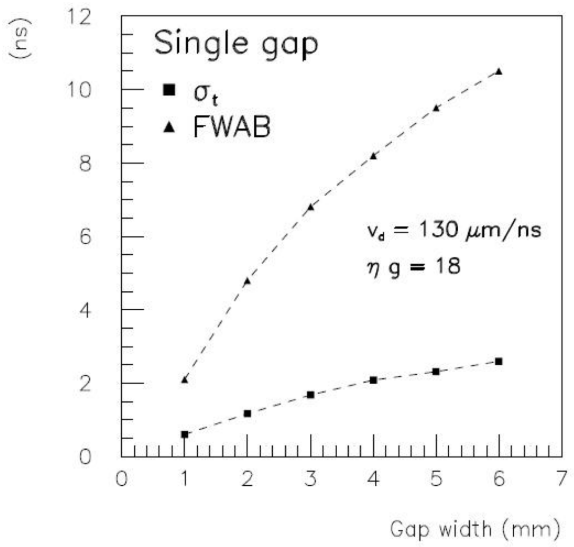

Figure 4.4: Simulated time resolution w.r.t the width of gas gap [8] and full width at base (FWAB)

4.4.5 Pick−up Strips

Muon bent tracks in CMS are measured in $r-\phi$ plane with high granularity to insure good transverse momentum resolution. Nominal strip angular width is to be $\frac{5}{16}^0$ in the $r-\phi$ plane [59, 60]. Barrel chamber strips run parallel to the z-axis with $2.2-4.1$ cm pitch. Endcap strips are radially arranged and are trapezoidal in shape. All endcap rolls count 32 strips (96 strips per chamber), while barrel, due to geometrical constrains rolls have a number of strips that varies among 36, 42, 48, 60, 84, and 90. Assuming signal propagation velocity is $\frac{2}{3}c$, a maximum strip length of about 1 m is allowed. In CMS, long strips, raging from $80-100$ cm, are used in the barrel wheels where background rate is comparatively low. Instead, in the endcap, where the background rate is quite high, strips are only 25 to 80 cm long.

Chapter 5

RPC Performance Studies at $\sqrt{s} = 13\ TeV$

The RPC Data taken with cosmic rays and p-p collisions at 13 TeV in 2015/2016 , is used to study detector and trigger performance. Hundreds of millions of cosmic muons have been collected in order to prepare for extended data taking. Now, after several years of LHC operation, 13 TeV collision data have been used to study detector behaviour and trigger capabilities in further extreme conditions. Operations were important to assert system stability, debug hardware, synchronise electronics, and ultimately obtain a measurement of detector performance. In the present chapter, RPC detector performance studies are presented. In section 5.2, results obtained with cosmic data, collected with the nominal magnetic field strength of 3.8 T and the tracking system on, are reviewed, while in the subsequent sections, performance results using the 2015/2016 LHC collision data are shown. In the last section are shown the results from dedicated studies based on the current performance of the detector, predicting expected rates and currents at high luminosity LHC (HL-LHC) conditions where the luminosity will be $5\text{x}10^{34}$ cm^{-2} s^{-1}.

5.1 DT and CSC Segment Extrapolation

The RPCs are used as trigger detectors in the CMS Muon System, having a very high time resolution, while the DTs and CSCs are used as tracking devices providing the needed space resolution. The RPCs do provide some tracking information as well. This redundancy between the RPCs and the tracking detectors is very suitable for efficiency measurements and other performance studies.

At local reconstruction level in a DT or CSC chamber, a track is characterised by fitting internal hits to a straight line defined by a position and a direction, constituting what is called a "segment".

The CMS muon system was designed with alternating layers of tracking (DTs and CSCs) and trigger (RPCs) detectors where every RPC chamber is located next to a tracking chamber. The extrapolation of a segment reconstructed by one of those chambers should point to an RPC strip and even more to a particular location within the strip. In addition, the information reported by the RPC should be consistent with segment extrapolation. This allows implementation of methods for determining the efficiency, understanding the hit cluster-size, surveying the geometry, performing FEB connectivity tests and carrying out alignment studies.

In order to estimate the error in the extrapolation between the tracking chamber and the RPC surface, a Monte Carlo study was performed with 10 000 di-muon events coming from the vertex with a momentum of 100 GeV. The extrapolated point was compared with the simulated muon hit on the RPC surface. The distribution of the differences between those two points (residuals) gives a way to estimate the error in the procedure.

When a segment is reconstructed, the number of hits used and the χ^2/n of the fit, define two quality factors that can be used in this kind of studies as selection criteria for the sample. In the plots mentioned above, no segment quality selection

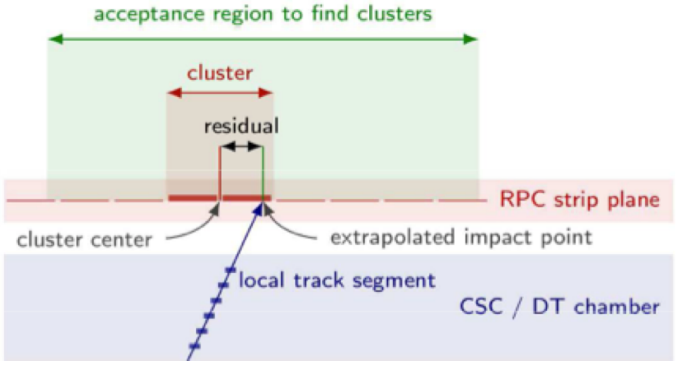

Figure 5.1: Sketch of the segment extrapolation technique.

was applied for the case of the barrel, while for the case of the endcap, only segments with a number of reconstructed hits between 4 and 10 were used.

In the barrel region of the muon system are 4 layers of DT chambers, where each layer is composed of 3 super-layers which provide the information for the z coordinate of the segment. Combining information from the three super layer allows reconstruction of a complete three-dimensional segment in that layer. However this situation changes in the outer-most layer where the super layer providing the z coordinate information is missing and has to be obtained from the previous layer instead. More details of this technique can be found in [61].

5.2 Study of Cosmic Data

To commission the experiment for extended data taking, the CMS conducted a month-long data taking exercise in beginning of 2015, called as the Cosmic Run at Full Tesla (CRAFT15). Data recorded by RPCs during CRAFT15 (3.8 x 10^7 cosmic rays triggered events) are analyzed here using RPC offline performance tools and thus detector and trigger behaviours are studied.

Average intrinsic detector noise, cluster size and efficiency were computed and compared to the results of the cosmic rays data taken in 2012. This study also

indicated a few hardware failures and cable map errors which have now been fixed.

This plot shown in Fig. 5.2 is called the XY view occupancies for one of the barrel wheels. The RPC local reconstruction is crucial for various detector studies and for some physics analysis such as a study of heavy stable charged particles [62]. The code can be consulted in the official CMSSW repository [63]. The plot shows the position of the reconstructed muon hits on the RPC detectors. These plots are used to monitor the detector performance. When the geometry of the RPC detector becomes visible we know that the detectors are working properly. The data used for these plots comes from cosmic and 13 TeV collision muons; this data was taken with a magnetic field of 3.8 Tesla. Small interruptions in the black lines are due to RPC detectors that were turned off for commissioning activities on the Gas system. Occupancies and other performance parameters for all the other wheels can be found in detail in [64]

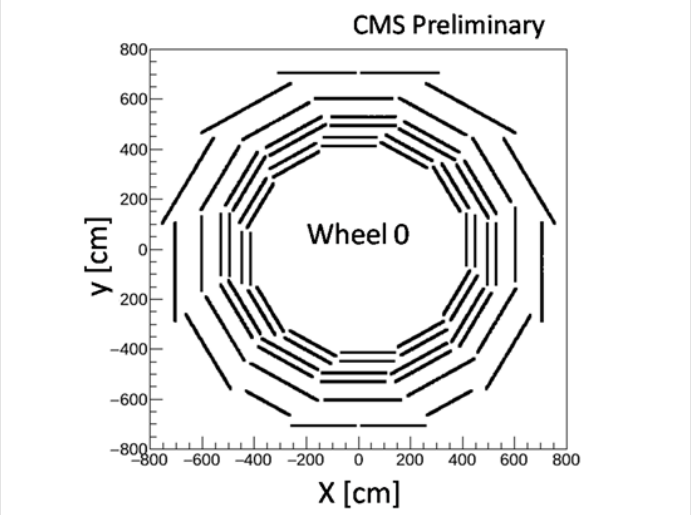

Figure 5.2: RPC muon hit occupancy.

The intrinsic chamber noise and background radiation levels could have an impact on the performance of the system as high rates can affect trigger performance and reconstruction of the muon tracks. The RPC rate is also measured during the cosmic data taking between collisions runs. Average intrinsic noise changes in 17-02-2015 is

presumably due to threshold settings changes, and it keeps the new average trend during the upcoming period. Fig. 5.3 represents the history of rate level in barrel, endcap and system average from 2011 to 2015. Fluctuations in the rate are mainly due to post-collisions radiation, threshold value optimization vs efficiency and operating channels number change. Though the blue and the green curves show similar drift behaviour, no significant spike correlations are observed. The overall trend show minor increase in the system rate with time, which is well below the official CMS requirement of rate $< 5\ Hz/cm^2$. The end points of the barrel and endcap curves (2015 data taking) get close together since we have lower noise in the RE4 (around 0.05) which lowers the average of the measured endcap rate.

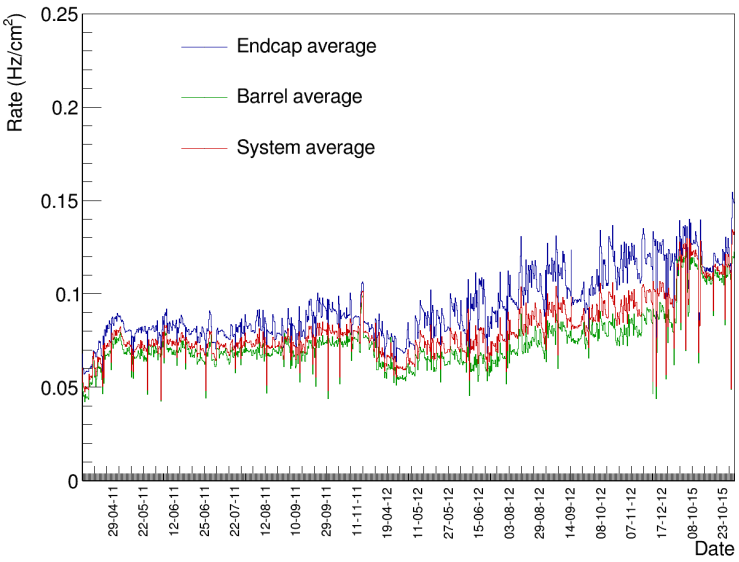

Figure 5.3: RPC cosmic rate distribution.

The cluster size is defined as the number of consecutive strips fired when a muon crosses a single RPC detector. This quantity was measured with Cosmic muons during 2015 and it was found to be around 1.7. This value is in agreement with previous measurements performed with 2012 Cosmic muons as shown in Fig. 5.4. This stability

is important to keep a stable RPC trigger since an increase in the cluster size values will increase the probability of having fake RPC triggers.

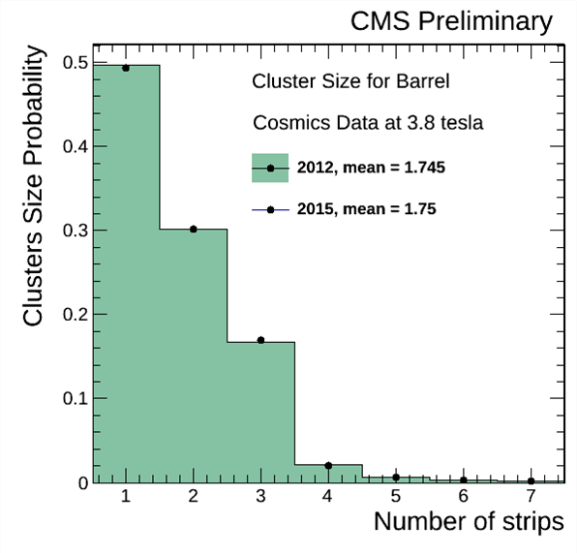

Figure 5.4: RPC system intrinsic noise.

5.3 RPC Performance during RUN-I and RUN-II

5.3.1 RPC Monitor Data Skim

To study RPC performance, a carefully tailored data skim has been adopted, the RPC 2015/16 - 13 TeV COLLISIONS SKIM, based on the official /MuMonitor/ dataset, recorded by CMS in p-p collisions at a centre-of-mass energy of 13 TeV. In particular, /MuMonitor/ is a collection of events triggered by a selection of single-muon triggers and intended for monitoring purposes.

Selected events contain at least one high quality muon reconstructed in both tracking and muon system (global muon) with at least one valid hit in the muon chambers. A detailed description of muon track reconstruction in CMS can be found here [65]. Only muons with $\eta < 1.6$, corresponding to RPC geometrical acceptance, are considered.

5.3.2 RPC Working Point Calibration

A high voltage (HV) calibration scan was performed every year: recording collision data at several HV settings to define the operating voltage for every single chamber separately, called working point (WP). Details can be found in [66, 67] for a full explanation of the HV scan and dependence of efficiency on the HV, including the analysis and methodology. Effective HV equation (5.3.1) shows the dependency of the avalanche production on the environmental pressure P, temperature T and the applied HV.

$$HV_{eff}(P,T) = HV(P_0/P)(T/T_0) \tag{5.3.1}$$

Where HV_{eff} [68] is effective high voltage, HV is applied high voltage, and the reference temperature and pressure are $T_0 = 293$ K and $P_0 = 965$ mbar.

The efficiency ϵ dependence with respect to the HV_{eff} is followed by a sigmoidal shape (5.3.2).

$$\epsilon = \frac{\epsilon_{max}}{1 + e^{\lambda(HV_{eff} - HV_{\epsilon=\epsilon_{max}/2})}} \tag{5.3.2}$$

where ϵ_{max} is the maximum efficiency reached by the chamber when HV reaches ∞ . The three parameters of the fit are:

- maximum fit efficiency labeled ϵ_{max}
- voltage at which the measured efficiency is 50% of maximum efficiency ($HV50$)
- slope of the sigmoid rise at HV50 (Slope50)

An typical efficiency curve for a chamber is shown in Fig. 5.6. It is crucial to define the operational HV of all detectors in the plateau region of sigmoid to get a high and stable efficiency. A software miniscan was performed every 20V from the knee to give the efficiency and cluster size at working point for every WP definition for the Barrel, the old RE1, RE2, RE3 Endcap stations and the lately installed fourth

muon station RE4 as shown in Fig. 5.5. The miniscan is used to define the best WP definition in the interval of physically required values, based namely on the efficiency and cluster size. RPC chambers should have efficiency greater than 95% and cluster size below 2 signal electrodes (strips) to avoid trigger in-ambiguity. The lower limit of the WP interval is defined as the voltage at which the efficiency becomes greater than 95%. The upper limit is defined as the voltage at which the cluster size becomes greater than 2 strips. Working point (WP) is finally defined as

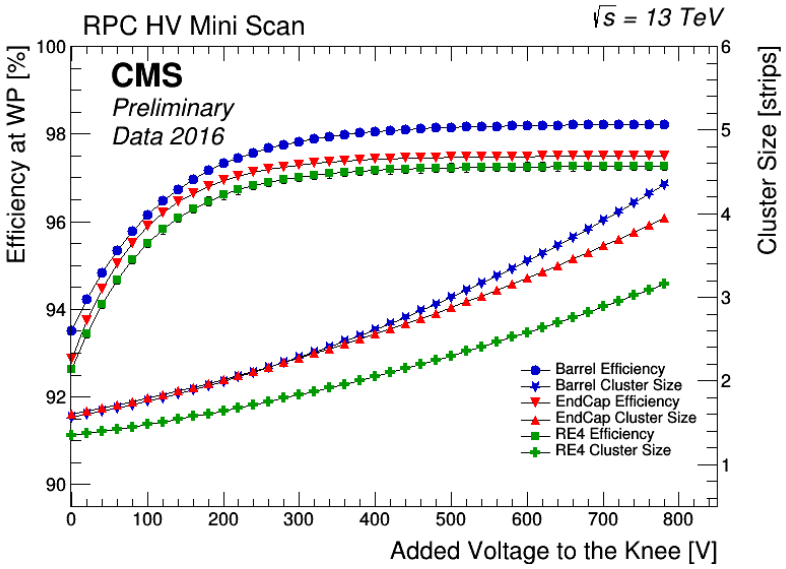

Figure 5.5: Efficiency and cluster size at working point for every WP definition for the Barrel (in blue), the old RE1, RE2, RE3 Endcap stations (in red) and the lately installed fourth muon station RE4 (green).

- Barrel $WP = HV_{knee}$+ 100 V
- Endcap $WP = HV_{knee}$ + 120 V

where HV_{knee} is the high voltage at which a chamber reaches 95% of the plateau efficiency.

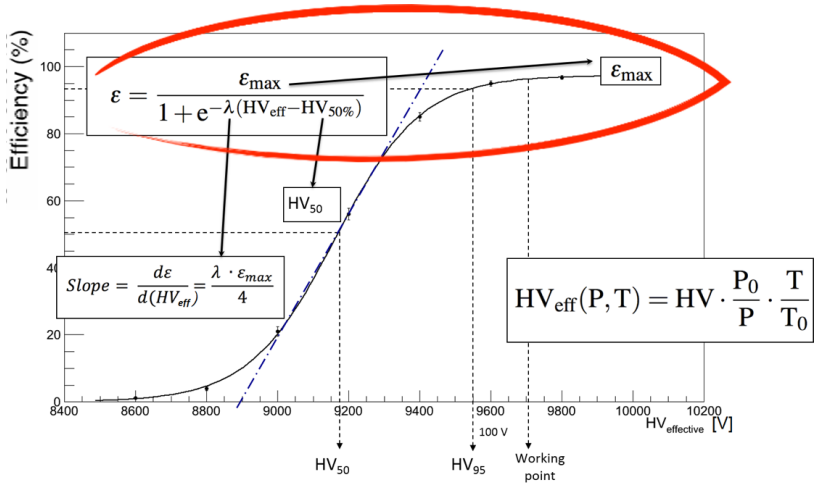

Figure 5.6: HV Scan Parameters.

The plots represent the working point, the efficiency at the working point from the fit evolution and the Voltage at 50% Efficiency evolution in the Barrel as shown in Fig. 5.7 and in the Endcap as shown in Fig. 5.8. The efficiency at WP distributions have been represented in light blue while a blue, full circle represents the mean efficiency at WP for each of the HV scans. By red, full squares is represented the mean of the working point distribution for each HV scan with their Standard deviations. In magenta, full triangles represent the mean of the voltage at 50% efficiency distribution for each HV scan with their standard deviations. No significative variations has been observed in the average working points over the years.

The small difference in HV between barrel and endcap detectorss depends on few differences in the assembly parameters and the definition of the working point. The distributions for 2011, 2012 and 2015 given in Fig. 5.9 show no evident ageing effect.

5.3.3 Synchronisation

For efficient triggering, all parts of the CMS detector must produce synchronous trigger signals for the same event. Delay of RPC signals with respect to the Level-1

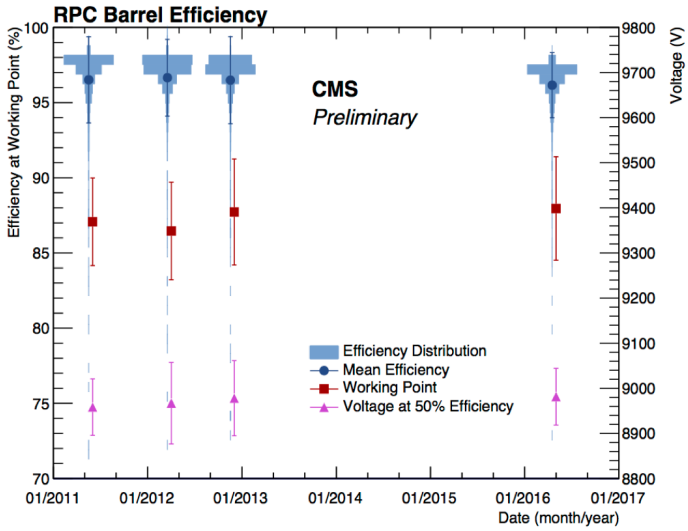

Figure 5.7: Efficiency at the working point from the fit evolution and the Voltage at 50% Efficiency evolution in the Barrel.

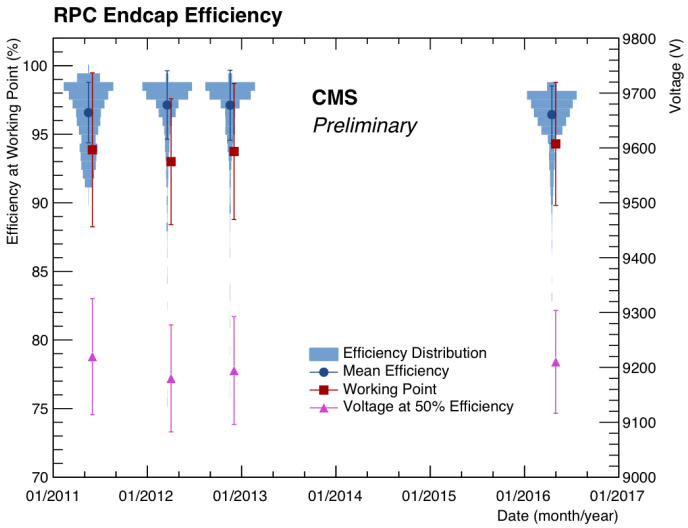

Figure 5.8: Efficiency at the working point from the fit evolution and the Voltage at 50% Efficiency evolution in the Endcap.

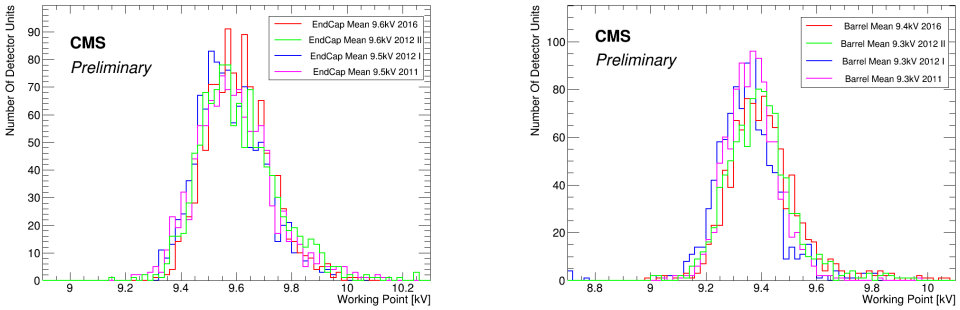

(a) (b)

Figure 5.9: HV_{eff} distributions for endcap (a) and barrel (b) as measured at the 95% $efficiency$.

Trigger signal has been studied for each and every eta partition. Data misalignment may have negative effects on detection and reconstruction efficiency. Delay of RPC trigger signal with respect to the Level-1 Trigger is shown in Fig. 5.10a for barrel and Fig. 5.10b for positive endcap stations. The delay is given in units of bunch crossing (25 ns). All hits in the central bin correspond to synchronised entries while those in other bins correspond to delayed signals coming from background noise.

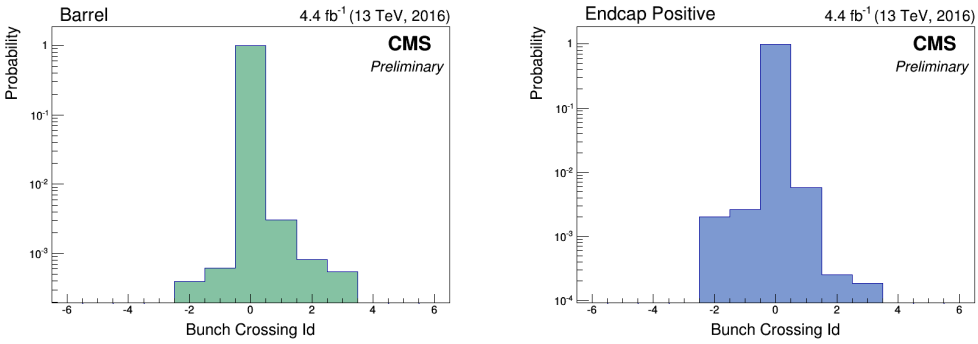

(a) (b)

Figure 5.10: Delay of the RPC signals with respect to the Level-1 Trigger signal for barrel (a) and for positive endcap stations (b)

5.3.4 RPC Hit Resolutions

The residuals are defined as a difference between the extrapolated point and the centre of cluster related to the matched RPC hit as shown in Fig. 5.1. The plots in Fig. 5.11 represent the residuals for all RPC barrel layers. The order of layers corresponds to the distance from the beam pipe, where layer 1 is the closest to it and layer 6 is the outermost. The plots in Fig. 5.12 represent the residuals for RPC endcap stations. The order of roll names corresponds to the distance from the beam pipe, where Rolls C of rings 2 are the closest to beam while Rolls A of rings 3 are the outermost. The residual distributions have been fit to Gaussian distributions and the obtained mean and standard deviation are given on the plot. The obtained standard deviations are in agreement with the expected spacial resolution and less than one strip pitch of the strip for a given layer.

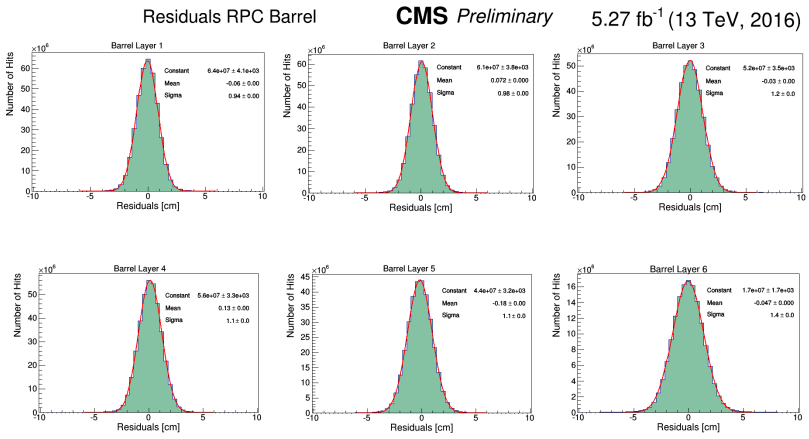

Figure 5.11: Residuals for 6 barrel layers.

5.3.5 CMS RPC Active Channels

Before proton beam were injected for collisions, the intrinsic noise rate was measured and thresholds were tuned for noisy strips and strps were disabled where needed. Fig. 5.13 shows the fraction of channels not operational during 2015. The blue line

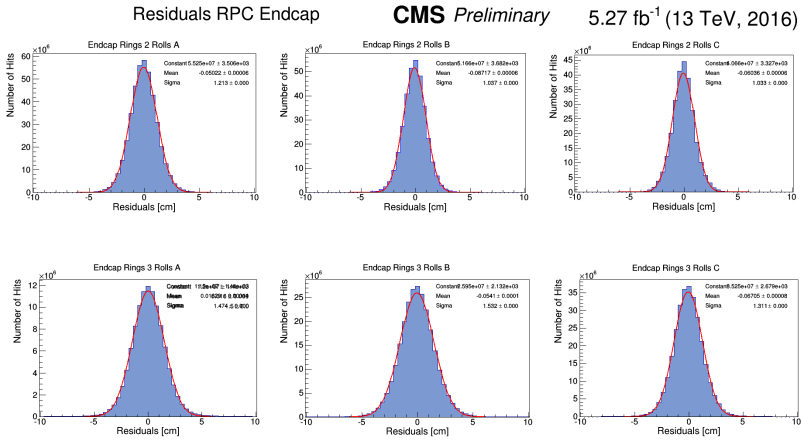

Figure 5.12: Residuals for RPC endcap stations.

represents the number of inactive (non responsive) channels, while the green line represents number of the masked strips that changes with time as they are adjusted per run depending on the performance of the system. The observed peaks related to the bigger number of masked strips are caused by the temporary hardware problems, which were successfully resolved. In 2015, the percentage of inactive channels was stable between 2 and 2.5%

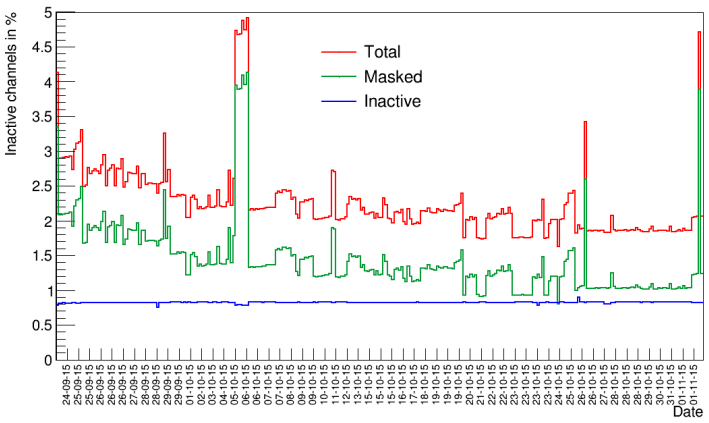

Figure 5.13: Fraction of channels not operational during 2015.

5.3.6 RPC Cluster Studies

RPC cluster size (CLS) is defined as the number of adjacent strips fired when an avalanche is produced in the RPC. Keeping the cluster size stable over time was one of the greatest successes achieved at the end of RUN-I [69]. RPC system has a stable average cluster size of about 1.8 strips over the years, which is in agreement with the CMS TDR [70]. During RUN-II, the chamber cluster size was monitored run-by-run to guarantee the stability of the system.

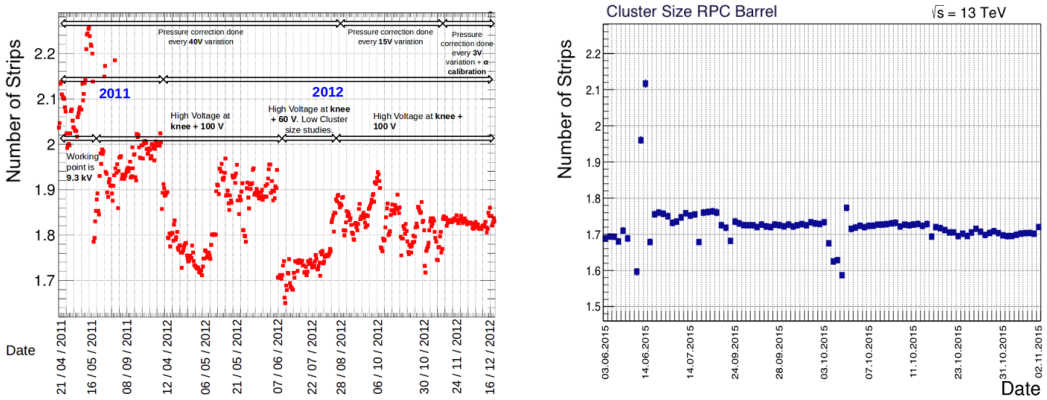

(a) (b)

Figure 5.14: The plots represent the history of the mean Cluster Size for the barrel for 2011 and 2012 physics data taking at 8 TeV in (a), and for 2015 at 13 TeV in (b).

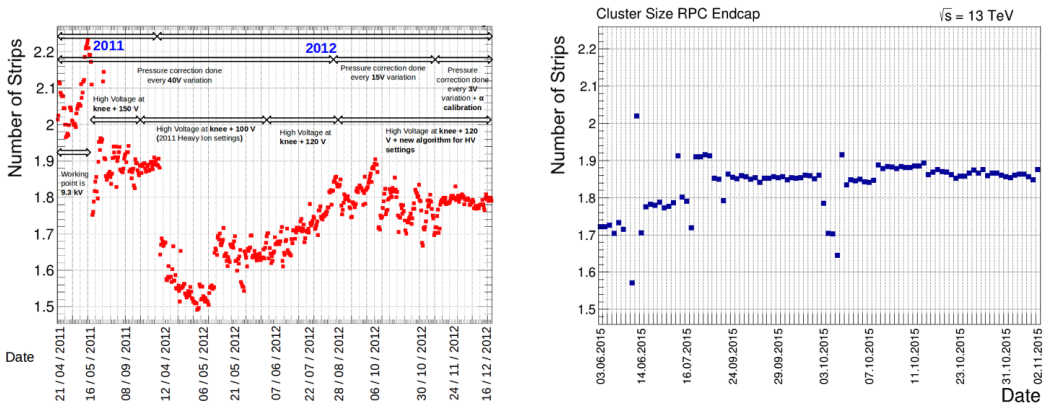

(a) (b)

Figure 5.15: The plots represent the history of the mean Cluster Size for the endcap for 2011 and 2012 physics data taking at 8 TeV in (a), and for 2015 at 13 TeV in (b).

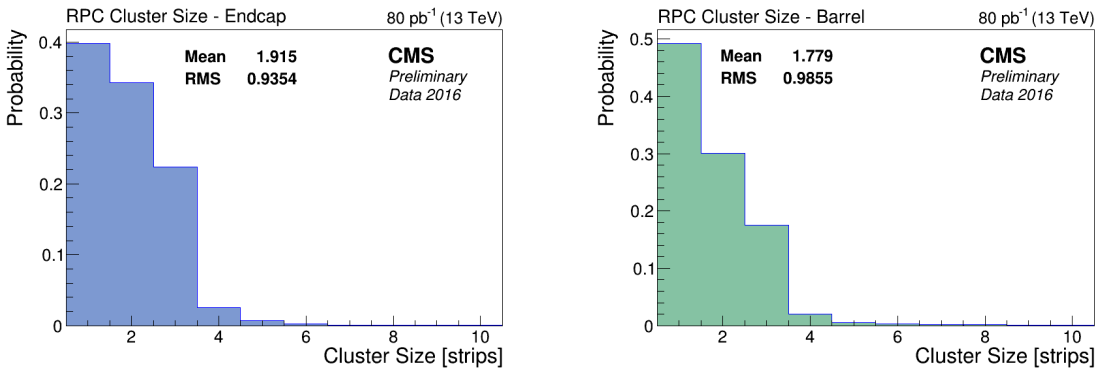

(a) (b)

Figure 5.16: End-cap average cluster size (a) and Barrel average cluster size (b).

Average CLS history in 2011 and in the start of 2012, as shown in Fig. 5.14 and Fig. 5.15, is affected by applied pressure corrections and several HV settings. During 2011 and the beginning of 2012, the applied HV to every RPC detector was corrected to compensate for pressure changes in the CMS cavern. The CLS at the end of 2012 was kept lower than 2011 to maintain a stable trigger rate. The fluctuation for 2015 in the middle of June and beginning of October, are due to the performed HV and

threshold scans. Fig. 5.16 shows the cluster size distributions for the end-cap and barrel measured during 2016.

5.3.7 RPC Efficiency

The segment extrapolation method described in section 5.1 is used to calculate the RPC efficiency. RPC efficiency depends on the atmospheric pressure in the cavern. In order to compensate this dependence, automatic corrections to the HV have been applied during the data taking. Chambers efficiency 2d map for 2015 data for one of the abrrel wheels and for one of the endcap disks is shown in Fig. 5.17. Vast majority of the detectors have average efficiency of more than 94%.

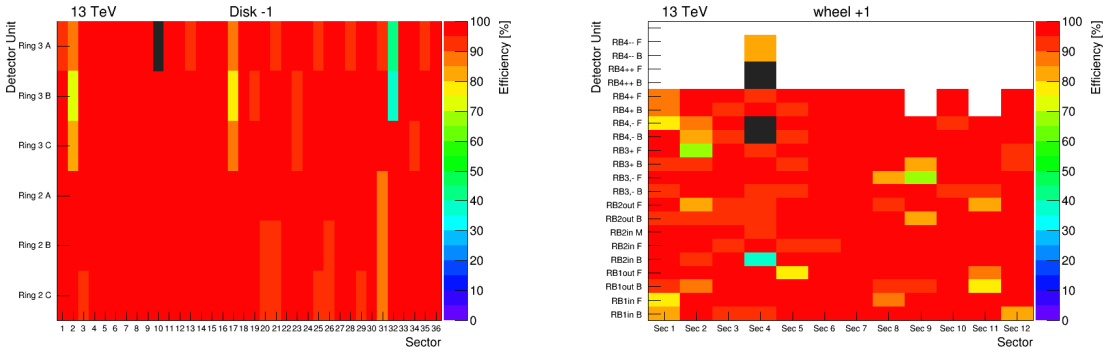

(a) (b)

Figure 5.17: Chambers efficiency 2d map for the endcap disk -1 (a). The 36 sectors are shown on x axis and the 6 η partitions on y axis. Chambers efficiency 2d map of barrel wheel +1(b). The plot represents the 12 sectors on x axis and the 6 RPC layers on y axis (RB1in, RB1out, RB2in, RB2out, RB3, RB4). For both, the black entries correspond to the detector units which are switched off due to known hardware problems

Local efficiency measurement is also performed for every partition called as a "roll" of every chamber. Fig. 5.18 shows an example of a barrel and an endcap roll with high (average efficiency = 98%) and uniform efficiency. The typical trapezoidal shape for the endcap and rectangular shape for the barrel roll is clearly seen. The

lower efficiency regions, visible as small yellow spots, are due to the PVC spacers. Local efficiency for every single roll was compared with the same from previous years by developing a sophisticated algorithm to see any degradation in any part of the detector. No ageing effect (any trend in decreasing efficiency) was observed except for some minor regions of the detectors which are working with known hardware problems.

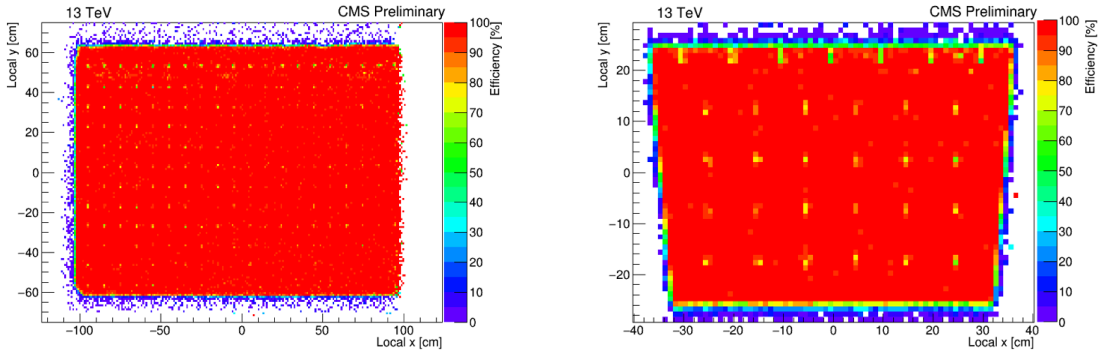

(a) (b)

Figure 5.18: The plots represent the efficiency vs the local impact point on the RPC surface for one of the barrel (a) and one of the endcap (b) detector units. The Y axis is along the strip length. Due to the geometrical issues there are no extrapolated hits in the area corresponding to $x >= 98\ cm$ on the left plot and because of this the efficiency is not calculated for it.

Fig. 5.19 shows the latest measurement of chamber efficiency. The distribution is obtained using 2016 collision data at $\sqrt{s} = 13\ TeV$, B = 3.8 T and an integrated luminosity of about 80 pb^{-1}. The mean RPC efficiency was calculated to be 94.6 % - 95.1 %. The few chambers with low efficiency have known hardware problems.

Efficiency is affected by several HV settings and applied pressure corrections, during 2011 and beginning of 2012 as shown in Fig. 5.20 and Fig. 5.21. The fluctuation for 2015 in the middle of June and beginning of October, are due to the performed HV and threshold scans. Performance of the newest part of the RPC system (RE4

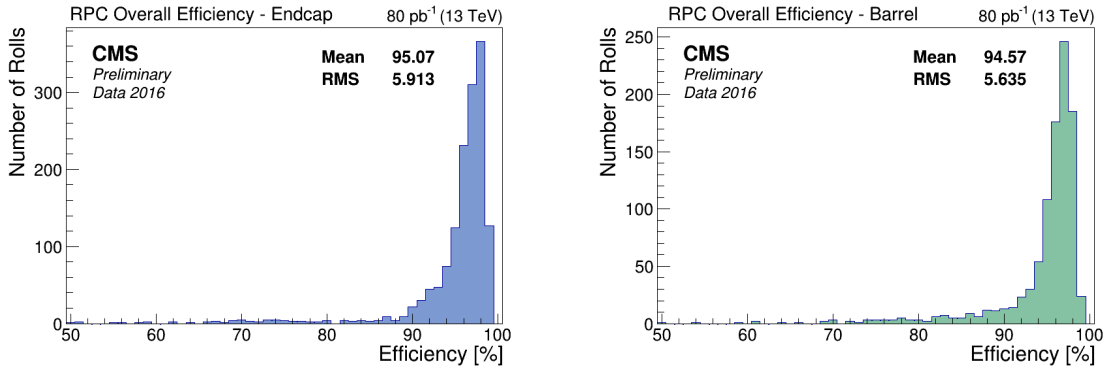

(a) (b)

Figure 5.19: End-cap chambers efficiency distribution (a) and Barrel chambers efficiency distribution (b).

stations) can be found in detail in [71]

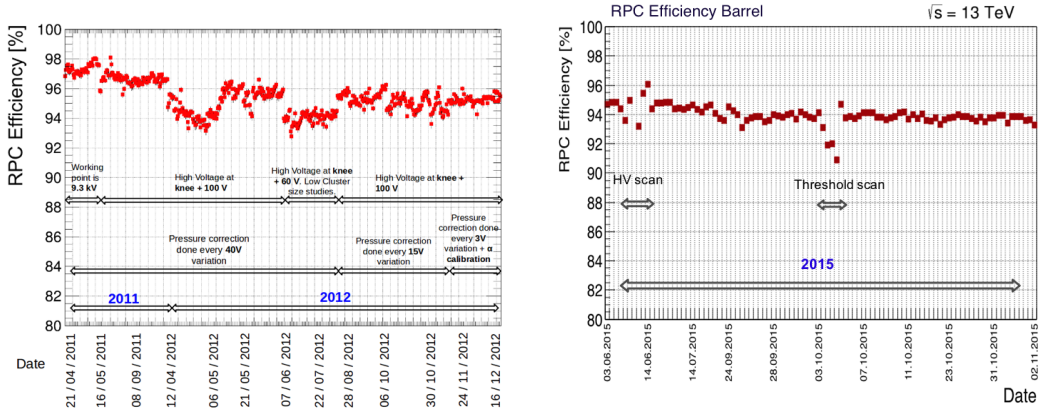

(a) (b)

Figure 5.20: The plots represent the history of the overall RPC efficiency for the barrel for 2011 and 2012 physics data taking at 8 TeV in (a), and for 2015 at 13 TeV in (b).

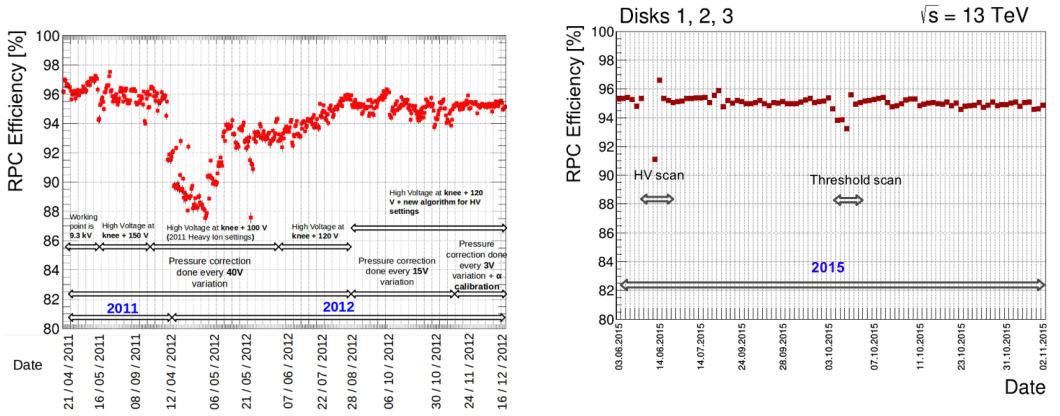

(a) (b)

Figure 5.21: The plots represent the history of the overall RPC efficiency for the endcap for 2011 and 2012 physics data taking at 8 TeV in (a), and for 2015 at 13 TeV in (b).

Average RPC efficiency during 2015 at 13 TeV was ≈ 94% after 1 year of LHC running as detectors were operated at lower working points. During 2015, the RPC system was running with a very stable efficiency.

5.3.8 RPC Background

Background radiation level in the CMS muon spectrometer is one of the key factors in the performance of the detectors. Low-momentum primary and secondary muons, gamma-rays, neutrons, and LHC beam-induced backgrounds could have an impact on performance of trigger and pattern recognition of muon tracks. In addition, huge radiation can also cause premature ageing of the detectors.

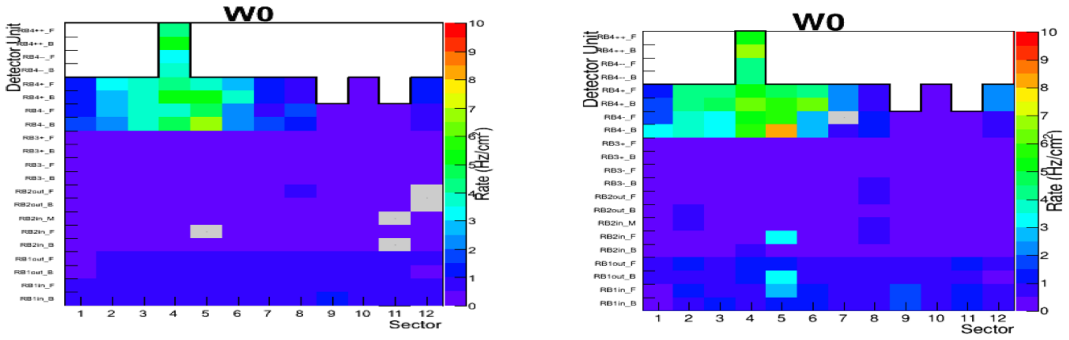

(a) (b)

Figure 5.22: The detector units hit rate (in Hz/cm^2) is shown for a run at average instantaneous luminosity of 4.5*10^{33} cm^{-2}s^{-1} for one of the barrel wheels in (a) at 8 TeV before 2013 and in (b) at 13 TeV during 2015. Detector units switched off are shown in gray. Blue and violet colours correspond to lower rates, while yellow, orange and red colours correspond to high background level.

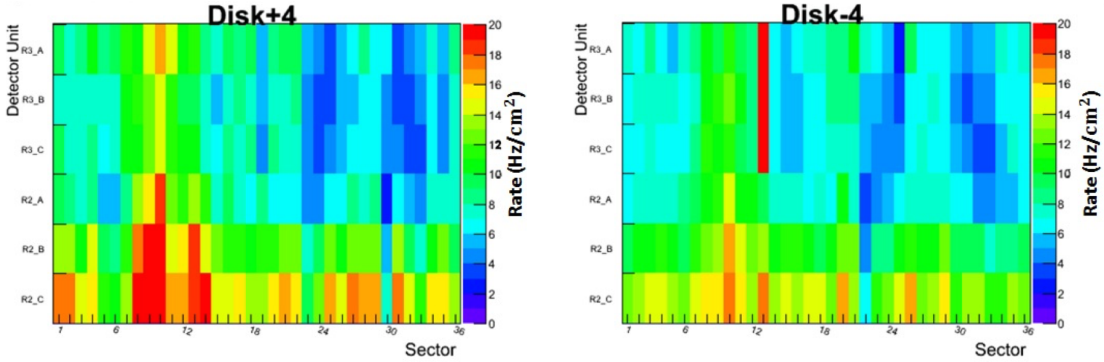

(a) (b)

Figure 5.23: The detector units hit rate (in Hz/cm^2) is shown for a run at average instantaneous luminosity of 4.5*10^{33} cm^{-2}s^{-1} for the newly installed RPCs for the positive station in (a) and for negative station in (b) during 2015 at 13 TeV.

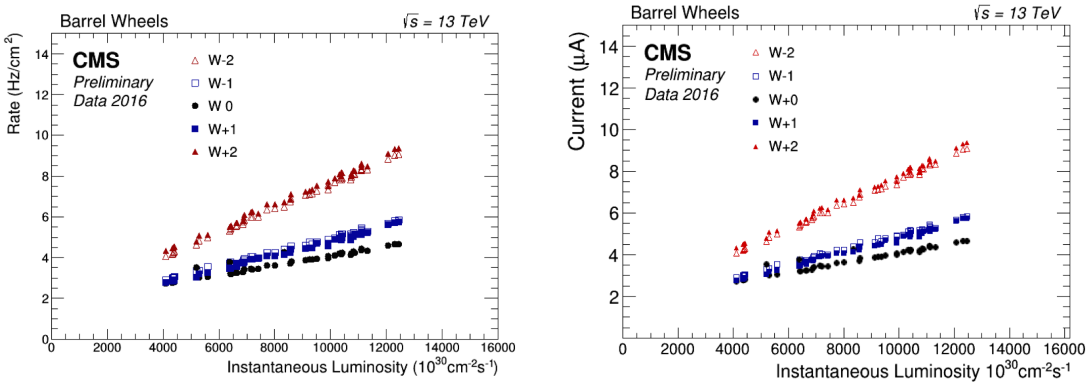

(a) (b)

Figure 5.24: The plots represent the average hit rate vs. instantaneous luminosity for all barrel wheels, with 2016 pp collisions at 13 TeV in (a) and currents vs. instantaneous luminosity in (b).

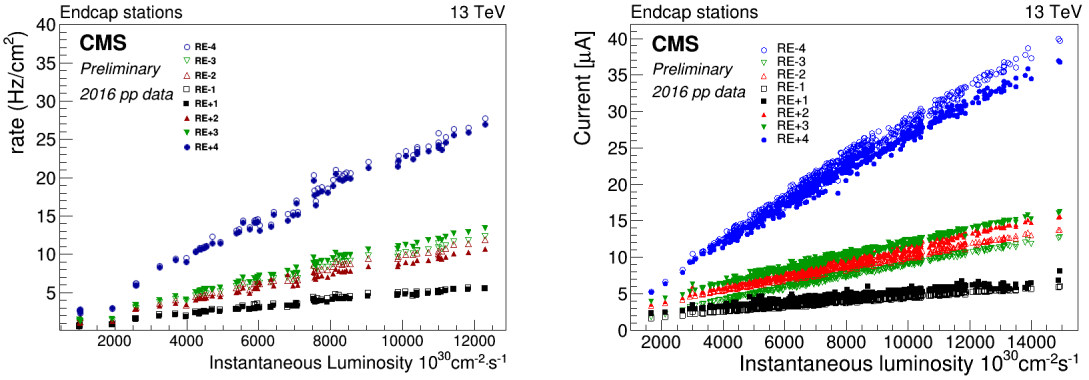

(a) (b)

Figure 5.25: The plots represent the average hit rate vs. instantaneous luminosity for all endcap stations, with 2016 pp collisions at 13 TeV in (a) and currents vs. instantaneous luminosity in (b).

Main contribution in measured RPC rate is coming from background. A plot is shown in Fig. 5.22 as an example of 2015 at 13 TeV with its comparison to 2012 at 8 TeV. The X-axis corresponds to the chamber number and there are 36 chambers per ring, while the Y-axis corresponds to the ring number and the names of the detector

units. Fig. 5.23 shows the measured rate for the recently installed endcap stations, where blue and violet colors correspond to the lower rates, while yellow, orange and red colors correspond to high background level. The average hit rate for the shown maps is 10 Hz/cm^2. The higher rate for higher eta regions is in agreement with previous measurements and as expected from Monte Carlo [61].

5.4 Data driven Predictions to HL-LHC Program

During HL-LHC (High Luminosity LHC) operation, the instantaneous luminosity should increase to 5x10^{34} cm^{-2} s^{-1}, with a corresponding increase of the background. The experiments are expected to collect an integrated luminosity of 3000 fb^{-1}.

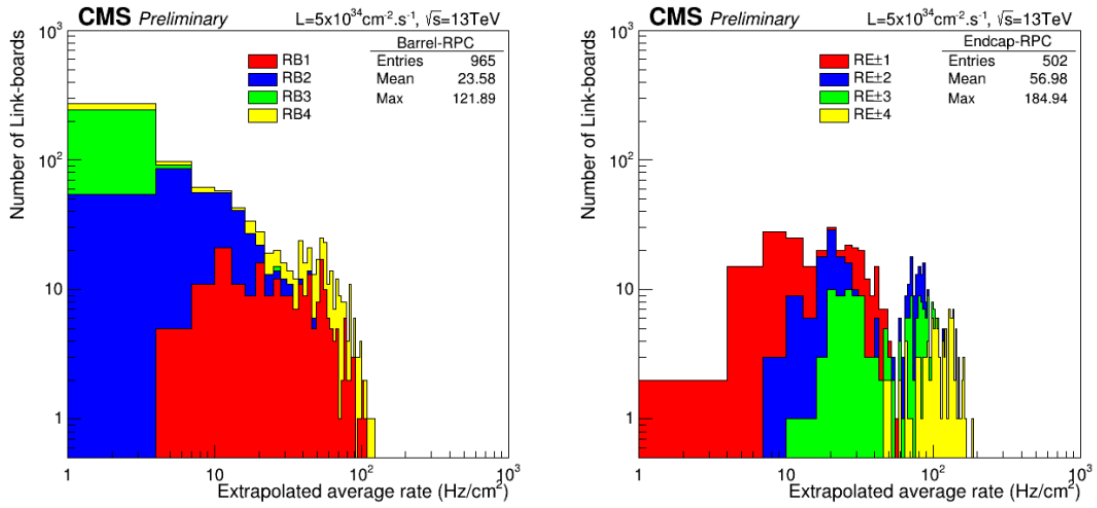

(a) (b)

Figure 5.26: Extrapolation from 2016 data of single hit rate per unit area to HL-LHC conditions, in the barrel (a) and endcap (b) regions, for the present RPC system.

Based on 2016 proton-proton collisions data, a linear dependence of the background rates as a function of the instantaneous luminosity was obtained for all barrel and endcap stations. RPC current and hit rate vs instantaneous luminosity dependencies for all barrel stations are shown in Fig. 5.24(a) and (b) and for all 8 endcap

stations in Fig. 5.25 (a) and (b) respectively. The dependencies show clear linear behaviour. Mean rate and currents values per run are respectively defined as the average rate of all the rolls and the average current on all HV channels present in the corresponding station, selected runs with identical LHC running parameters. Highest hit rate and currents have been measured in fourth endcap stations $-RE-4$ and $RE+4$, furthest from the interaction point, which are mostly affected by the background in the cavern. Rotating shielding on positive and negative ends were not symmetric in 2016 which contributed to relatively higher rates and currents in RE4 with respect to 2015 performance.

Table 5.1: RPC currents and rates per Barrel wheels and Endcap stations, extrapolated to HL-LHC conditions

Region	**Current** (μ A)	**Rate** (Hz/cm^2)
RE-4	135.1060	108.6190
RE-3	42.7914	48.4225
RE-2	41.0459	46.6811
RE-1	17.1378	21.3045
W-2	34.4768	26.5914
W-1	20.0554	18.3903
W0	14.8550	12.6072
W+1	19.6571	19.3545
W+2	35.7912	31.3384
RE+1	18.3773	21.07480
RE+2	46.6151	41.5868
RE+3	48.7422	52.1645
RE+4	125.1740	103.8110

Assuming the same linear relationship up to a luminosity of about one order of magnitude higher i-e 5x10^{34} cm^{-2} s^{-1}, the expected rates at HL-LHC conditions are shown in Fig. 5.26 for all barrel (a) and endcap (b) chambers. Full details of current and hit rate extrapolations for all barrel and endcap regions are shown in table 5.1, where maximum rate per unit area of about 200 Hz/cm^2 is expected. Background

simulations reproduce the measured rates within a factor of two. In the following we apply a safety factor of three and evaluate the performance up to a rate of 600 Hz/cm^2.

The RPC efficiency and cluster size have been measured in proton-proton collision runs in 2016 and 2017 as discussed in detail in the last sections. The plot shown in Fig. 5.27 represents the RPC barrel and positive endcap efficiency and cluster size w.r.t increasing instantaneous luminosity measured in proton-proton collision runs in 2016 and 2017 data taking. The lower efficiency and cluster size in barrel during 2016 are caused by the higher concentration of Isobutane in the gas working mixture in 2016. Nevertheless the comparison between the 2016 an 2017 results show stable efficiency and cluster size. The results were then extrapolated to the designed luminosity of HL-LHC and 0.8% of reduction in efficiency is found for barrel and 2% in the endcap which is consistent with the hit rate in the barrel and endcap as background rate in endcap is twice as that of barrel. No degradation has been observed for cluster size at HL-LHC conditions.

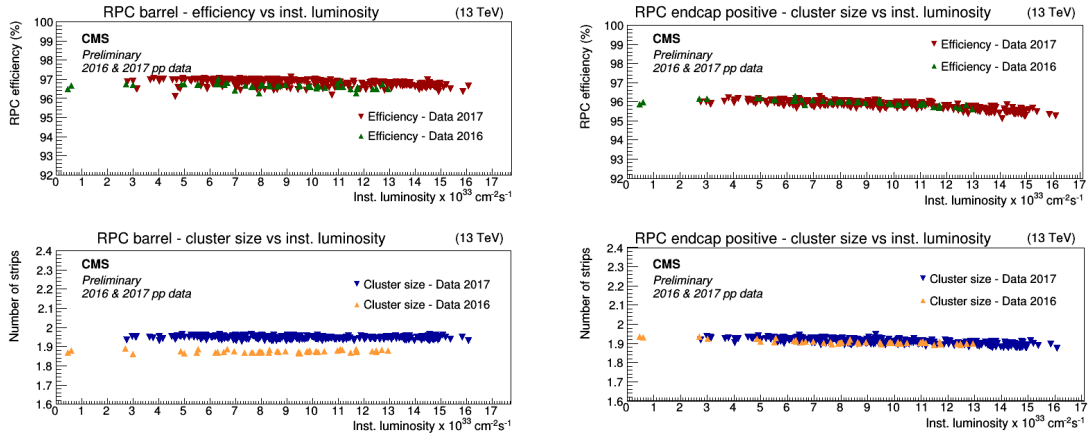

(a) (b)

Figure 5.27: RPC barrel efficiency and cluster size as a function of the instantaneous luminosity measured in proton-proton collision runs in 2016 and 2017 data taking for barrel in (a) and positive endcap in (b).

Chapter 6

The $t\bar{t}$ Event Selection

6.1 Introduction

As described in detail in 2, following analysis is done using $t\bar{t}$ candidate events with ℓ+jets, where leptons are either electrons or muons, and dilepton final states. In the former case, the cross section is extracted by a fit in different categories, while in the latter a simpler but more robust event-counting experiment approach is used. The two results are then combined in the final measurement. Top-quark pair production probes the gluon distribution in the proton. In particular, $t\bar{t}$ production at $\sqrt{s} = 5.02$ TeV accesses the high-x region at which the gluon distribution is not well understood. Improvements of our understanding of the high x gluon distribution are essential for accurate theoretical predictions for cross sections in the SM interactions and those beyond the SM at high energy experiments. The impact of $t\bar{t}$ cross section measurement on the uncertainty in the gluon distribution functions is represented through a next-to-next-to leading order (NNLO) QCD analysis.

6.2 Data, simulated samples and theoretical cross section

The presented analysis was done using $27.4 \pm 0.6\ pb^{-1}$ [72] CMS dataset. The presence of several proton collisions in the same or nearby events ("pileup") results in an average number of overlapping interactions estimated online to be 1.4, assuming a total inelastic cross section of 65 mb.

Several Monte Carlo (MC) generators are being used to simulate signal and background events. The NLO $POWHEG$ (v2) [34, 35] generator is used for $t\bar{t}$ events, assuming a value of 172.5 GeV for the top quark mass (m_{top}). These events are passed to $PYTHIA$ (v8.205) [73, 74] to simulate parton showering, hadronization, and the underlying event, using the CUETP8M1 [75] tune for the default $t\bar{t}$ MC sample. The NNPDF3.0 NLO PDFs with strong coupling $\alpha_s(M_Z) = 0.118$ at the Z boson mass scale M_Z are utilized in the MC calculations.

The $MadGraph5amc@NLO(v5\_2.2.2)$ generator [76] is used to simulate W boson production with additional jets (W+jets), and high-mass (> 50 GeV) Drell–Yan quark-antiquark annihilation into lepton-antilepton pairs through Z boson or virtual-photon exchange (referred to as "Z/γ^*"). The simulation includes up to two extra partons at matrix element level, and the FxFx merging procedure [77] is used to interface with $PYTHIA$. Low-mass Z/γ^* events (20–50GeV) are simulated with $PYTHIA$. The normalization of the W+jets and Z/γ^* processes is either derived from data (in the dilepton channel) or estimated based on the NNLO cross sections (in the ℓ+jets channel) from the $FEWZ$ program (v3.1.b2) [78]. Single top quark plus W boson events (tW) are simulated using $POWHEG$ (v1) [79, 80] interfaced with $PYTHIA$, and are normalized to the approximate NNLO cross sections [81]. The contributions from WW and WZ production (referred to as "WV") are simulated with $PYTHIA$, and are normalized to the NLO cross sections calculated with the

MCFM (*v*8.0) program [82]. All generated events undergo a full *GEANT*4 [83] simulation of the detector response.

The expected signal yields are normalized to the value of the SM prediction for the $t\bar{t}$ production cross section:

$$\sigma_{t\bar{t}}^{\mathrm{NNLO}} = 68.9\ ^{+1.9}_{-2.3}\ (\mathrm{scale}) \pm 2.3\ (\mathrm{PDF})\ ^{+1.4}_{-1.0}\ (\alpha_{\mathrm{s}})\,\mathrm{pb}\quad , \tag{6.2.1}$$

as calculated with the TOP++ program [84] at NNLO in perturbative QCD, including soft-gluon resummation at next-to-next-to-leading-logarithmic order [13], using the NNPDF3.0 NNLO PDF set, with $\alpha_{\mathrm{s}}(M_{\mathrm{Z}}) = 0.118$ and $m_{\mathrm{top}} = 172.5\,GeV$.

The systematic uncertainties in the theoretical $t\bar{t}$ cross section are associated with the choice of the renormalization (μ_{R}) and factorization (μ_{F}) scales–nominally set at $\mu_{\mathrm{R}} = \mu_{\mathrm{F}} = \sqrt{m_{top}^2 + p_{\mathrm{T},top}^2}$ with $p_{\mathrm{T},top}$ the top quark transverse momentum–as well as with the PDF set and the α_s value.

The uncertainty of 0.1% in the LHC beam energy [85] translates into an additional uncertainty of 0.22 pb in the expected cross section, with negligible impact on the acceptance of any of the channels included in this analysis.

6.2.1 Object reconstruction

Identification and reconstruction of all individual particles have been done by applying particle-flow (PF) algorithm [86] by collecting information from all the sub-system of the CMS detector. The electron momentum is calculated by combining the energy measurement in the ECAL system with the associated tracks momentum in the tracker. Spatially compatible photons with electron track has taken in consideration, bremsstrahlung photons produced by the accelerated electron. In $Z \to ee$ decays, electrons with transverse momentum $P_T \approx 45\,GeV$ have momentum resolution ranges from 1.7% for nonshowering electrons in the barrel region to the higher value, 4.5%, in the endcaps showering electrons [87]. Muon are reconstructed by combining the

information collected by the muon spectrometer and the silicon tracker. The resultant relative P_T resolution is better in the barrel, 1.3–2.0%, and in the endcaps it is 6% corresponding to muons with $20 < P_T < 100\ GeV$ within the range $|\eta| < 2.4$ [88, 89]. In case of charged hadron, the energies are measured from a combination of its tracker momenta and matching of zero-suppression effects corrected energy deposits in the ECAL and HCAL systems. Finally, the corrected energies from ECAL and HCAL systems give the corresponding neutral hadron energies. Missing transverse energy in an event is taken as negative vector sum of the momenta of all reconstructed PF candidates, projected onto the transverse plane of the proton beams. Its magnitude is denoted as $P_T^{miss}$and the jet energy corrections are propagated to the P_T^{miss}calculation.

In pp interaction, the primary vertex is taken as the sum of the highest value of physics-object P_T^2. Jets are taken as the physics objects, clustered using jet algorithm [90, 91].The isolation of electron and muon candidates from nearby jet activity is then evaluated as follows. For electron and muon candidates, a cone of $\Delta R = 0.3$ and 0.4, respectively, is constructed around the direction of the lepton track at the primary event vertex, where ΔR is defined as $\sqrt{(\Delta\eta)^2 + (\Delta\phi)^2}$, and $\Delta\eta$ and $\Delta\phi$ are the differences in pseudorapidity and azimuthal angle between the directions of the lepton and another particle. A relative isolation discriminant, I_{rel}, is calculated by the ratio between the scalar P_T sum of all particle candidates inside the cone consistent with originating from the primary vertex and the P_T of the lepton. In this sum, we exclude the P_T of the lepton candidate. The neutral particle contribution to I_{rel} is corrected for energy deposits from pileup interactions using different techniques for electrons and muons.

The trigger efficiency of the electrons/muons is measured by using a "tag-and-probe" technique as explained in Ref. [92]. The sample of $Z \to \mu^+\mu^-$ events used for muon efficiency extraction is selected by the same trigger requirement used by the main analysis. The $Z \to e^+e^-$ sample for electron efficiency extraction makes use of

events that satisfy a diphoton trigger. Details with trigger efficiency distributions and few fit results examples are shown in AppendixC. Finally by comparing the lepton selection efficiency in data and simulation, the event yield in simulation is corrected using data-to-simulation scale factors.

Jets are reconstructed from the PF candidates using the anti-kt clustering algorithm [90]. Jets closer than $\Delta R = 0.3$ to the nearest muon or electron are discarded. Jet energy corrections extracted from full detector simulation are also applied as a function of jet p_T and η [93] to data and simulation. A residual correction to the data is applied to account for the discrepancy between data and simulation in the jet response.

6.3 Event selection

The event sample is selected by a loose online trigger and further filtered offline to remove noncollision events, such as beam-gas interactions or cosmic rays. Collision events containing one high-P_T electron (muon) candidate are selected online by requiring values of $E_T(P_T)$ greater than 40 (15) GeV and of $|\eta|$ less than 3.1 (2.5). The measured trigger efficiency for each decay channel, relative to the final selection, is higher than 90%. In the ℓ+jets analysis, electron candidates are selected if they have $P_T > 40\,GeV$ and $|\eta| < 2.1$. Further identification and isolation criteria are applied to the electron candidates. Electrons reconstructed in the ECAL barrel (endcap) are required to have $I_{\text{rel}} < 4$ (5)%. Electron candidates in the $1.44 < |\eta| < 1.57$ region, i.e., in the transition region between the barrel and endcap sections of the ECAL, are excluded because the reconstruction of an electron object in this region is less efficient. Muons are required to have $P_T > 25\,GeV$ and $|\eta| < 2.1$. Additional identification criteria are applied and I_{rel} is required to be $< 15\%$.

$$I_{rel} = \frac{I^{\text{ch. h}} + \max\left[\left(I^{\gamma} + I^{\text{n. h}} - 0.5 I^{\text{ch. h PU}}\right), 0\right]}{P_T} \tag{6.3.1}$$

where $I^{\text{ch. h}}$, I^{γ} and $I^{\text{n. h}}$ and $I^{\text{ch. h PU}}$ are the sum of the transverse energies of the reconstructed PF candidates (charged hadrons, photons, neutral hadrons and charged hadrons associated to other vertices) and P_T is the lepton transverse momentum. Events are rejected if they contain extra electrons or muons identified using a looser set of identification criteria and have $P_T > 10$ or $15\,GeV$, respectively.

The distinct signature of two b jets, expected in $t\bar{t}$ decays, is rare in background events, and thus is exploited in the ℓ+jets analysis. Backgrounds from W+jets, QCD multijet, and Z/γ^* events are controlled by counting the number of b jets in the selected events. In addition, two light-flavor jets are expected to be produced in the decay of one of the W bosons for signal events. The correlation in phase space of these light jets carries a distinctive hallmark with respect to the main backgrounds. To that end, jets are selected if they have $P_T > 30\,GeV$ and $|\eta| < 2.4$. The event selection requires at least two non-b-tagged jets to be identified as candidates from the W boson hadronic decay. More jets passing the b quark identification criteria are counted and used to classify the selected events in none (0 b), exactly one (1 b), or at least two ($\geq$2 b) tagged jet categories. The efficiency of the b jet identification algorithm is measured *in situ*, simultaneously with the signal cross section.

Dilepton events are required to have at least one muon at trigger level. No requirement on the presence of electron candidates is made at trigger level owing to the relatively high-E_T threshold (40 GeV) of the trigger. Electrons are selected if they have $P_T > 20\,GeV$, $|\eta| < 2.4$, and $I_{\text{rel}} < 9$ (or 12)% if in the barrel (or one of the endcaps). As in the ℓ+jets channel, electrons detected in the transition region between the barrel and endcap sections of the ECAL are excluded. Muons are required to have $P_T > 18\,GeV$, $|\eta| < 2.1$, and $I_{\text{rel}} < 15\%$. At least two jets satisfying the criteria $P_T > 25\,GeV$ and $|\eta| < 3$ are required. Events are subsequently selected if they have

a pair of leptons with opposite charge (($e^{\pm}\mu^{\mp}$)or ($\mu^{\pm}\mu^{\mp}$)) passing the requirements listed above. If additional lepton pairs manage to pass above mentioned selections, two oppositely charged leptons that yield the highest scalar P_T sum are selected.

Events with dilepton invariant mass of $M_{\ell\ell} < 20\,\text{GeV}$ are rejected.Events with couple of muons in the final state are still dominated by the Z/γ^* background. In order to suppress this contribution, events in the Z boson mass window of $76 < M_{\ell\ell} < 106\,\text{GeV}$ are vetoed in this channel. To further suppress the Z/γ^* events, a requirement on $P_T^{miss}$of $> 35\,GeV$ is imposed.

In both the ℓ+jets and dilepton analyses, events with τ leptons are considered as signal if they decay to any of the leptons which fulfils the selection requirements, and are included in the simulation.

6.3.1 The ℓ+jets final state

In the ℓ+jets analysis, the contributions of all background processes are estimated from simulation, with the exception of the QCD multijet background. Due to its large cross section, there is a non negligible contribution from the latter faking a $t\bar{t}$ event with ℓ+jets in the final state. Both the contribution from hard fragmentation of c and b quarks whose hadrons decay semileptonically, and the contribution from misidentified leptons, such as from either punch-through hadrons or collimated jets with a high electromagnetic fraction, can yield ℓ+jets-like topologies.

We made use of the expected $W \to qq'$ mass peak in $t\bar{t}$ events. We have explored this resonant dijet production inside a $t\bar{t}$ event in different ways: either by reconstructing its invariant mass (which should naturally peak closely to the W boson mass) or by inspecting how correlated the two jets are in the phase space. The reasons for this choice are the following:

- the backgrounds are non-resonant and their distribution is expected to have a

turn-on driven by kinematic requirements or a distribution resembling a combinatorial one or shaped by the recoil of the hard process.

- the signal distribution, being peaked at a well known resonance, can be used to further constraint in-situ the jet energy scale/resolution uncertainties

- the distribution is of interest in pPb and PbPb collisions, as a probe of the medium traversed by the final state particles of the $t\bar{t}$ decay

The selection of the two jets has been tested using the $t\bar{t}$ simulation by comparing different rankings:

- leading P_T jets - the two jets which maximize $P_T(j)$+$P_T(j')$

- leading dijet P_T- the two jets which maximize $P_T(jj')$

- closest in phase space according to a $FASTJET$-based metric - $\alpha = \frac{d_{ij}}{d_{iB}}$, where $d_{ij} = \min(k_{Ti}^{2p}, k_{Tj}^{2p}) \left(\frac{\Delta_{ij}}{D}\right)^2$, $d_{iB} = k_{Ti}^{2p}$ with p=-2, -1, 0, 1, 2, k_T being the transverse momentum of the jet, D=0.4, and Δ_{ij} a measurement of the distance between the two jets in the phase-space. For Δ_{ij} we have compared the performance obtained using ΔR, $\Delta\eta$ or $\Delta\phi$. For each we rank the dijet candidates by increasing α and then pick the one with lowest value of α as the candidate. In this process we notice that the values of p=-2, 0, 2 correspond to the anti-kt, Cambridge-Aachen and kt metrics. We also notice that the value of D is irrelevant for the purposes of ranking, as the metric only changes by an overall scale factor.

The comparison of the different rankings listed above is done using the generator-level jets which are not matched to b jet candidates. We compare the number of events under the W mass peak with the number of events off-peak, as well as the

RMS/mean of the dijet invariant mass distribution or of the distance (ΔR) to the closest W boson in the event.

In order to quantify the expected gain on the final measurement we have then chosen to compare the results of analysis performed with the following variables:

- simple counting
- m_{jj} by leading P_T
- m_{jj} by smallest ΔR_{jj}
- m_{jj} by smallest ΔR_{jj} and imposing $\Delta R\ < 2.0$
- ΔR_{jj}

Comparison of the results is shown in AppendixB, obtained before choosing the final variable to measure the cross section from.

The estimation of the QCD multijet background is separately performed for the events with 0, 1, or $\geq$2 b jets using a control region where either the muon candidate fails a looser isolation requirement ($I_{\text{rel}} < 20\%$) or the electron candidate fails the identification criteria. The choice of the QCD multijet control region has been made in such a way as to minimize the contamination due to the signal and W+jets events, while retaining a large number of events in the sample for the estimation of this type of background. The initial normalization of the QCD multijet contribution in the signal region is derived from events with $P_T^{miss} < 20\,GeV$ ("reduced-signal" region). Events in both the reduced-signal and control regions fulfilling this requirement are counted. After subtracting the expected contributions from non-QCD processes, the ratio between the numbers of events observed in the reduced-signal region and in the control region, is used as a transfer factor to normalize the QCD multijet background estimate. In both the electron and muon channels, a 30% uncertainty is assigned to

the estimate of the expected contribution from non-QCD processes, estimated after varying the QCD scales in the W+jets simulation. This uncertainty propagates as both a normalization and a shape uncertainty in the predicted distributions for the QCD multijet processes.

$$N_{\mathrm{SR}}(QCD) = [N_{\mathrm{CR}}(obs) - N_{CR}(non-QCD)] \cdot \frac{N_{\mathrm{SR}}^{E_T^{miss}<20}(obs) - N_{\mathrm{SR}}^{E_T^{miss}<20}(non-QCD)}{N_{\mathrm{CR}}^{E_T^{miss}<20}(obs) - N_{\mathrm{CR}}^{E_T^{miss}<20}(non-QCD)}, \tag{6.3.2}$$

where "SR"("CR") is signal (control) region and "obs" is the observed data. Scale factors applied to the control region distributions for QCD in order to normalize them in the signal region are summarised in table 6.1 along with the uncertainty assigned to the normalization.

Table 6.1: Scale factors applied to the data-driven estimations of the QCD multijets backgrounds. The uncertainty on the final normalization is shown in percentage.

Category	inclusive	=0 b-tags	=1 b-tag	$\geq$2 b-tags
		μ+jets		
SF_{QCD}	0.088	0.034	0.024	0.101
Uncertainty	31%	34%	29%	100%
		e+jets		
SF_{QCD}	0.0038	0.002	0.00088	0.0138
Uncertainty	34%	33%	30%	100%

Fig. 6.1 and 6.2 show the MET distributions in the CR and SR (including the re-scaled shape obtained from the CR for QCD). Conversely Figs. 6.3 and 6.4 show the transverse mass (muon+MET) distributions. In both cases we show the inclusive (prior to any jet selection) and the exclusive (two non b-tagged jets + N b-tagged jets) distributions. Fair agreement is observed for all categories in both variables. For higher number of b-tags the expected contamination from non QCD processes tends to be larger.

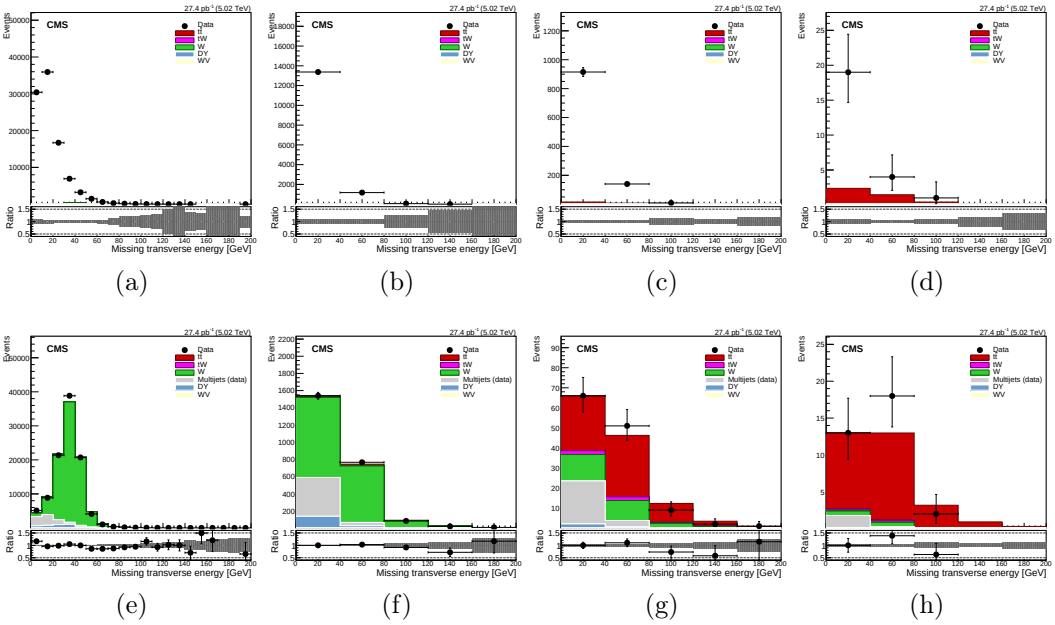

Figure 6.1: Distributions for the MET for non-isolated (top), and isolated (top) muon events. From left to right inclusive events and events with 0, 1 or at least 2 b-tagged jets.

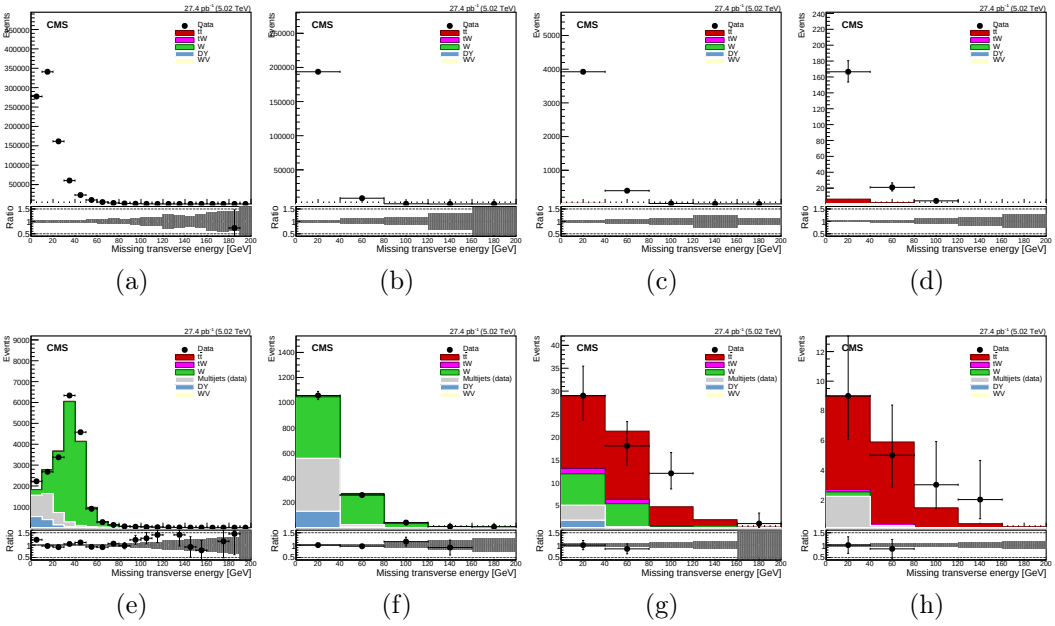

Figure 6.2: Similar to Fig. 6.1 for the electron channel.

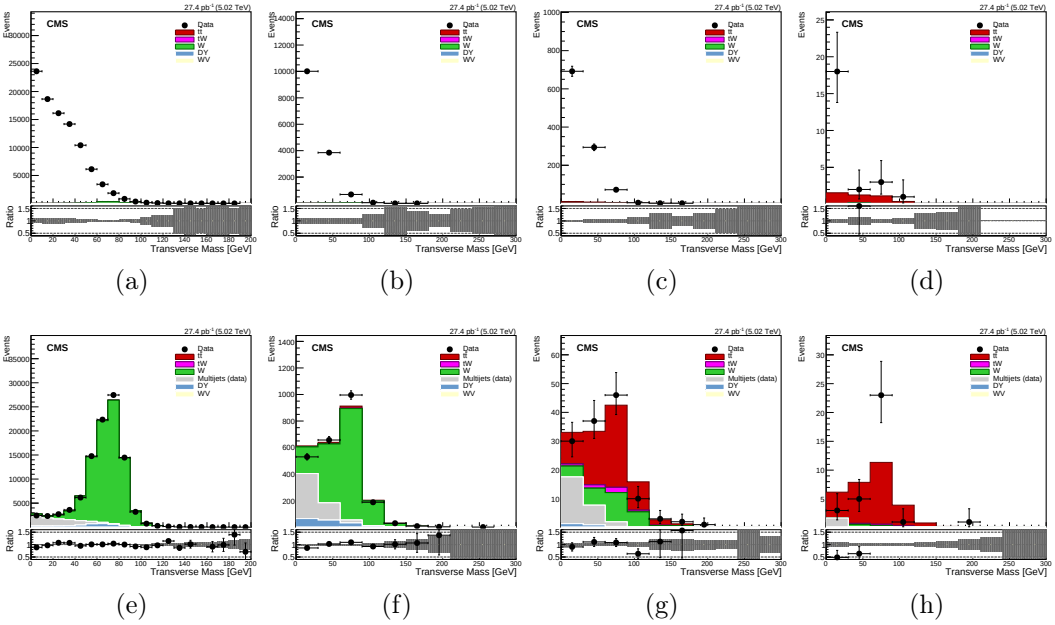

Figure 6.3: Similar as Fig. 6.1 for the transverse mass variable in the muon channel.

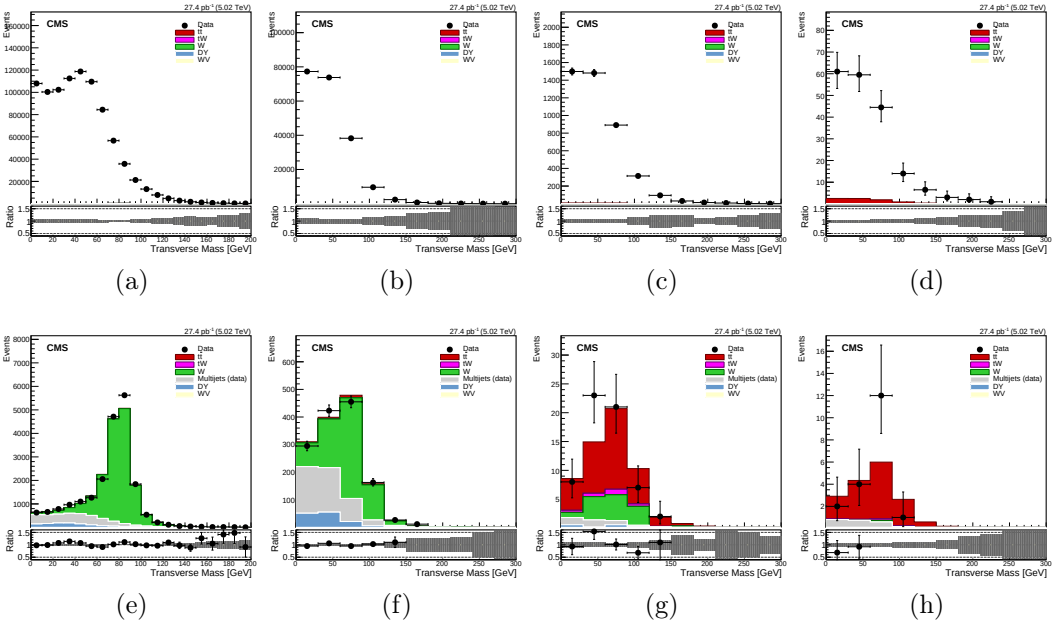

Figure 6.4: Similar as Fig. 6.1 for the transverse mass variable in the electron channel.

The variations are applied independently in the reduced-signal and control regions in order to determine an uncertainty envelope. A more accurate normalization for this contribution is obtained by the fit performed to extract the final cross section, described in Section 7.2.1.

6.3.2 The dilepton final state

Final states with two genuine leptons can originate from background processes, primarily from $Z/\gamma^* \to \tau^+\tau^-$ (where the τ leptonic decays can yield $(e^{\pm}\mu^{\mp})$or $(\mu^{\pm}\mu^{\mp})$plus P_T^{miss}due to the neutrinos), tW, and WV events. Other background sources, such as W+jets events or $t\bar{t}$ production in the ℓ+jets final state, can contaminate the signal sample if a jet is misidentified as a lepton, or if an event contains a lepton from the decay of b or c hadrons. These are included in the "$Non-WZ$" category, since genuine leptons are defined as originating from decays of W or Z bosons. The yields from tW and WV events are estimated from simulation, while the contribution of the Z/γ^* background is evaluated using control samples in data. The rate of $Non-WZ$ backgrounds is extracted from control samples in data for the $(e^{\pm}\mu^{\mp})$channel and is estimated from simulation for the $(\mu^{\pm}\mu^{\mp})$channel.

A scale factor for the Z/γ^* background normalization is estimated, as in Ref. [94], from the number of events within the Z boson mass window in data, which is extrapolated to the number of events outside the window. A scale factor of $0.91 \pm 0.14(stat)$ is obtained in the $(e^{\pm}\mu^{\mp})$channel, and $0.96 \pm 0.78(stat)$ in the $(\mu^{\pm}\mu^{\mp})$channel. The estimation is performed using events with at least two jets, and the dependence on different jet multiplicities is discussed in Section 7.1.

The $Non-WZ$ background in the $(e^{\pm}\mu^{\mp})$channel is estimated using an extrapolation from a control region of same-sign (SS) dilepton events to the signal region of opposite-sign (OS) dileptons. The muon isolation requirement is relaxed in order to enhance the number of events. The SS dilepton events predominantly contain at

least one misidentified lepton. The estimate for the $Non-WZ$ background is found to be $1.0 \pm 0.9(stat)$ events, where the central value comes from the estimation using events with at least two jets. No particular dependence of this scale factor is observed for different jet multiplicities within the large statistical uncertainty.

6.3.3 Control distributions

For ℓ+jets analysis pre-fit control distributions for different variables in events with 0, 1 or at least 2 b-tagged jets and two non-b-tagged jets are shown below. The lepton P_T and η are illustrated in Fig. 6.5, 6.6.

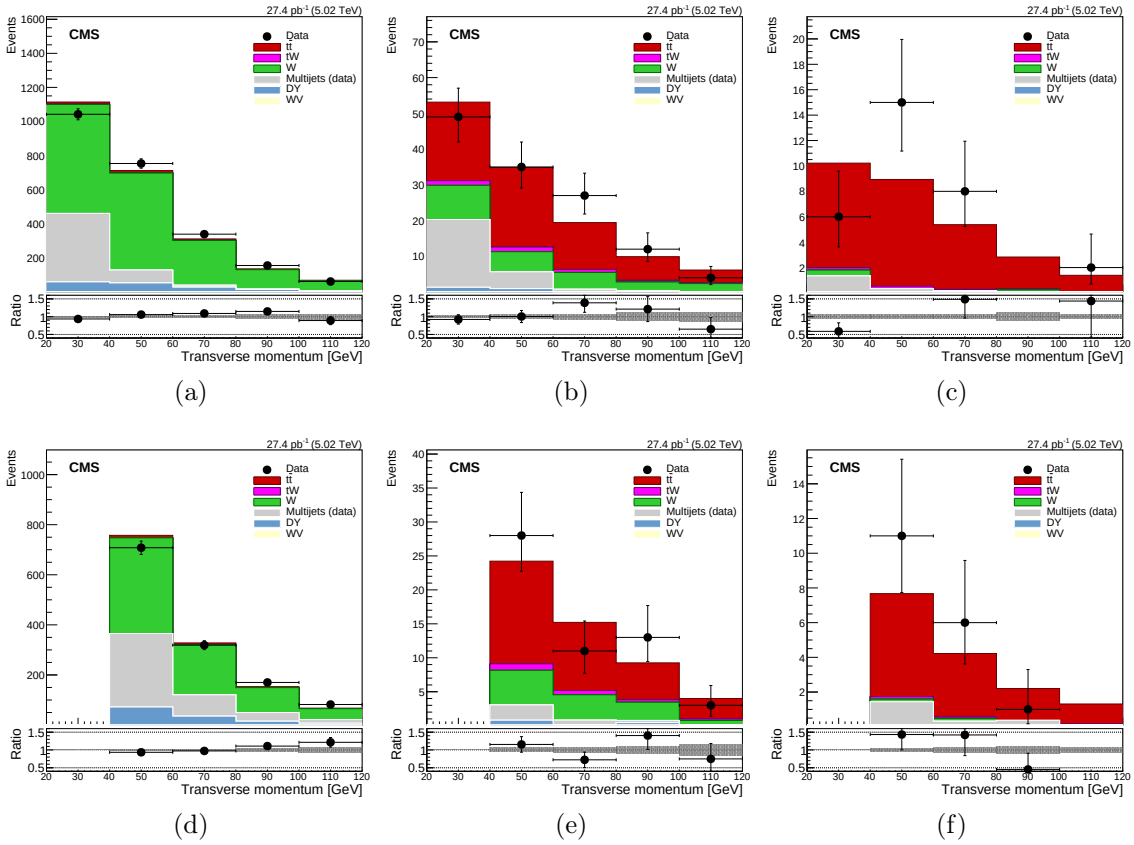

Figure 6.5: Distributions for the P_T in events with 0 (a/d), 1 (b/e) or at least 2 (c/f) b-tagged jets. The top (bottom) plots correspond to the muon (electron) channel.

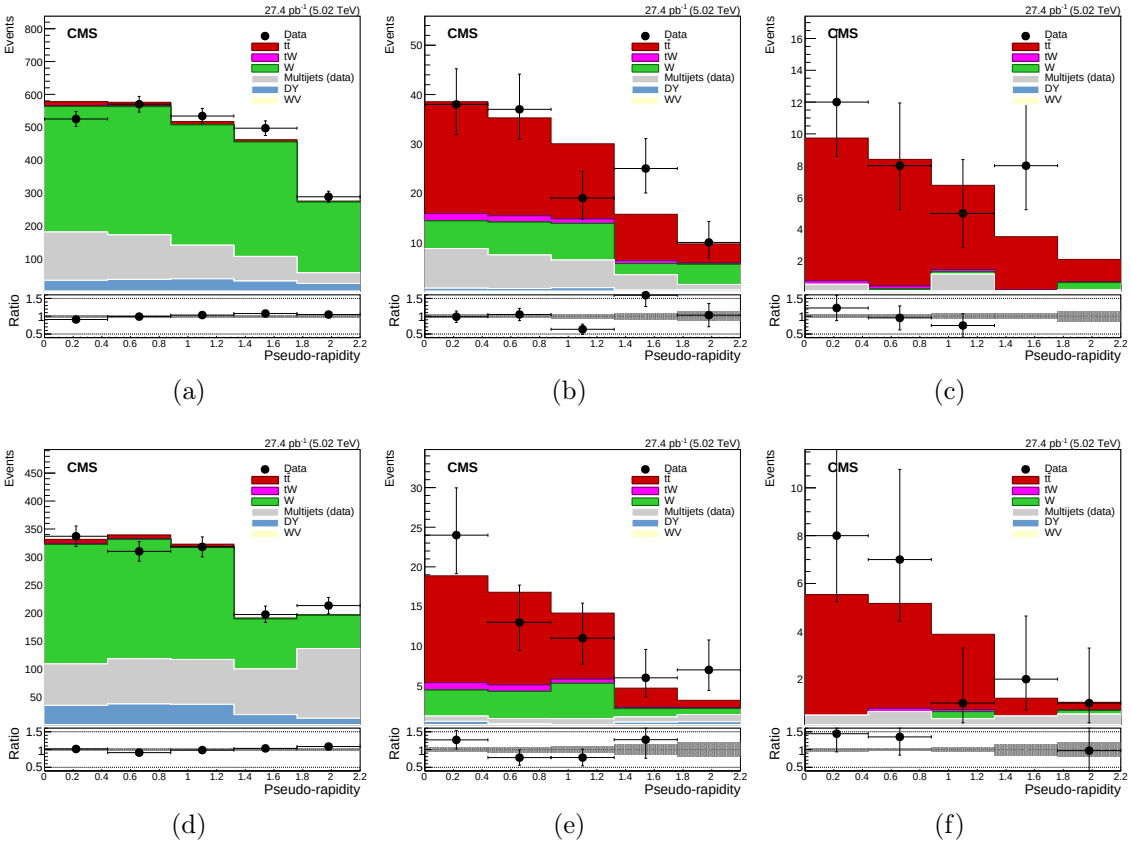

Figure 6.6: Similar as Fig. 6.5 for the pseudorapidity of the lepton.

The leading jet (or $b-tagged$ jet in events with b$-tags$) P$_T$ *and* η distributions are shown in Fig. 6.7 and 6.8. The scalar sum P_T of the selected jets (H_T) in the event is shown in Fig. 6.9. A slight trend of the jet P_T is observed in events without b-tags (dominated by W+jets).

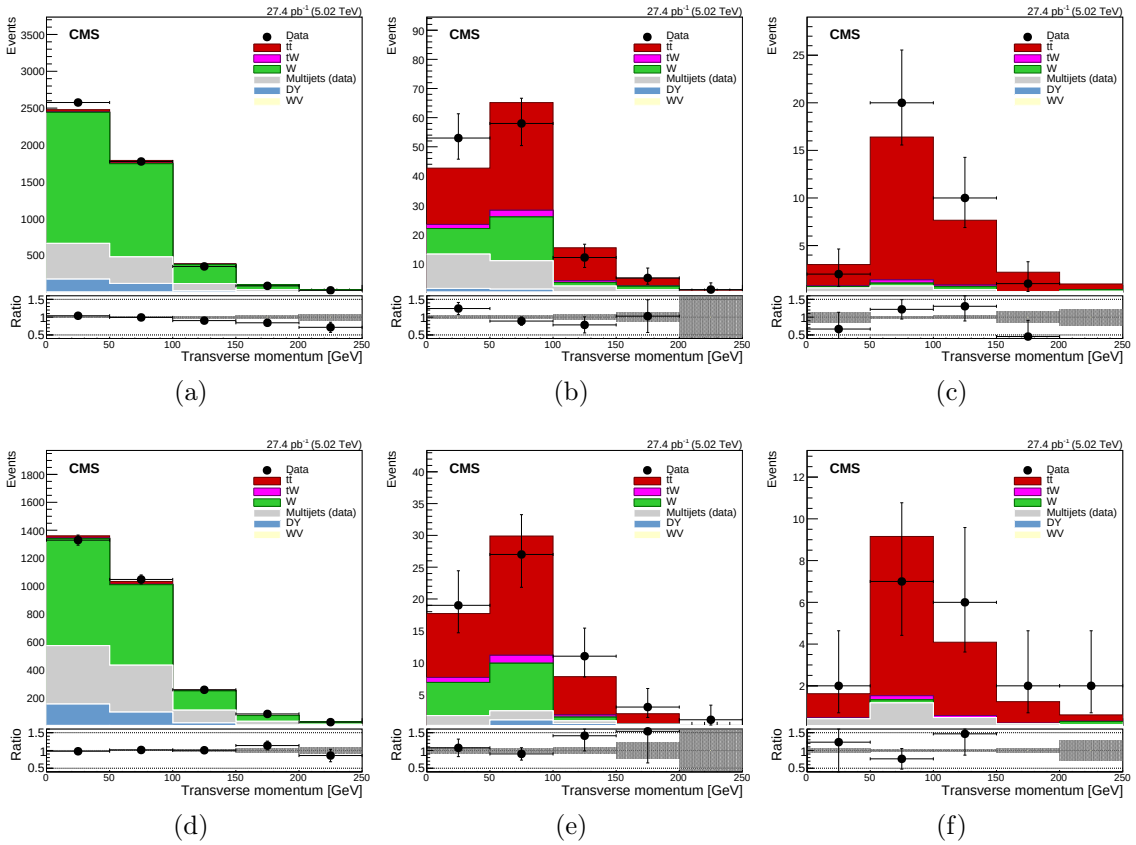

Figure 6.7: Similar as Fig. 6.5 for the two leading jets P_T in case there is no b-tagged jet, or for the leading b-tagged jet P_T.

Fig. 6.10 shows the distribution of M(ℓ,b), the invariant mass of the lepton and the b-tagged jet. For events without b-tags we compute the invariant mass with respect to the leading P_T jet. Good agreement is found between data and simulations in both channels.

For each selected event, the $W \to qq'$ dijet candidate is selected as described in

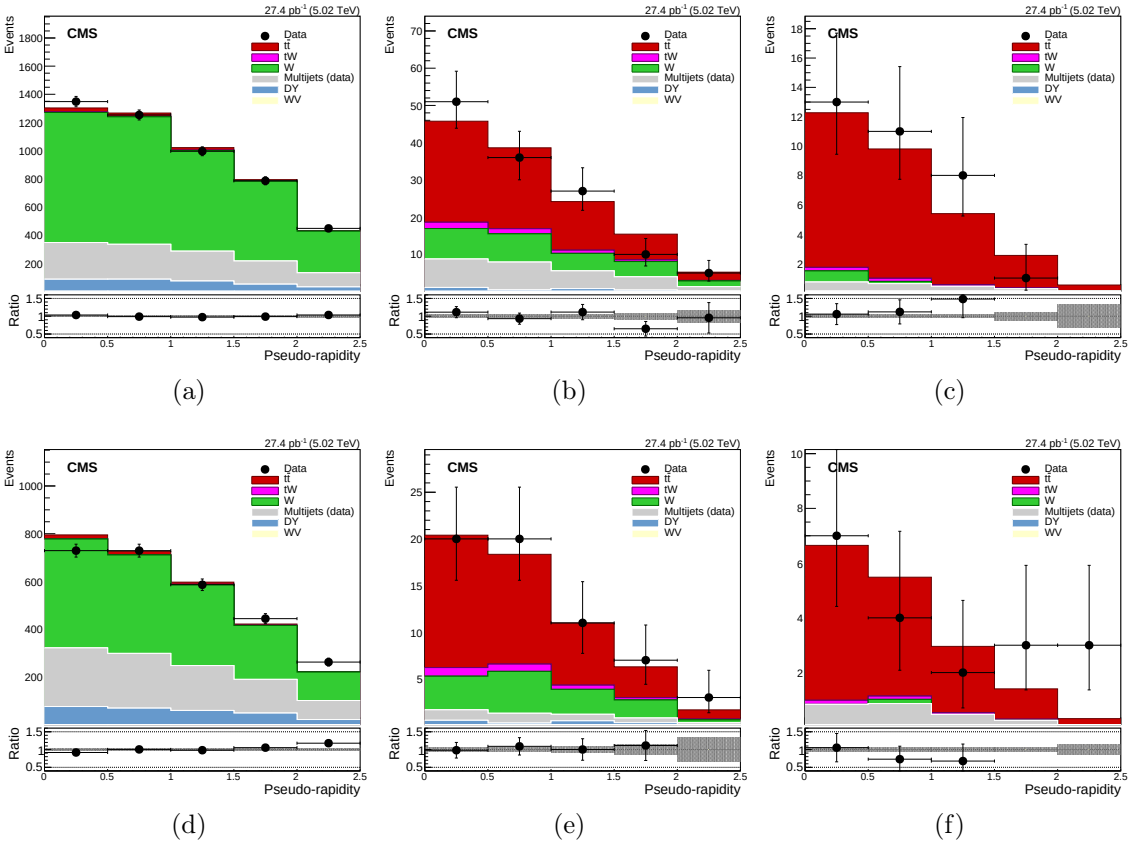

Figure 6.8: Similar as Fig. 6.7 for the pseudo-rapidity of the jet(s).

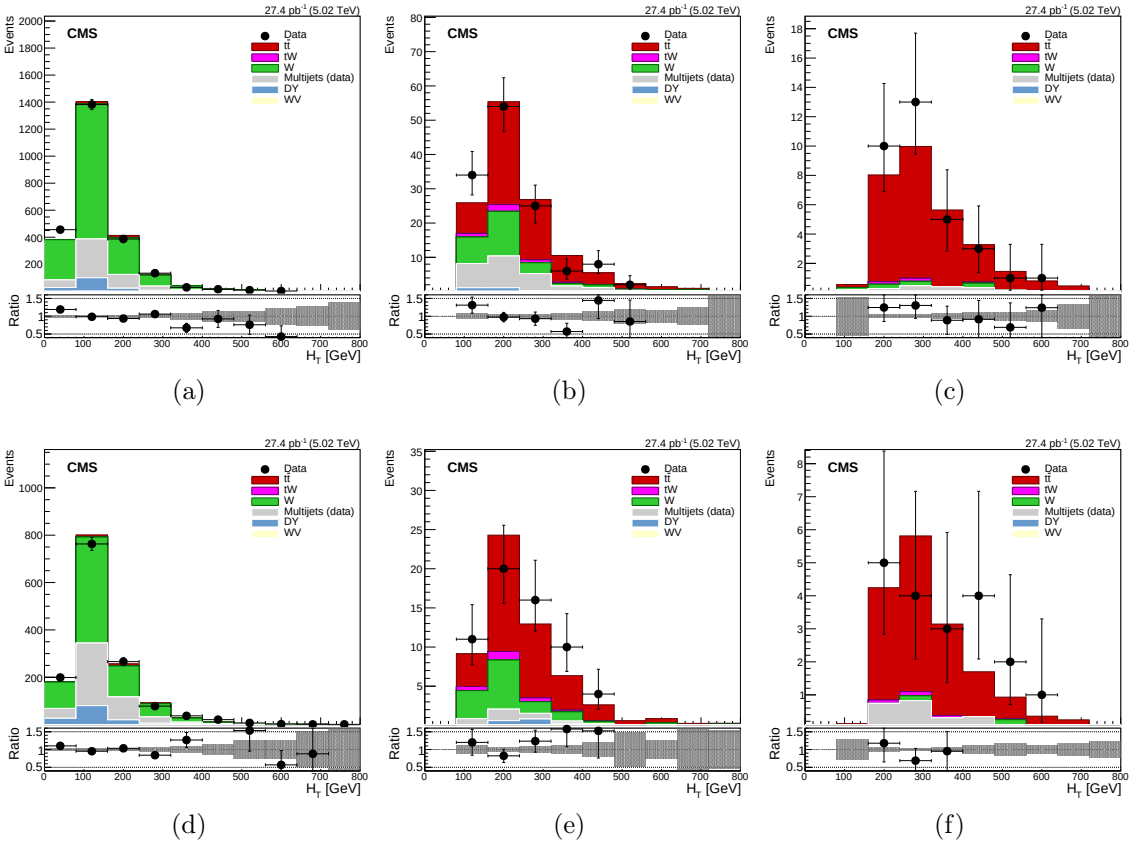

Figure 6.9: Similar as Fig. 6.5 for the H_T variable.

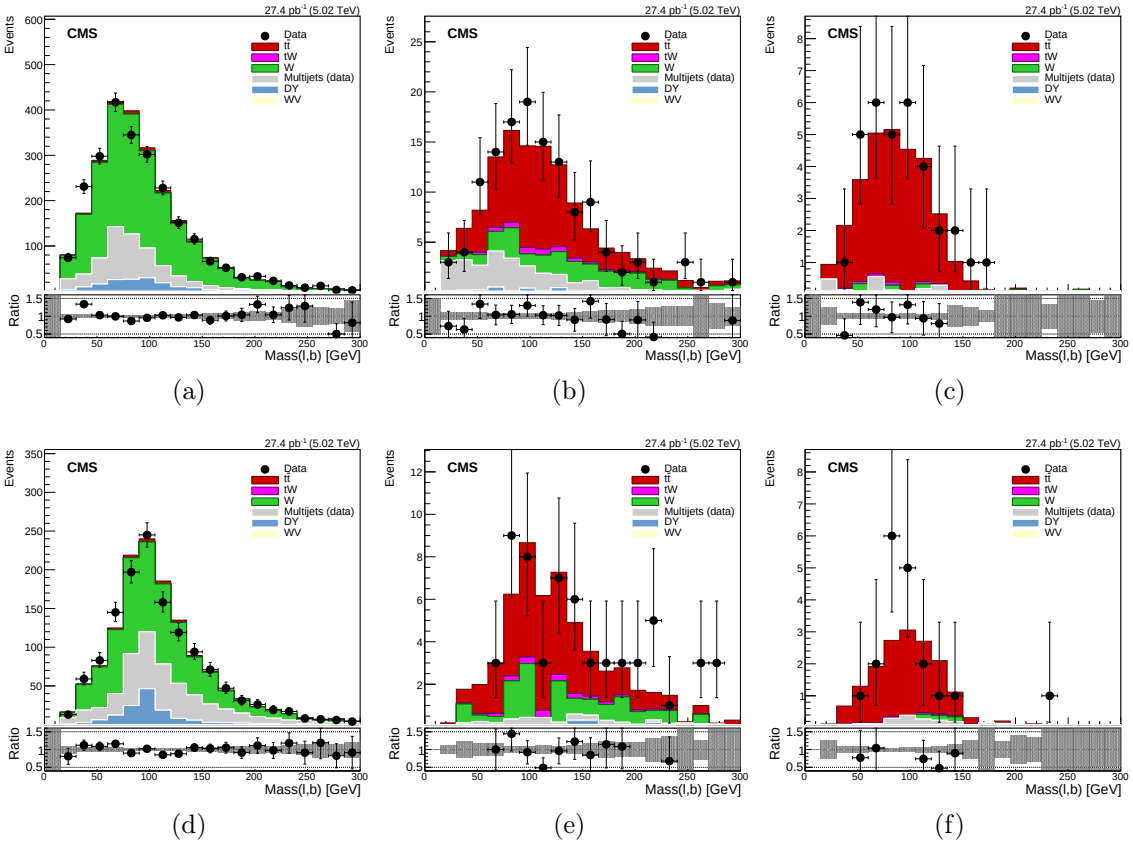

(a) (b) (c)

(d) (e) (f)

Figure 6.10: Similar as Fig. 6.5 for the $M(\ell, b)$ variable.

Sec. 6.3.1. Figs. 6.11, 6.12 and 6.13 show the dijet invariant mass distribution of the dijets selected by leading jet P_T, smallest ΔR and smallest ΔR where $\Delta R < 2.0$ correspondingly. Fair agreement is observed overall. The inital normalization of QCD tends to overestimate the observed data in the $0b$-tag category but this is expected to be corrected post-fit. In the signal region one can observe a significant improvement in the resolution of the dijet mass peak. The ranking in ΔR also removes some candidates at high mass, in particular in the μ+jets channel.

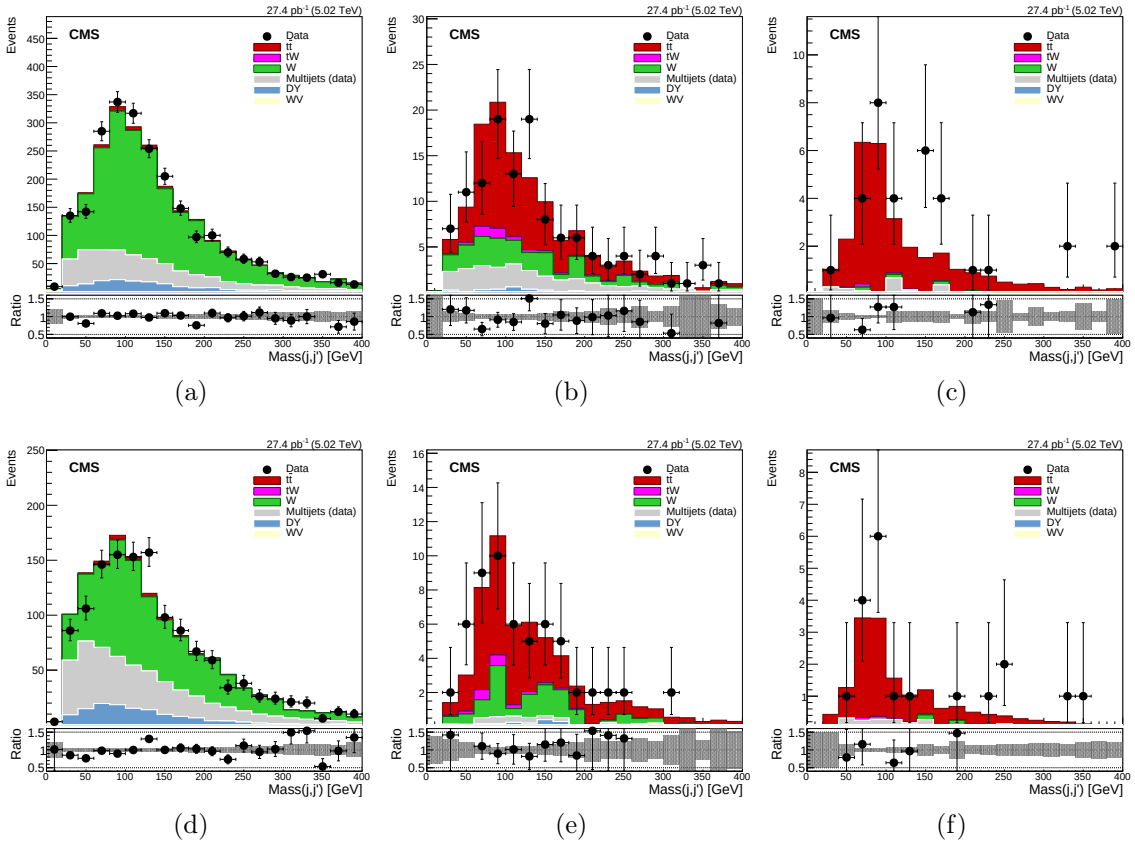

Figure 6.11: Similar as Fig. 6.5 for the $M(j, j')$ variable constructed from the two leading P_T jets in each event.

The $\Delta R(j, j')$ distribution for the jets closest in phase space is shown in Fig. 6.14.

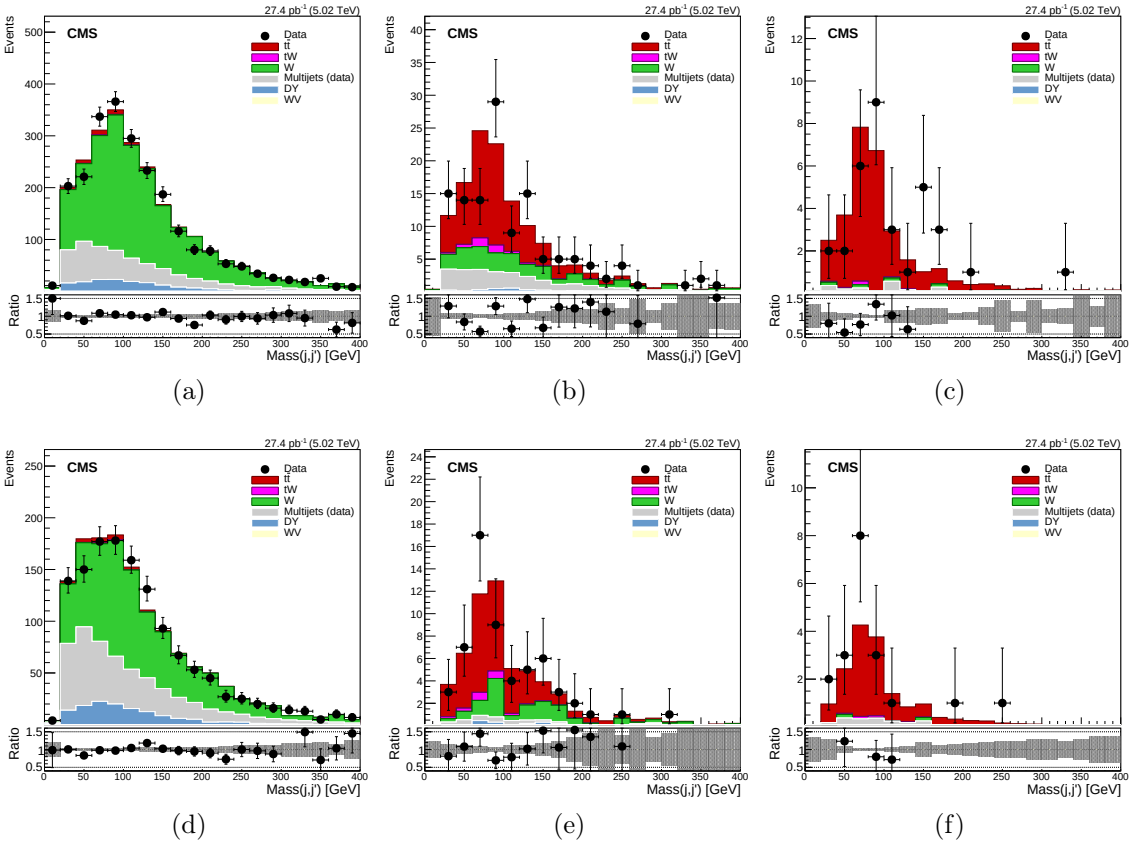

Figure 6.12: Similar as Fig. 6.11, when the jets closer in ΔR are used.

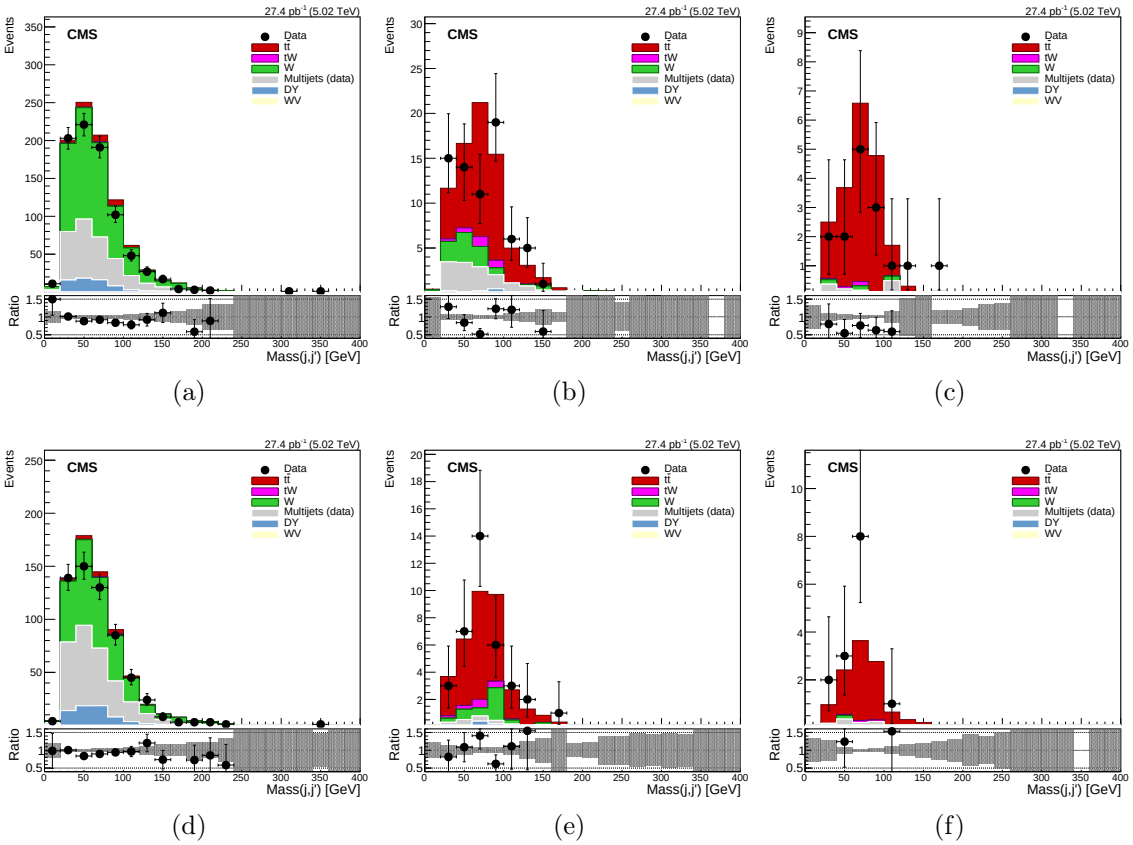

Figure 6.13: Similar as Fig. 6.11, when the jets closer in ΔR are used and $\Delta R < 2.0$ is imposed.

Fair agreement is observed overall. A clear separation between $t\bar{t}$, and the backgrounds QCD and W+jets is observed, making a clear distinction of a resonant dijet production in signal events. In addition we have computed the P_T and the η of the dijet system (Wboson candidate) in a pure region where $\Delta R < 2.0$ is imposed. The distributions are shown in Figs. 6.15 and 6.16, where the data is generally well reproduced by the pre-fit expectations.

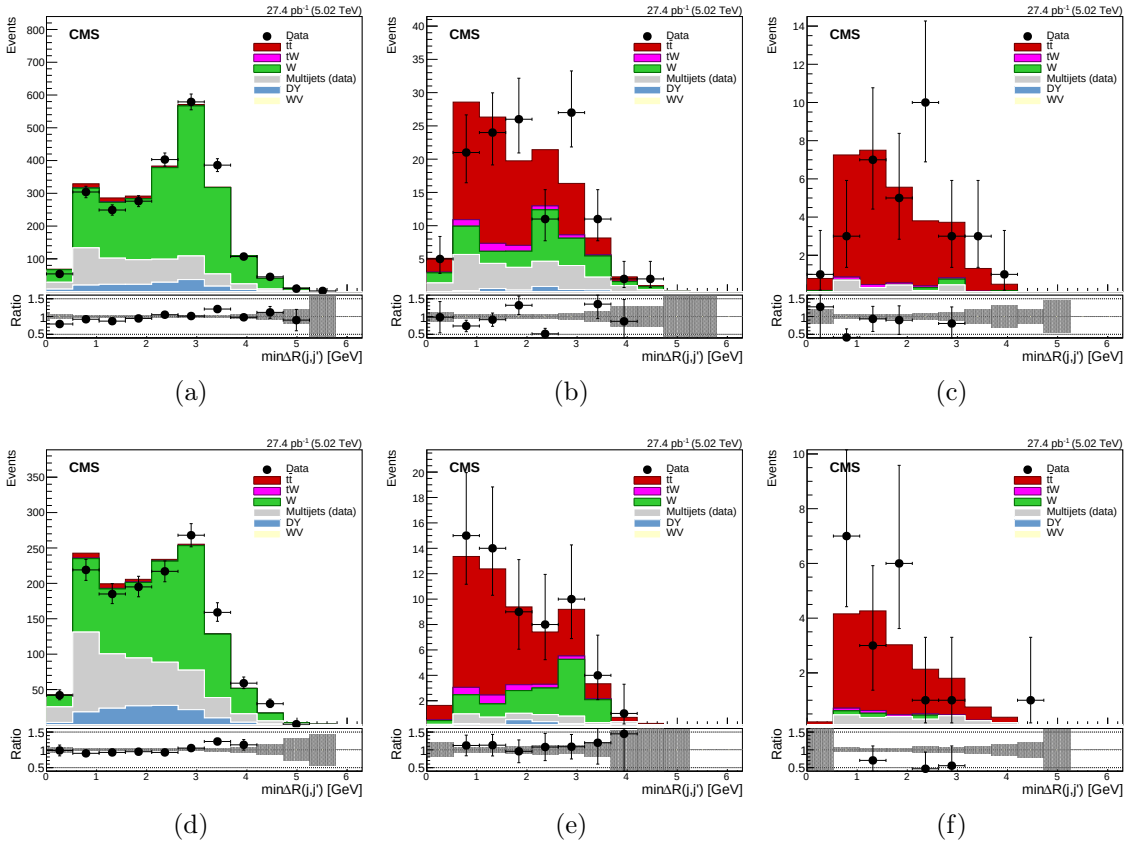

Figure 6.14: Similar as Fig. 6.5 for the $\Delta R(j, j')$ variable constructed from the two jets closest in ΔR in each event.

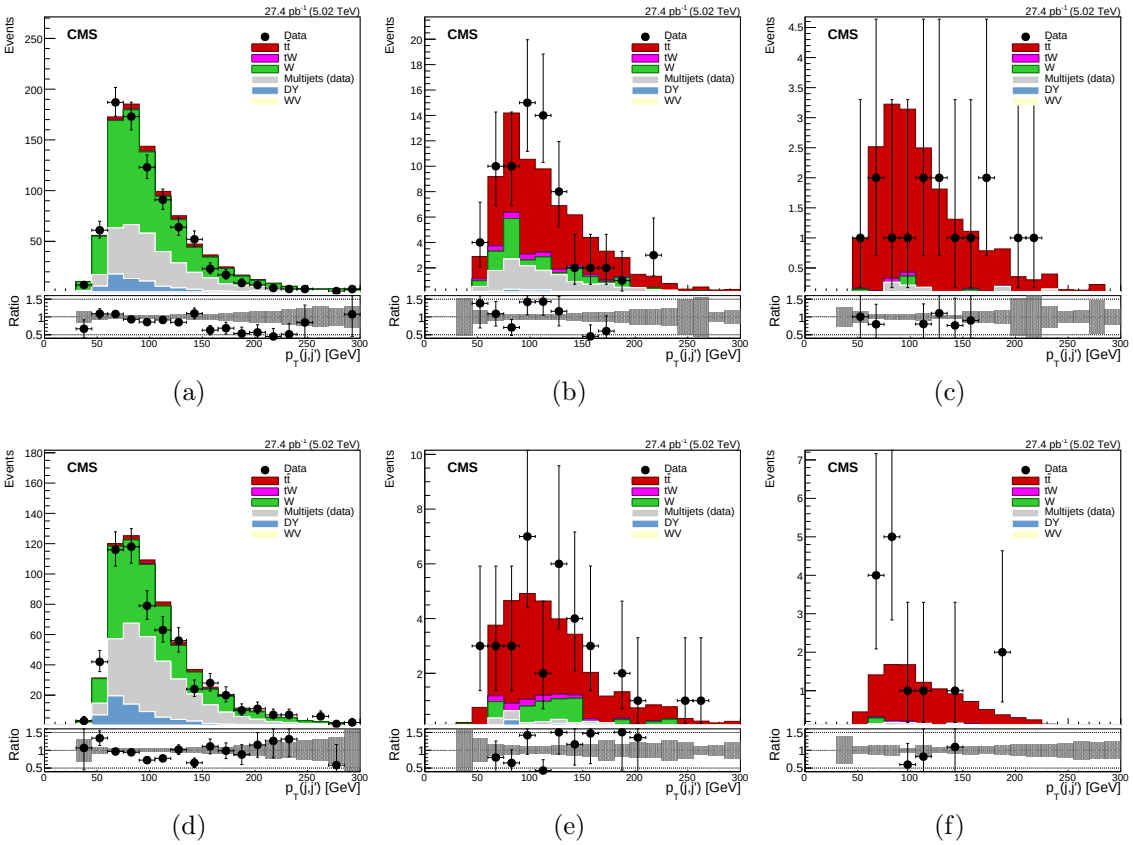

Figure 6.15: Similar as Fig. 6.14 showing the P_T of the dijet system, after imposing $\Delta R < 2.0$.

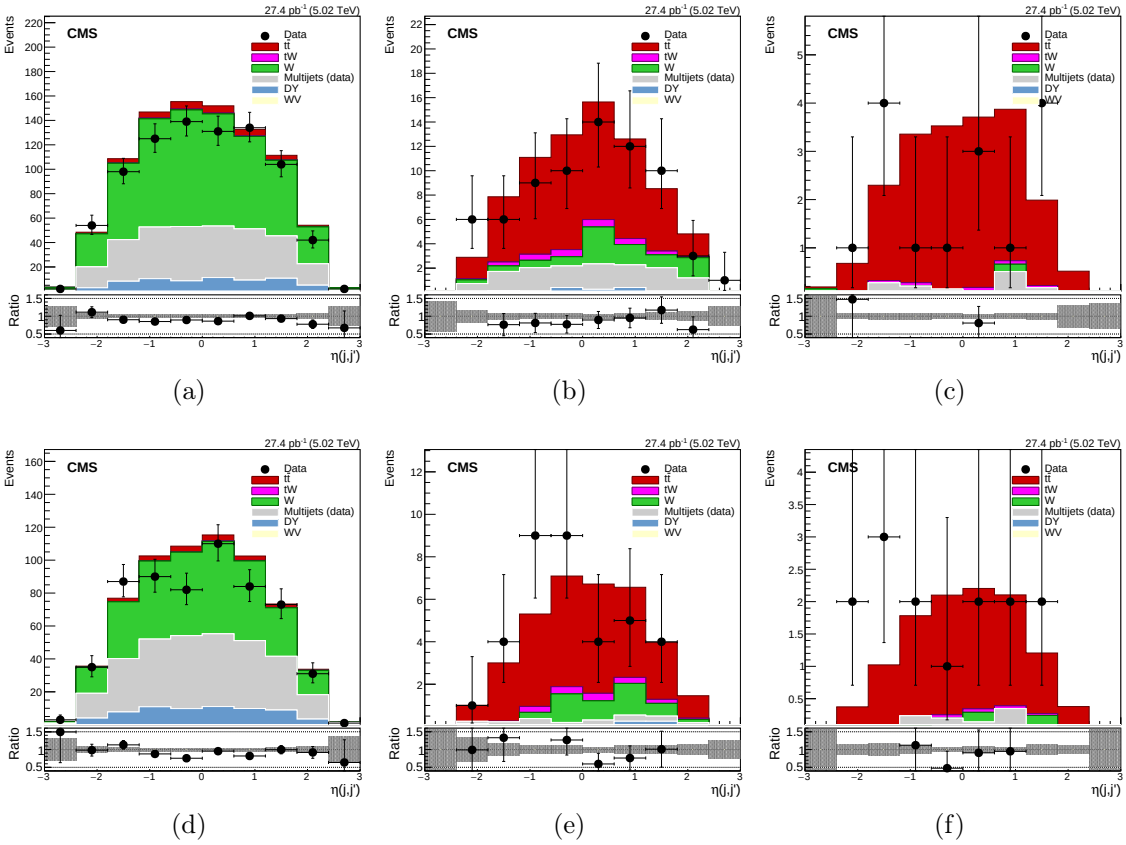

Figure 6.16: Similar as Fig. 6.15 showing the η of the dijet system

Chapter 7

$t\bar{t}$ Cross Section Extraction

In this chapter the systematic uncertainties, extraction of cross section for both the channels, combined cross section results and QCD analysis to illustrate the impact of the measured cross section, are presented.

7.1 Systematic uncertainties

The integrated luminosity has been estimated offline using a pixel cluster counting method [72]. The estimation takes into account normalization uncertainties and uncertainties related to the different conditions during typical physics periods relative to the specially tailored beam-separation scans, adding up to a total uncertainty of $\pm 2.3\%$.

The uncertainties in the electron trigger efficiency (1.5%) and the identification and isolation efficiency (2.5%) are estimated by changing the values of the data/simulation scaling factors within their uncertainties, obtained from the "tag-and-probe" method. The uncertainty in the muon identification and isolation efficiency, including the trigger efficiency, is 3% and covers one standard deviation of the scale factors from unity.

The impact of the uncertainty in the jet energy scale (JES) is computed by changing the P_T- and η-dependent JES corrections by a constant 2.8% [93]. The uncertainty

in jet energy resolution (JER) is computed via η-dependent variations in the JER corrections to the simulation [93]. The uncertainty arising from the use of P_T^{miss}in the $(\mu^{\pm}\mu^{\mp})$ channel is dominated by the unclustered energy contribution to P_T^{miss}. Finally, a 30% uncertainty is conservatively assigned to the jet misidentification probability in the ℓ+jets analysis, as no dedicated measurement of this quantity has been performed for the considered data set. Fig. 7.1 illustrates the impact of varying the main experimental uncertainties on the signal prediction, according to the prescriptions described above. Here b-tagging efficiency is chosen as a parameter of interest in the fitting.

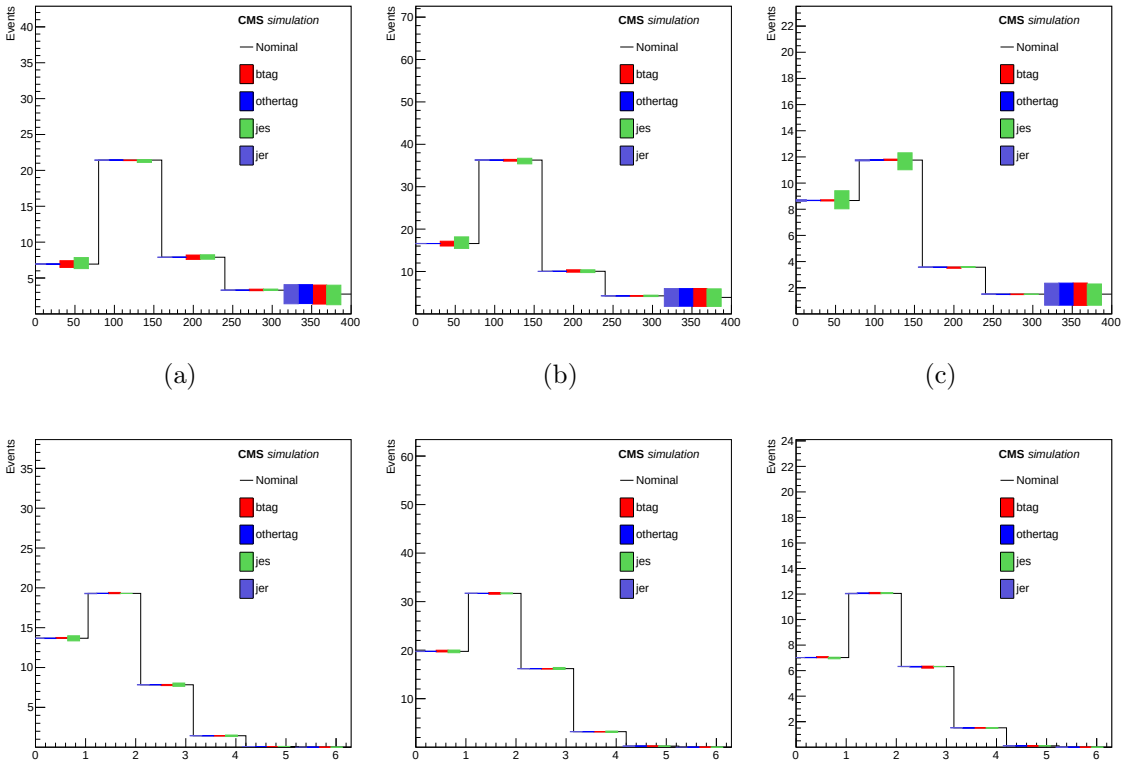

Figure 7.1: Illustration of signal shapes with the main experimental uncertainties super-imposed for t events with 0 (a/d), 1 (b/e) or at least 2 (c/f) b-tags. The top (bottom) plots correspond to the $M(j, j')$ ($\Delta R(j, j')$) distribution.

Theoretical uncertainties in the simulation of $t\bar{t}$ production cause a systematic bias corresponding the missing higher-order diagrams in $POWHEG$, which is computed by analyzing the signal modeling by modifying the $\mu_{\mathrm{R}}, \mu_{\mathrm{F}}$ scales within a factor of two w.r.t their nominal value. The impact of the $\mu_{\mathrm{R}}, \mu_{\mathrm{F}}$ variations are examined independently in ℓ+jets analysis, while in the dilepton analysis they are varied simultaneously. In both analyses, these variations are applied independently at level of matrix element (ME) and parton shower (PS).

The hadronization uncertainty is computed via a comparison of sample of events generated by using $POWHEG$, where hadronization is modelled with $PYTHIA$ or $HERWIG++$h (v2.7.1) [95]. This is what also accounts for differences in the PS model and the underlying event. The uncertainty from the choice of PDF is computed via reweighting the sample of simulated $t\bar{t}$ events in accordance with the root-mean-square (RMS) variation of the NNPDF3.0 replica set. Two extra variations of α_{s} are added in quadrature to determine the total PDF uncertainty.

In the ℓ+jets analysis, the uncertainty in the choice of the $\mu_{\mathrm{R}}, \mu_{\mathrm{F}}$ scales in the W+jets simulation is taken into account by considering alternative shapes and yields after varying independently the $\mu_{\mathrm{R}}, \mu_{\mathrm{F}}$ scales, following a similar procedure to that described above for the signal. Due to the finite event count in the W+jets simulated sample, an additional bin-by-bin uncertainty is assigned by generating an alternative shape to fit (see Section 7.2.1), where the bin prediction is varied by ± 1 standard deviation, while keeping all the other bins at their nominal expectation. The uncertainty assigned to the QCD multijet background includes the statistical uncertainty in the data, and the uncertainty from the non-QCD multijet contributions subtracted from the control region, as described in Section 6.3.1, and an additional 30%–100% normalization uncertainty. The latter depends on the event category and stems from the measured difference with respect to an alternative estimate of the QCD normalization based on the transverse mass, m_{T}, of the lepton and P_T^{miss} system. Finally,

a 30% normalization uncertainty in the theoretical tW, Z/γ^*, and WV background cross sections is assigned [9], given the previously unexplored $\sqrt{s}$ value and that the final states contain several jets.

In the dilepton channel, an uncertainty of 30% is considered [9] for the cross sections of the tW and WV backgrounds to cover the theoretical uncertainties and the effect of finite simulated sets. The uncertainty in the Z/γ^* estimation is calculated by combining in quadrature the statistical uncertainty and an additional 30% from the variation of the scale factor in the different levels of selection, resulting in uncertainties of about 30 and 80% in the $(e^{\pm}\mu^{\mp})$and $(\mu^{\pm}\mu^{\mp})$ channels, respectively. The systematic uncertainty in the non-W/Z background is estimated to be 90% in the $(e^{\pm}\mu^{\mp})$ channel and is dominated by the statistical uncertainty in the method. Owing to the limited sample size in the data, the method cannot be applied in the $(\mu^{\pm}\mu^{\mp})$ channel. The estimation is therefore based on MC simulation, and an uncertainty of 100% is conservatively assigned.

Fig. 7.2 summarizes the expected effect on the signal shapes from the choices of the QCD/PS-scales and hadronizer. For the QCD scale choices at matrix element level, the effect on the normalization is computed and assigned separately. Fig. 7.3 illustrates the effect of the QCD scale choice at matrix-element level for the W process. Here the impact on the normalization is large and included in the fit as it affects the nominal W+jets prediction.

7.2 Measurement of the $t\bar{t}$ cross section

7.2.1 The ℓ+jets final state

In the ℓ+jets analysis, the $t\bar{t}$ cross section is measured in a fiducial phase space by means of a fit. Two variables were independently considered for the fit, which are sensitive to the resonant behaviour of the light jets produced from the W boson

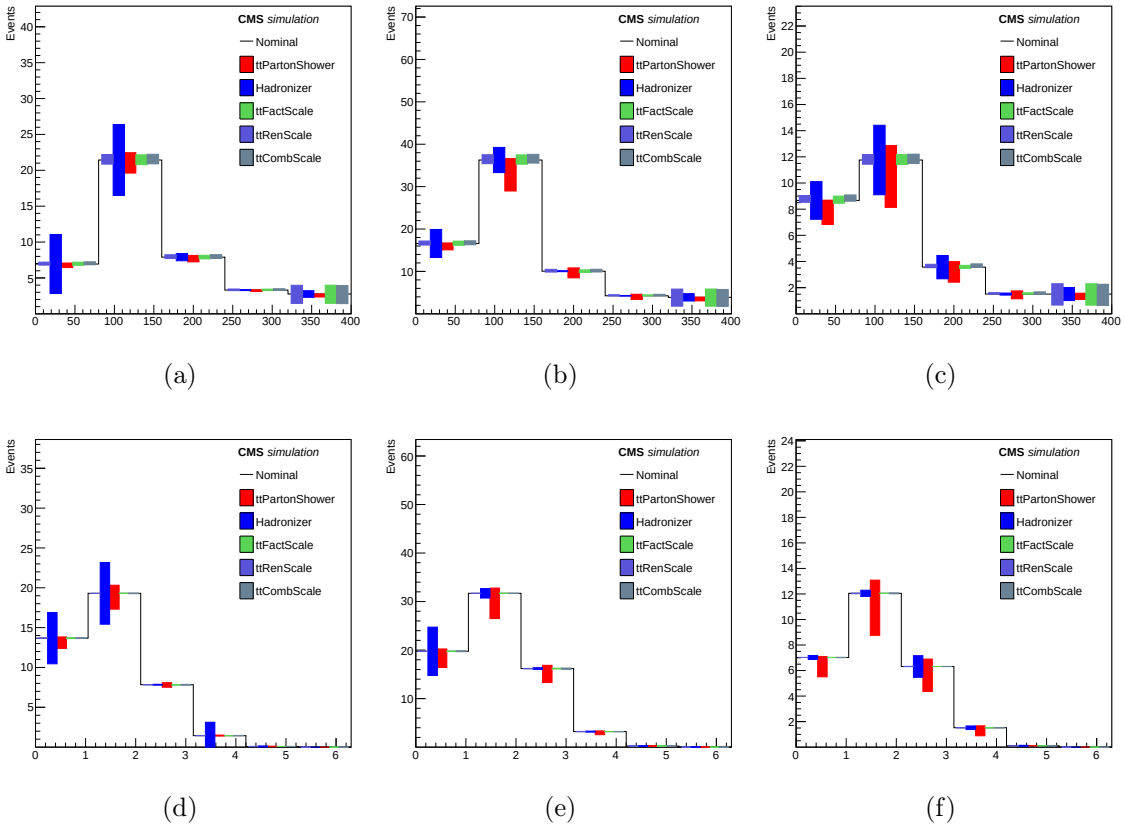

Figure 7.2: Illustration of signal shapes with the QCD/PS-scale, and hadronizer choice related uncertainties. See more details in Fig. 7.1 for the correspondences to the event categories.

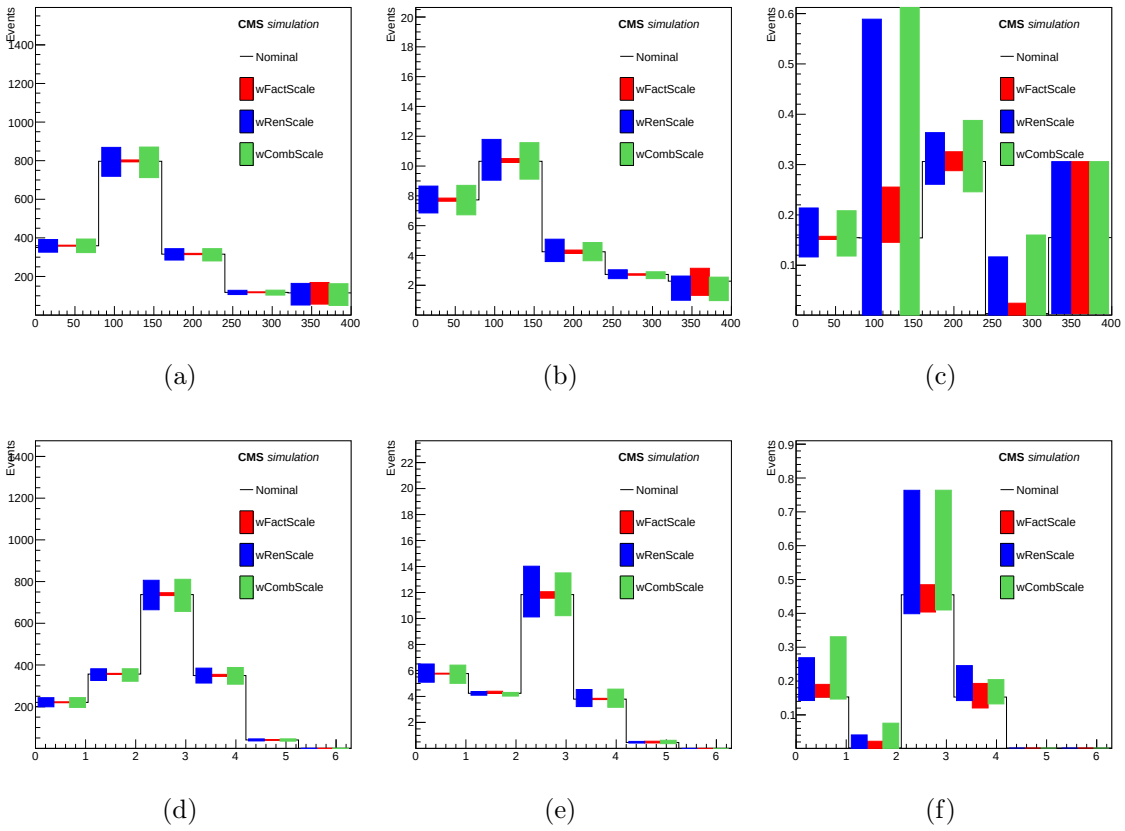

Figure 7.3: Illustration of W+jets shapes with the QCD-scale choice related uncertainties. See more details in Fig. 7.1 for the correspondences to the event categories.

hadronic decay in a $t\bar{t}$ event. Given that these light jets, here denoted by j and j', are correlated during production, they are also expected to be closer in phase space when compared to pairs of other jets in the event. The angular distance ΔR can thus be used as a metric to rank all pairs of non-b-tagged jets, maximizing the probability of selecting those from the W decay in cases where additional non-b-tagged jets are found. From simulation we expect that the signal peaks at low ΔR, while the background is uniformly distributed up to $\Delta R \approx 3$. Above that value, fewer events are expected and background processes are predicted to dominate. The invariant mass $M(j, j')$ of jets j and j' also has a distinctive peaking feature for the signal in contrast with a smooth background continuum. From simulation we expect that the minimum angular distance ΔR between all pairs of jets j and j', $\Delta R_{\text{min}}(j, j')$, is robust against signal modeling uncertainties such as the choice of the $\mu_{\text{R}}, \mu_{\text{F}}$ scales and jet energy scale and resolution, while the $M(j, j')$ variable tends to be more affected by such uncertainties. Owing to its more robust systematic uncertainties and signal-to-background discrimination power, the $\Delta R_{\text{min}}(j, j')$ variable is used to extract the $t\bar{t}$ cross section.

The $\Delta R_{\text{min}}(j, j')$ distributions are categorized $w.r.t$ to additional number of jets other than those which coming from W boson hadronic decay–passing the b quark identification criteria, to maximize the sensitivity of the analysis. In total, 6 categories are used, corresponding to electron or muon events with 0, 1, or $\geq$2 b jets. Table 7.1 summarises the observed yields and expected number of signal and background events in all categories prior to the fit. Fair agreement is observed between data and expectations.

The $M(j, j')$ and $\Delta R_{\text{min}}(j, j')$ distributions are shown in Fig. 7.4. The distributions have been combined for the e+jets and μ+jets channels to maximize the statistical precision and are shown for events with different b-tagged jet multiplicities. Fair agreement is observed between data and the pre-fit expectations.

Table 7.1: The number of expected background and signal events and the observed event yields in the different b tag categories for the e+jets and μ+jets analyses, prior to the fit. With the exception of the QCD multijet estimate, for which the total uncertainty is reported, the uncertainties reflect the statistical uncertainty in the simulated samples.

Process	Category =0b		=1b		≥2b	
	e	μ	e	μ	e	μ
$t\bar{t}$	22.8±0.3	42.3±0.4	36.9±0.4	71.1±0.5	13.8±0.2	27.0±0.3
tW	3.03±0.02	5.6±0.03	2.49±0.02	4.5±0.03	0.39±0.01	0.67±0.01
QCD multijets	442±132	493±148	3.6±1.1	28±8	2.5±0.8	2.0±0.8
W+jets	776±17	1704±26	13±2	26±3	0.2±0.3	0.8±0.6
DY	136±4	162±5	1.7±0.5	2.8±0.6	0.1±0.1	0.1±0.1
VV	0.52±0.01	1.01±0.02	<0.01	< 0.02	< 0.01	< 0.01
Total	1381±133	2408±150	57.7±2.4	131±9	16.8±0.9	31±1
Observed	1375	2406	61	129	19	33

A profile likelihood ratio method (PLR), same as employed in Ref. [12], is used to perform the fit. In addition, we consider the b-tagging efficiency scale factor (SF_b) as a parameter of interest for the fit. The PLR is written as:

$$\lambda(\mu, \mathrm{SF}_b) = \frac{\mathcal{L}(\mu, \mathrm{SF}_b, \hat{\hat{\Theta}})}{\mathcal{L}(\hat{\mu}, \hat{\mathrm{SF}}_b, \hat{\Theta})}, \tag{7.2.1}$$

where $\mu = \sigma/\sigma_{\mathrm{theo}}$ is the signal strength (ratio of the observed $t\bar{t}$ cross section to the theoretical cross section) and Θ denotes the nuisance parameters which encode the effect on the expectations due to variations in the sources of the systematic uncertainties described in Section 7.1. The quantities $\hat{\hat{\Theta}}$ correspond to the values of the nuisance parameters that maximize the likelihood for the specified signal strength and b tagging efficiency (conditional likelihood), and $\hat{\mu}$, $\hat{\mathrm{SF}}_b$, $\hat{\Theta}$ are, respectively, the values of the signal strength, b tagging efficiency, and nuisance parameters that maximize the likelihood.

Fig. 7.5 (left) shows the two-dimensional contours at the 68% confidence level (CL) obtained from the scan of $-2\ln(\lambda)$, as functions of μ and SF_b. The expected

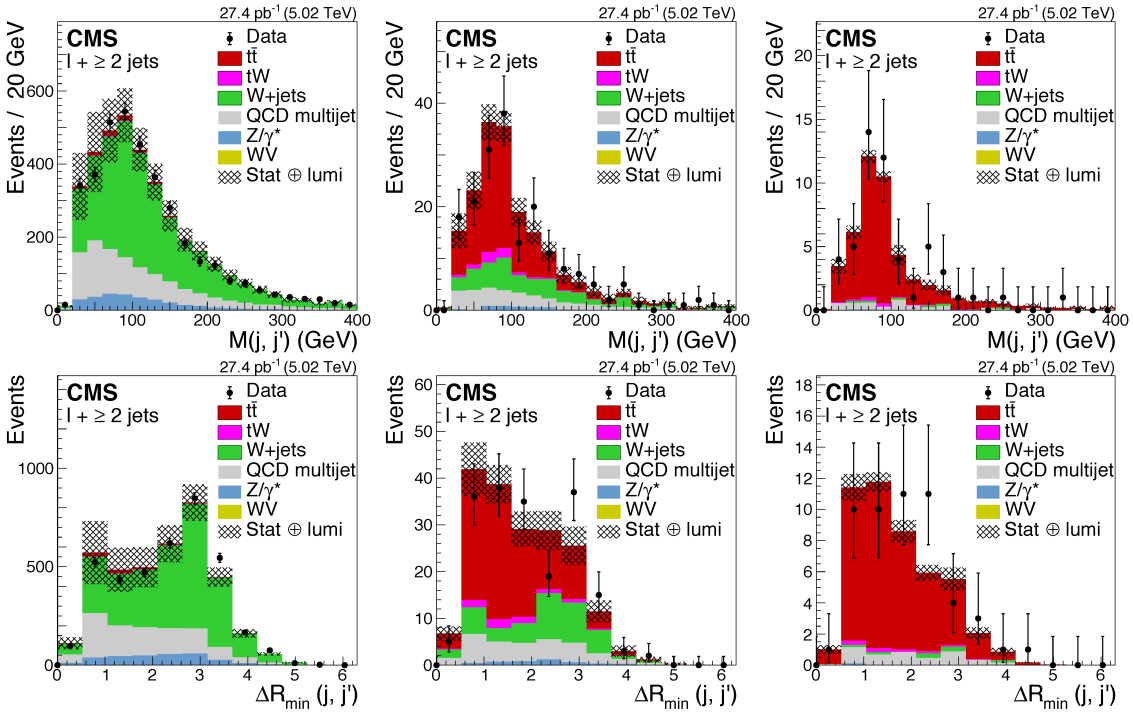

Figure 7.4: The predicted and observed distributions of the (upper row) $M(j, j')$ and (lower row) $\Delta R_{\text{min}}(j, j')$variable for ℓ+jets events in the 0 b (left), 1 b (center), and $\geq$2 b (right) tagged jet categories. The distributions from data are compared to the sum of the expectations for the signal and backgrounds prior to any fit. The QCD multijet backgrounds are determined from data. The cross-hatched band represents the statistical and the integrated luminosity uncertainties in the expected signal and background yields added in quadrature. The bars on the black data points show the statistical uncertainties.

results, obtained using the Asimov data set [96], are compared to the observed results and found to be in agreement well within one standard deviation. The signal strength is obtained after profiling SF_b and the result is $\mu = 1.00\ ^{+0.10}_{-0.09}(stat)\ ^{+0.09}_{-0.08}(sys)$. Further details of the fit results are given in AppedixB. As a cross-check, the signal strength is also extracted by fitting only the total number of events observed in all six categories. The observed value $\mu = 1.03\ ^{+0.10}_{-0.10}(stat)\ ^{+0.21}_{-0.11}(sys)$ is in agreement with the analysis using the $\Delta R_{\text{min}}(j, j')$distributions. Fig. 7.5 (right) summarizes the results obtained

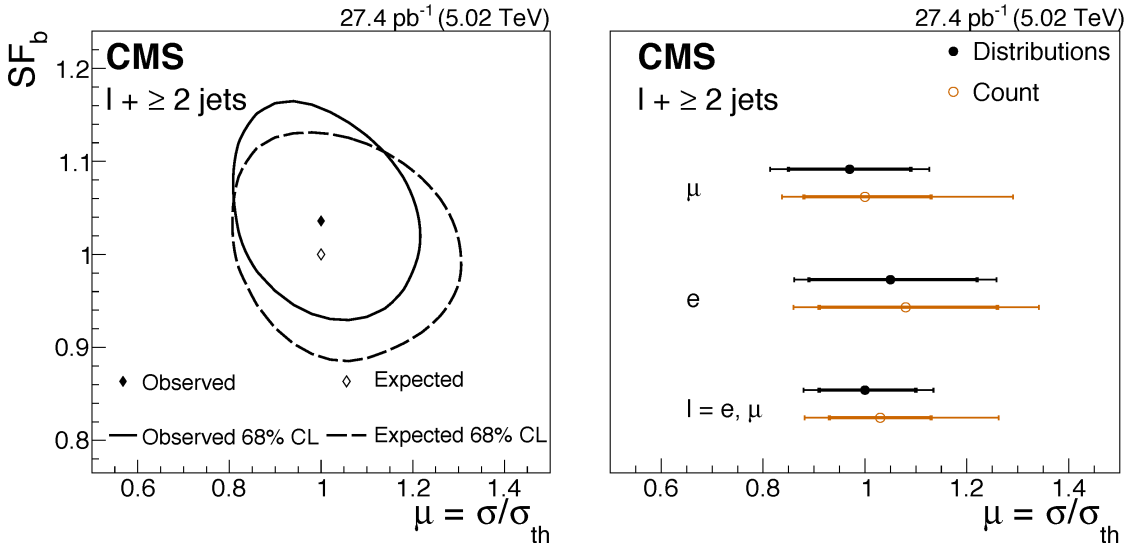

Figure 7.5: Left: The 68% CL contour obtained from the scan of the likelihood in ℓ+jets analysis, as a function of μ and SF_b in the ℓ+jets analysis. The solid (dashed) contour refers to the result from data (expectation from simulation). The solid (hollow) diamond represents the observed fit result (SM expectation). Right: Summary of the signal strengths separately obtained in the e+jets and μ+jets channels, and after their combination in the ℓ+jets channel. The results of the analysis from the distributions are compared to those from the cross-check analysis with event counting (Count). The inner (outer) bars correspond to the statistical (total) uncertainty in the signal strengths.

for the signal strength fit in each channel separately from the analysis of the distributions and from event counting. In both cases, a large contribution to the uncertainty is systematic in nature, although the statistical component is still significant. In the ℓ+jets combination, the μ+jets channel is expected and observed to carry the largest weight.

To determine the impact of the experimental systematic uncertainties in the measured signal strength, fit is repeated after fixing one nuisance parameter at a time at its post-fit uncertainty (± 1 standard deviation) values. The impact on the signal strength fit is then evaluated from the difference induced in the final result from this procedure. By redoing the fits, the impact of few nuisance parameters being fixed

Table 7.2: Estimated impact of all sources of uncertainty in the value of μ extracted from the analysis of distributions, and in the cross-check from event counting. The "Other background" component includes the contributions from Z/γ^*, tW, and WV events. The total uncertainty is computed by adding in quadrature the statistical, experimental, systematic, and theoretical uncertainties. The individual experimental uncertainties are obtained by repeating the fit after fixing one nuisance parameter at a time at its post-fit uncertainty (± 1 standard deviation) value. The values quoted have been symmetrized.

Uncertainty	$\Delta\mu/\mu$	
	Cut-in-Categories	Shape
Statistics	0.010	0.095
Systematics	0.160	0.085
Experimental uncertainties		
W+jets	0.025	0.035
QCD multijets	0.044	0.024
Other backgrounds	0.013	0.013
Jet energy scale	0.031	0.030
Jet energy resolution	0.023	0.006
b-tagging	0.045	0.034
Electron efficiencies	0.028	0.011
Muon efficiencies	0.022	0.017
Theory uncertainties		
Hadronizer	0.069	0.028
Parton shower scale	0.115	0.044
$t\bar{t}$QCD scale	<0.01	<0.01
Total	0.189	0.127

might get reabsorbed by a variation of the ones being profiled, owing to correlations. As such, the individual experimental uncertainties obtained and summarized in Table 7.2 can only be interpreted as the observed post-fit values, and not as an absolute, orthogonalized breakdown of uncertainties. With respect to the event counting, the analysis of the distributions is less prone to the uncertainties in the QCD multijet background, jet energy resolution, and signal modeling. In both cases, the signal modeling uncertainties and the b tagging efficiency are among the largest sources of uncertainty.

The fiducial cross section is measured in events with one electron (muon) in the range P_T> 35 (25) GeV and $|\eta| < 2.1$ (including the transition region for electrons), and at least two jets with $P_T > 25\,GeV$ and $|\eta| < 2.4$. After multiplying the signal strength by the theoretical expectations (Eq. (6.2.1)), we find

$$\sigma_{\text{fid}} = 20.8 \pm 2.0\ (stat) \pm 1.8\ (syst) \pm 0.5\ (lumi)\ pb.$$

The combined acceptance in the e+jets and μ+jets channels is estimated using the NLO *POWHEG* simulation to be $\mathcal{A} = 0.301 \pm 0.007$, with the uncertainty being dominated by the variation of the $\mu_{\text{R}}, \mu_{\text{F}}$ scales at ME and PS levels and the hadronization model used for the $t\bar{t}$ signal. The uncertainty due to the PDFs is included but verified to be less important. Taking into account the acceptance of the analysis and its uncertainty, the inclusive $t\bar{t}$ cross section is determined to be

$$\sigma_{t\bar{t}} = 68.9 \pm 6.5\ (stat) \pm 6.1\ (syst) \pm 1.6\ (lumi)\ pb,$$

which in a fair agreement with the SM prediction and attaining a 13% total relative uncertainty.

7.2.2 The dilepton final state

In the dilepton analysis, the $t\bar{t}$ cross section is extracted from an event counting measurement. Fig. 7.6 shows the distributions of the jet multiplicity and the scalar P_T sum of all jets (H_{T}), for events passing the dilepton criteria in the ($e^{\pm}\mu^{\mp}$) channel. In addition, it displays the lepton-pair invariant mass and P_T distributions, after requiring at least two jets in the event in the ($e^{\pm}\mu^{\mp}$) channel. Fig. 7.7 shows the P_T^{miss} and the lepton-pair invariant mass distributions in the ($\mu^{\pm}\mu^{\mp}$) channel for events passing the dilepton criteria, and the Z boson veto with the P_T^{miss}> 35 GeV requirement, in the second case. The predicted distributions take into account the

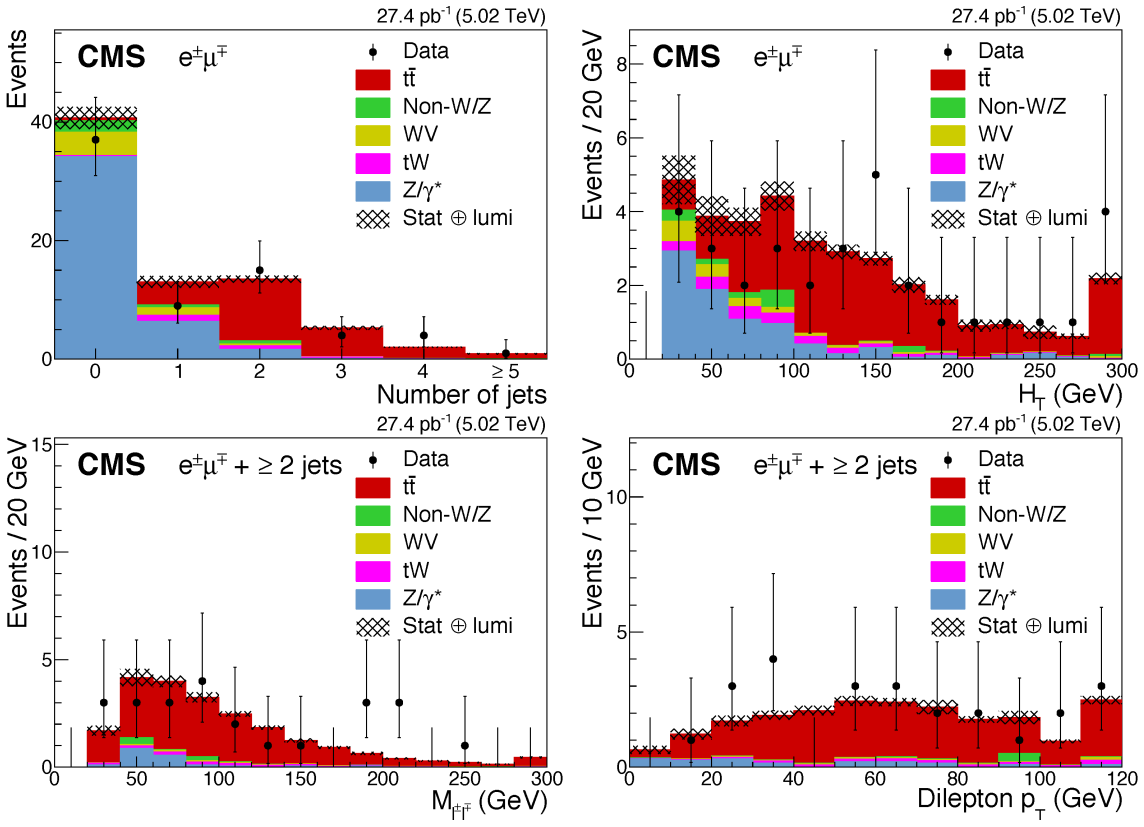

Figure 7.6: Predicted and observed distributions of the (upper row) jet multiplicity and scalar P_T sum of all jets (H_{T}) for events passing the dilepton criteria, and of the (lower row) invariant mass and P_T of the lepton pair after requiring at least two jets, in the ($e^{\pm}\mu^{\mp}$) channel. The Z/γ^* and $Non-WZ$ backgrounds are determined from data (see Section 6.3.2). The cross-hatched band represents the statistical and integrated luminosity uncertainties in the expected signal and background yields added in quadrature. The bars on the data points show the statistical uncertainties. The last bin of the distributions contains the overflow events.

efficiency corrections described in Section 6.3 and the background estimations discussed in Section 6.3.2. Good agreement is found between the data and predictions for both signal and background.

The fiducial $t\bar{t}$ production cross section is computed by counting events in the visible phase space (defined by the same P_T, $|\eta|$, and multiplicity requirements for leptons and jets, but including the transition region for electrons) and is denoted by

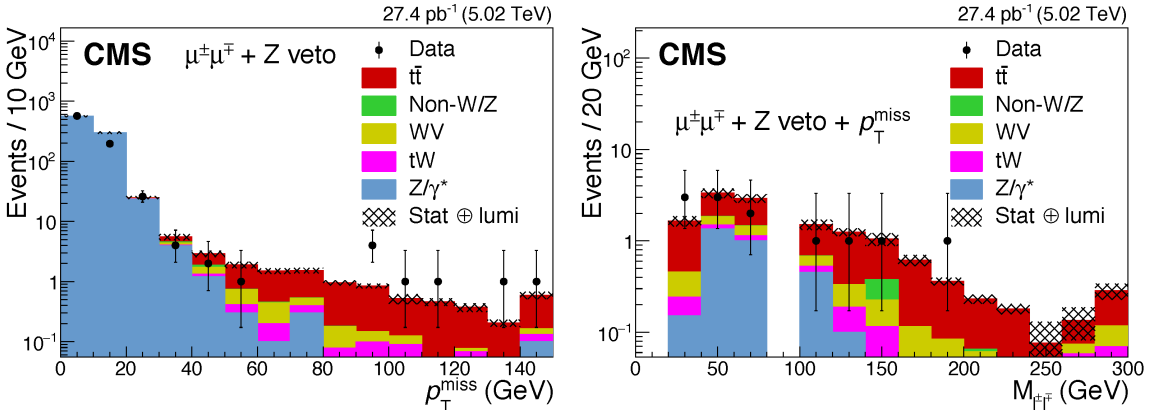

Figure 7.7: Predicted and observed distributions of the (left) P_T^{miss}in events passing the dilepton criteria and Z boson veto, and of the (right) invariant mass of the lepton pair after the P_T^{miss}> 35 GeV requirement in the $(\mu^{\pm}\mu^{\mp})$ channel. The cross-hatched band represents the statistical and integrated luminosity uncertainties in the expected signal and background yields added in quadrature. The vertical bars on the data points represent the statistical uncertainties. The last bin of the distributions contains the overflow events.

σ_{fid}. It is extrapolated to the full phase space in order to determine the inclusive $t\bar{t}$ cross section using the expression

$$\sigma_{t\bar{t}} = \frac{N - N_{\text{B}}}{\varepsilon\,\mathcal{A}\,\mathcal{L}} = \frac{\sigma_{\text{fid}}}{\mathcal{A}}, \tag{7.2.2}$$

where N denotes the number of observed dilepton events in data, N_{B} is the number of background events, ε is the selection efficiency, $\mathcal{A}$ denotes the acceptance, and $\mathcal{L}$ is the integrated luminosity. Table 7.3 shows the total number of events observed, together with the total number of signal and background events determined from simulation or data, after the full set of selection criteria. The total detector, trigger, and reconstruction efficiency is estimated from data to be $\varepsilon = 0.55 \pm 0.02$ (0.57 ± 0.04) in the $(e^{\pm}\mu^{\mp})((\mu^{\pm}\mu^{\mp}))$ channel. Using the definitions above, the yields from Table 7.3, and the systematic uncertainties from Table 7.4, the measured fiducial cross section for $t\bar{t}$ production is

$$\sigma_{\text{fid}} = 41 \pm 10\ (stat) \pm 2\ (syst) \pm 1\ (lumi)\ pb$$

Table 7.3: The predicted and observed numbers of dilepton events attained after applying all the selections. The values are given for each individual source of background, $t\bar{t}$ signal, and data. The uncertainties correspond to the statistical component.

Source	$(e^{\pm}\mu^{\mp})$	$(\mu^{\pm}\mu^{\mp})$
tW	0.92 ± 0.02	0.29 ± 0.01
$Non-WZ$leptons	1.0 ± 0.9	0.04 ± 0.01
Z/γ^*	1.6 ± 0.4	1.05 ± 0.37
WV	0.44 ± 0.02	0.15 ± 0.01
$t\bar{t}$signal	18.0 ± 0.3	6.36 ± 0.16
Total	22.0 ± 0.9	7.9 ± 0.4
Observed Data	24	7

in the $(e^{\pm}\mu^{\mp})$ channel and

$$\sigma_{\text{fid}} = 22 \pm 11\ (stat) \pm 4\ (syst) \pm 1\ (lumi)\ pb$$

in the $(\mu^{\pm}\mu^{\mp})$ channel.

The acceptance, as estimated from MC simulation, is found to be $\mathcal{A} = 0.53 \pm 0.01$ (0.37 ± 0.01) in the $(e^{\pm}\mu^{\mp})((\mu^{\pm}\mu^{\mp}))$ channel. The statistical uncertainty (from MC simulation) is included in the uncertainty in $\mathcal{A}$. By extrapolating to the full phase space, the inclusive $t\bar{t}$ cross section is measured to be

$$\sigma_{t\bar{t}} = 77 \pm 19\ (stat) \pm 4\ (syst) \pm 2\ (lumi)\ pb$$

in the $(e^{\pm}\mu^{\mp})$ channel and

$$\sigma_{t\bar{t}} = 59 \pm 29(stat) \pm 11(syst) \pm 1(lumi)pb$$

in the $(\mu^{\pm}\mu^{\mp})$ channel. Table 7.4 summarizes the relative and absolute statistical and systematic uncertainties from different sources contributing to $\sigma_{t\bar{t}}$. The cross sections, measured with a relative uncertainty of 25 and 52%, are in agreement with the SM prediction (Eq. (6.2.1)) within the uncertainties in the measurements.

Table 7.4: Summary of the individual contributions to the systematic uncertainty in the $\sigma_{t\bar{t}}$ measurements for the dilepton channels. The relative uncertainties $\Delta\sigma_{t\bar{t}}/\sigma_{t\bar{t}}$ (in %), as well as absolute uncertainties in $\sigma_{t\bar{t}}$, $\Delta\sigma_{t\bar{t}}$ (in pb), are presented. The statistical and total uncertainties are also given, where the latter are the quadrature sum of the statistical and systematic uncertainties.

	$(e^{\pm}\mu^{\mp})$		$(\mu^{\pm}\mu^{\mp})$	
Source	$\Delta\sigma_{t\bar{t}}$ (pb)	$\Delta\sigma_{t\bar{t}}$ /$\sigma_{t\bar{t}}$ (%)	$\Delta\sigma_{t\bar{t}}$ (pb)	$\Delta\sigma_{t\bar{t}}$ /$\sigma_{t\bar{t}}$ (%)
Electron efficiencies	1.0	1.4	—	—
Muon efficiencies	2.3	3.0	3.6	6.1
Jet energy scale	1.0	1.3	0.7	1.3
Jet energy resolution	0.05	0.06	0.04	0.06
Missing transverse energy	—	—	0.4	0.7
μ_R/μ_F scale of $t\bar{t}$signal (PS)	0.9	1.2	1.0	1.7
μ_R/μ_F scale of $t\bar{t}$signal (ME)	0.1	0.2	0.6	1.1
Hadronization model of $t\bar{t}$signal	0.9	1.2	3.1	5.2
PDF	0.4	0.5	0.2	0.4
MC statistics	1.1	1.4	1.4	2.4
tW background	1.1	1.4	0.9	1.6
WV background	0.5	0.7	0.5	0.9
Z/γ^* background	2.1	2.7	9.1	15.4
Non W/Z background	1.9	2.5	0.4	0.7
Total systematic (w/o luminosity)	4.4	5.8	10.6	17.9
Integrated luminosity	1.8	2.3	1.4	2.3
Statistical uncertainty	18.7	24.5	28.7	48.4
Total	19.3	25.2	30.6	51.7

7.2.3 Combination

The three individual $\sigma_{t\bar{t}}$ measurements are combined using the BLUE method [97] to determine an overall $t\bar{t}$ cross section. All systematic uncertainties are considered as fully correlated across all channels, with the following exceptions: the uncertainty associated with the finite event size of the simulated samples is taken as uncorrelated; the electron identification is not relevant for the $\mu\mu$ channel; and the b tagging and QCD multijet background uncertainties are only considered for the ℓ+jets channel. In the ℓ+jets channel, the WV and Z/γ^* backgrounds are not considered separately

but as part of the "Other backgrounds" component, which is dominated by tW events. The uncertainty associated with this category is therefore treated as fully correlated with the tW uncertainty in the dileptonic channels and uncorrelated with the WV and Z/γ^* uncertainties.

The combined inclusive $t\bar{t}$ cross section is measured to be:

$$\sigma_{tot}(\mathrm{p}p \to t\bar{t}) \;=\; 69.5 \pm 6.1\ (stat.) \pm 5.6\ (syst.) \pm 1.6\ (lumi.)\ \mathrm{p}b \;=\; 69.5 \;\pm\; 8.4\ (total)\ \mathrm{p}b.$$

where the total uncertainty is the sum in quadrature of the individual uncertainties. The weights of the individual measurements, to be understood in the sense of Ref. [97], are 81.8% for ℓ+jets, 13.5% for $(e^{\pm}\mu^{\mp})$, and 4.7% for $(\mu^{\pm}\mu^{\mp})$ channels.

The combined result is found to be robust by performing an iterative variant of the BLUE method [98] and varying some assumptions on the correlations of different combinations of systematic uncertainties. Also, the post-fit correlations between the nuisance parameters in the ℓ+jets channel have been checked and found to have negligible impact.

Fig. 7.8 presents a summary of CMS measurements [9, 10, 11, 12] of $\sigma_{t\bar{t}}$ in pp collisions at different $\sqrt{s}$ in the $l + jets$ and dilepton channels, compared to the $NNLO + NNLL$ prediction using the NNPDF3.0 PDF set with $\alpha_{\mathrm{s}}(M_Z) = 0.118$ and $m_{\mathrm{top}} = 172.5\,GeV$. In the inset, the results from this analysis at $\sqrt{s} = 5.02TeV$ are also compared to the predictions from the MMHT14 [15], CT14 [16], and ABMP16 PDF sets, with the latter using $\alpha_{\mathrm{s}}(M_Z) = 0.115$ and $m_{\mathrm{top}} = 170.4\,GeV$. Theoretical predictions using different PDF sets have comparable values and uncertainties, once consistent values of α_{s} and m_{top} are associated with the respective PDF set.

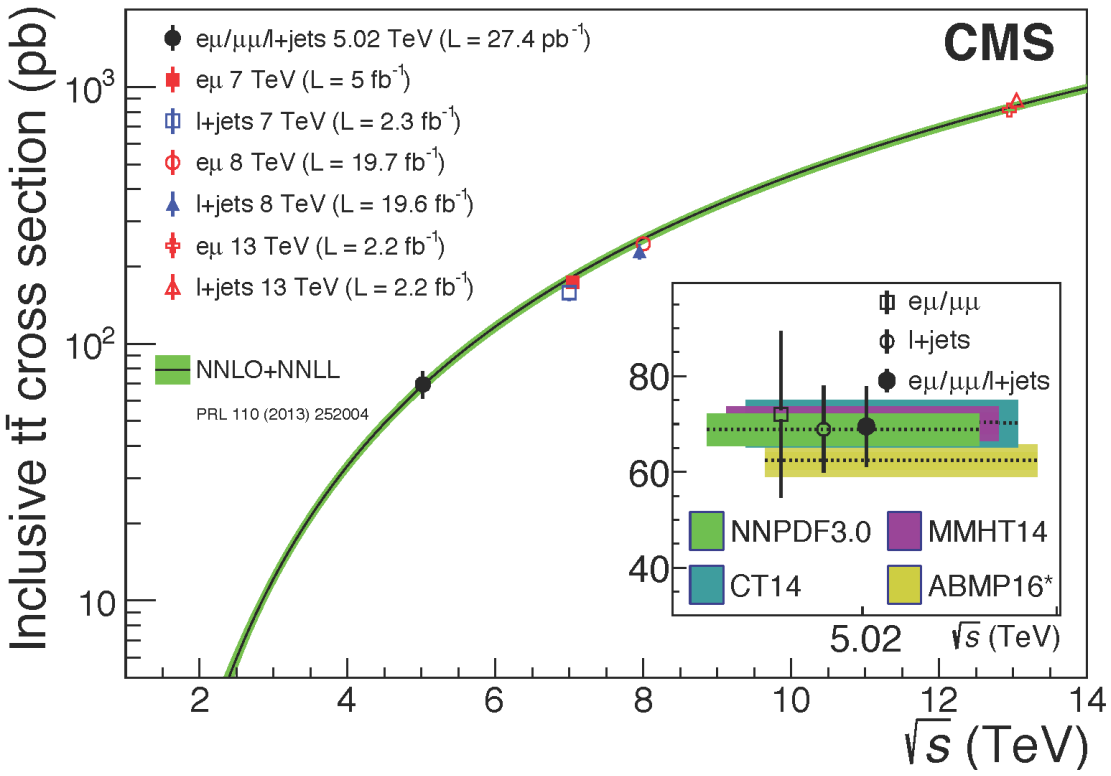

Figure 7.8: Inclusive $\sigma_{t\bar{t}}$in pp collisions as a function of the center-of-mass energy; previous CMS measurements at $\sqrt{s} = 7$, 8 [9, 10], and 13 [11, 12]TeVin the separate ℓ+jets and dilepton channels are displayed, along with the combined measurement at 5.02 TeV from this analysis. The NNLO+NNLL theoretical prediction [13] using the NNPDF3.0 [14] PDF set with $\alpha_s(M_Z) = 0.118$ and $m_{top} = 172.5\,GeV$ is shown in the main plot. In the inset, additional predictions at $\sqrt{s} = 5.02$ TeV using the MMHT14 [15], CT14 [16], and ABMP16 PDF sets, the latter with $\alpha_s(M_Z) = 0.115$ and $m_{top} = 170.4\,GeV$, are compared, along with the NNPDF3.0 prediction, to the individual and combined results from this analysis. The bars and bands represent the total uncertainties in the data and in the predictions, respectively.

7.3 QCD analysis

To illustrate the impact of the $\sigma_{t\bar{t}}$ result at $\sqrt{s} = 5.02\ TeV$on the knowledge of the proton PDFs, the results are used in a QCD analysis at NNLO, along with the joint measurements of neutral- and charged-current cross sections for deep inelastic

electron- and positron-proton scattering (DIS) at HERA [99], and the CMS measurement [100] of the muon charge asymmetry in W boson production at $\sqrt{s} = 8\,\text{TeV}$. The latter data set is used in order to improve the constraint on the light-quark distributions.

Version 2.0.0 of xFitter [101, 102], the open-source QCD-analysis framework for PDF determination, is employed, with the partons evolved using the Dokshitzer–Gribov–Lipatov–Altarelli–Parisi equations [103, 104, 105, 106, 107, 108] at NNLO, as implemented in the QCDNUM 17-01/13 program [109]. The treatment and the choices for the central values and variations of the c and b quark masses, the strong coupling, and the strange-quark content fraction of the proton follow that of earlier CMS analyses, e.g., Ref. [100]. The $\mu_\text{R}, \mu_\text{F}$ scales are set to the four-momentum transfer in the case of the DIS data, the W boson mass for the muon charge asymmetry results, and the top quark mass in the case of $\sigma_{t\bar{t}}$.

The systematic uncertainties in all three measurements of $\sigma_{t\bar{t}}$ and their correlations are treated the same way as in the combination described in Section 7.2.3. The theoretical predictions for $\sigma_{t\bar{t}}$ are obtained at NNLO using the HATHOR calculation [110], assuming $m_\text{top} = 172.5\,GeV$. The bin-to-bin correlations of the experimental uncertainties in the muon charge asymmetry and DIS measurements are taken into account. The theoretical predictions for the muon charge asymmetry are obtained as described in Ref. [100].

The procedure for the determination of the PDFs follows the approach used in the QCD analysis of Ref. [100] and results in a 14-parameter fit. The parametrized PDFs are the gluon distribution, xg, the valence quark distributions, xu_v, xd_v, and the u-type and d-type antiquark distributions, $x\overline{U}$, $x\overline{D}$. The relations $x\overline{U} = x\overline{u}$ and $x\overline{D} = x\overline{d} + x\overline{s}$ are assumed at the initial scale of the QCD evolution $Q_0^2 = 1.9\,GeV^2$. At this scale, the parametrizations are of the form:

$$xg(x) = A_g x^{B_g} (1-x)^{C_g} (1 + D_g x), \tag{7.3.1}$$

$$xu_v(x) = A_{u_v} x^{B_{u_v}} (1-x)^{C_{u_v}} (1 + D_{u_v} x + E_{u_v} x^2), \tag{7.3.2}$$

$$xd_v(x) = A_{d_v} x^{B_{d_v}} (1-x)^{C_{d_v}}, \tag{7.3.3}$$

$$x\overline{U}(x) = A_{\overline{U}} x^{B_{\overline{U}}} (1-x)^{C_{\overline{U}}} (1 + E_{\overline{U}} x^2), \tag{7.3.4}$$

$$x\overline{D}(x) = A_{\overline{D}} x^{B_{\overline{D}}} (1-x)^{C_{\overline{D}}}. \tag{7.3.5}$$

The normalization parameters A_{u_v}, A_{d_v}, and A_g are calculated by the QCD sum rules. Additional constraints $B_{\overline{U}} = B_{\overline{D}}$ and $A_{\overline{U}} = A_{\overline{D}}(1 - f_s)$ are imposed, with f_s being the strangeness fraction, $s/(d+s)$, which is set to 0.31 ± 0.08 as in Ref. [111], consistent with the value obtained using the CMS measurements of W+c production [112]. Using the measured values for $\sigma_{t\bar{t}}$ allows the addition of a new free parameter, D_{u_v}, in Eq. (7.3.2), as compared to the analysis in Ref. [100].

The predicted and measured cross sections for all the data sets, together with their corresponding uncertainties, are used to build a global χ^2, minimized to determine the PDF parameters [101, 102]. The results of the fit are given in Table 7.9. The quality of the overall fit can be judged based on the global χ^2 divided by the number of degrees of freedom, n_{dof}. For each data set included in the fit, the partial χ^2 divided by the number of the measurements (data points), n_{dp}, is also provided. The correlated part of χ^2, also given in Table 7.9, quantifies the influence of the correlated systematic uncertainties in the fit. The global and partial χ^2 values indicate a general agreement among all the data sets.

The experimental uncertainties in the measurements are propagated to the extracted QCD fit parameters using the MC method [113, 114]. In this method, 400 replicas of pseudo-data are generated, with measured values for $\sigma_{t\bar{t}}$ allowed to vary within the statistical and systematic uncertainties. For each of them, the PDF fit is performed and the uncertainty is estimated as the RMS around the central value. In

Data sets	Partial χ^2/n_{dp}
HERA1+2 neutral current, e^+p, $E_p = 920$ GeV	449/377
HERA1+2 neutral current, e^+p, $E_p = 820$ GeV	71/70
HERA1+2 neutral current, e^+p, $E_p = 575$ GeV	224/254
HERA1+2 neutral current, e^+p, $E_p = 460$ GeV	218/204
HERA1+2 neutral current, e^-p, $E_p = 920$ GeV	218/159
HERA1+2 charged current, e^+p, $E_p = 920$ GeV	43/39
HERA1+2 charged current, e^-p, $E_p = 920$ GeV	53/42
CMS $W^{\pm}$ muon charge asymmetry $\mathcal{A}(\eta_\mu)$, $\sqrt{s} = 8$ TeV	3/11
CMS inclusive $t\bar{t}$ 5 TeV, $e\mu$	1.31/1
CMS inclusive $t\bar{t}$ 5 TeV, $\mu\mu$	0.00/1
CMS inclusive $t\bar{t}$ 5 TeV, l+jet	0.33/1
Correlated χ^2	100
Global χ^2/n_{dof}	1387/1145

Figure 7.9: Partial χ^2 per number of data points, n_{dp}, and the global χ^2 per degrees of freedom, n_{dof}, from analysis of DIS data, and the $\sigma_{t\bar{t}}$ results at $\sqrt{s} = 5.02$ TeV from this analysis. The correlated part of the global χ^2 value is also given.

Fig. 7.10, the ratio and the relative uncertainties in the gluon distributions, as obtained in the QCD analyses with and without the measured values for $\sigma_{t\bar{t}}$, are shown. A moderate reduction of the uncertainty in the gluon distribution at $x \gtrsim 0.1$ is observed, once the measured values for $\sigma_{t\bar{t}}$ are included in the fit. The uncertainties in the valence quark distributions remain unaffected. All changes in the central values of the PDFs are well within the fit uncertainties.

Possible effects from varying the model input parameters and the initial PDF parametrization are investigated in the same way as in the similar analysis of Ref. [100].

The two cases when the measured values for $\sigma_{t\bar{t}}$ are included or excluded from the fit are considered, resulting in the same associated model and parametrization uncertainties.

In conclusion, the $\sigma_{t\bar{t}}$ measurements at $\sqrt{s} = 5.02\ TeV$ provide improved uncertainties in the gluon PDF at high x, though the impact is small, owing to the large experimental uncertainties.

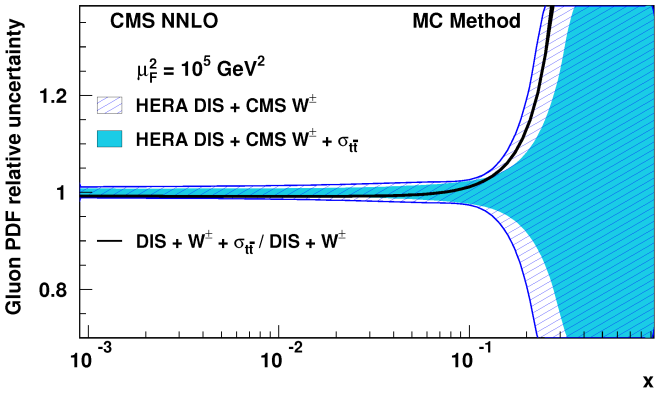

Figure 7.10: The relative uncertainties in the gluon distribution function of the proton as a function of x at $\mu_F^2 = 10^5\,GeV^2$ from a QCD analysis using the HERA DIS and CMS muon charge asymmetry measurements (hatched area), and also including the CMS $\sigma_{t\bar{t}}$ results at $\sqrt{s} = 5.02\,\text{TeV}$ (solid area). The relative uncertainties are found after the two gluon distributions have been normalized to unity. The solid line shows the ratio of the gluon distribution function found from the fit with the CMS $\sigma_{t\bar{t}}$ measurements included to that found without.

7.4 Summary

The first measurement of the top quark pair ($t\bar{t}$) production cross section in pp collisions at $\sqrt{s} = 5.02\,\text{TeV}$ is presented for events with one or two leptons and at least two jets, using a data sample collected by the CMS experiment, corresponding to an integrated luminosity of $27.4 \pm 0.6\ pb^{-1}$. The final measurement is obtained

from the combination of the measurements in the individual channels. The result is $\sigma_{t\bar{t}} = 69.5 \pm 6.1(stat) \pm 5.6(syst) \pm 1.6(lumi)\ pb$, with a total relative uncertainty of 12%, which is consistent with the standard model prediction. The impact of the measured $t\bar{t}$ cross section in the determination of the parton distribution functions of the proton is studied in a quantum chromodynamics analysis at next-to-next-to-leading order. A moderate decrease of the uncertainty in the gluon distribution is observed at high values of x, the fractional momentum of the proton carried by the gluon.

Conclusion and Summary

Over the past several years, the Compact Muon Solenoid (CMS) experiment has successfully dealt with the collisions the Large Hadron Collider (LHC) has delivered. In the search for new physics, some interesting events distinguish themselves through their muonic signatures. With its strong magnetic field, CMS is capable of measuring the transverse momentum of muons with high precision through its extensive tracker and muon system. First major part of this thesis dealt with one sub detector in the muon system, the Resistive Plate Chamber (RPC) which plays a crucial role in muon trigger because of its high time resolution ability.

To start with, all of its hardware had to be in place and functional. With 1056 chambers, each in need of gas supplies, High Voltage for its electric field, Low Voltage for its electronics and cables for control and readout, this is a complex system with the potential for a wide arrange of human and software errors. In addition, several parameters had to be tuned before the arrival of LHC collisions. The commissioning activities surrounding each of these services plus careful analysis of cosmic rays data constitute the first part of this PhD along with analysing the data collision data, defining the optimum operating voltage of every single chamber with a suitable average cluster size which is a key requirement of CMS trigger and operating at the region with stable efficiency.

Collisions data taken during 2015 and 2016 at 13 TeV has been exploited to study the key detector performance parameters and stability of the system in the conditions of high instantaneous luminosity and high number of pile up (PU) events are presented in a view of history monitoring and stable trend. RPC background, currents and charge was studied in depth with increasing luminosity and dat driven estimations of all these parameters are reported at the extreme conditions of High Luminosity LHC (HL-LHC). CMS RPC system operated well during RUN-2 (2015-2016) delivering good triggers and data for physics. At the end of 2016 the fraction of active channels was about 98.6%. After the LS1 running with increasing instantaneous luminosity and 13 years after the first RPCs have been assembled, the detector performance is within CMS specifications and stable with no degradation observed. From the studies of measured background and currents, no significant issues were found for running up to high luminosity scenarios.

The top quark, the heaviest elementary particle in the standard model (SM), has been the subject of numerous detailed studies using hadron-hadron collisions. The pair production ($t\bar{t}$) cross section ($\sigma_{t\bar{t}}$) as a function of center-of-mass energy is of interest for the extraction of the top quark pole mass and can be used to constrain the gluon distribution function at large fractions x of the proton longitudinal momentum carried by the gluon, where the gluon distribution is poorly known.

The second major part of this thesis is the key contribution to first measurement of the top quark pair ($t\bar{t}$) production cross section in pp collisions at $\sqrt{s} = 5.02\,\text{TeV}$ for events with one or two leptons and at least two jets, using a data sample collected by the CMS experiment in 2015, corresponding to an integrated luminosity of $27.4 \pm 0.6\ pb^{-1}$. The final measurement is obtained from the combination of the

measurements in the individual channels. The result is $\sigma_{t\bar{t}} = 69.5 \pm 6.1\ (stat) \pm 5.6\ (syst) \pm 1.6\ (lumi)\ pb$, with a total relative uncertainty of 12%, which is consistent with the standard model prediction. The impact of the measured $t\bar{t}$ cross section in the determination of the parton distribution functions of the proton is studied in a quantum chromodynamics analysis at next-to-next-to-leading order. A moderate decrease of the uncertainty in the gluon distribution is observed at high values of x, the fractional momentum of the proton carried by the gluon.

Appendix A
Data and MC samples analysed

We have used as starting point the HIN forest trees produced for the 5.02 TeV data and MC. The code used for our analysis is available in [115]. The study is based on an integrated luminosity of 27.4 ± 0.6 pb^{-1} [72].The average pileup in this dataset is estimated to be 1.4 and therefore. Overall standard Run II selections are used as they have been found to be adequate at a lower energy and pileup. We make use of the primary dataset with the unprescaled single lepton triggers, i.e.

/SingleMuHighPt/Run2015E-PromptReco/AOD

and

/FilteredHighPtPhoton30AndZ/Run2015E-PromptReco-v1/AOD.

The triggers used for data are
HLT_HIL2Mu15_v1 and HLT_HISinglePhoton40_Eta3p1_v1, while for MC HLT_HIL2Mu15ForPPRef_v1 and HLT_HISinglePhoton40_Eta3p1ForPPRef_v1 have been used.

In each run we excluded the luminosity sections flagged as bad according to the validations performed by each Detector Performance Group and Physics Object Group. Technically, we implement this by the use of the Cert_262081-262328_5TeV_PromptReco_Collisions15_25ns_JSON.txt json file. The

75X_dataRun2_v13 global tag is used to process data.

A.0.1 Simulation

The simulated $t\bar{t}$ events, along with their dependencies on the top quark mass, the renormalisation and factorisation scales, and the Parton Distribution Functions (PDFs), are generated using $POWHEG$ (v2) [34, 35] interfaced to $PYTHIA$ 8.2 [73, 74] for parton showering with the CUETP8M1 underlying event tune [116, 75]. NNPDF3.0 [117] is used as default PDF. The value of the top quark mass used in all simulated samples is m_t =172.5 GeV.

A similar setup is used for the simulation of the single top quark production in association with a W boson using $POWHEG$ (v1) [80]. Vector boson production in association with jets ($W$and DY+jets) are generated with the use of a MG5_aMC@NLO- [76], interfaced to $PYTHIA$for parton showering. The simulation includes up to two extra partons at matrix element level and uses the so-called FxFx matching procedure [77]. Residual contamination from double vector production (dibosons) are expected in dilepton final states. $WW/ZZ/WZ$ events are simulated with $POWHEG$.

A complete overview of all used simulated sample can be found in Fig. A.1. All the simulations include an emulation of the full detector response, based on GEANT 4 [118], assuming realistic alignment and calibration, tuned on data. Specific corrections for the selection efficiencies, energy scales and resolutions of the objects shall be detailed in the next sections. The 75X_mcRun2_asymptotic_ppAt5TeV_v3 global tag is used to process the MC simulations.

Monte Carlo datasets used in this analysis. "ppW16" is used as a shorthand for "HINppWinter16DR-75X_mcRun2_asymptotic_ppAt5TeV_v3". When not specified the samples are AODSIM. The samples are generated either inclusively or with a final state restricted to the leptonic mode, including electrons, muons, and taus. Where no references are given, the cross sections come from the generator itself. For the samples restricted to specific decay channels the branching ratio (BR) is included in the cross section value quoted.

Process	σ[pb]	Dataset name
$t\bar{t}$	68.9 (NLO+NNLL)	/TT_TuneCUETP8M1_5020GeV-powheg-pythia8/ppW16-v1/
		/TT_TuneCUETP8M1_5020GeV-powheg-scaledown-pythia8/ppW16-v1/
		/TT_TuneCUETP8M1_5020GeV-powheg-scaleup-pythia8/ppW16-v1/
		/TT_TuneEE5C_5020GeV-powheg-herwigpp/ppW16-v1
tW	3.04 (NNLL)	/ST_tW_5020GeV_top-powheg-pythia8/ppW16-v1
		/ST_tW_5020GeV_antitop-powheg-pythia8/ppW16-v1
$W(\to \ell\nu)$+jets	21159 (NNLO[QCD]+NLO[EWK])	/WJetsToLNu_TuneCUETP8M1_5020GeV-amcatnloFXFX-pythia8/ppW16-v1/
$Z/\gamma(\to \ell\ell)$+jets	2010 (NNLO[QCD]+NLO[EWK])	/DYJetsToLL_TuneCUETP8M1_5020GeV-amcatnloFXFX-pythia8/ppW16-v1
$WW(\to \ell\nu)$+jets	1.77 (NLO)	/WWTo2L2Nu_TuneCUETP8M1_5020GeV-powheg/ppW16-v1/
$ZZ(\to \ell\nu)$+jets	0.441 1.21 (NLO)	/WZTo3LNU_NNPDF30_TuneCUETP8M1_5020GeV-powheg/ppW16-v1/

Figure A.1: MC datasets used in this analysis

Appendix B
Fit performance

We perform the fits using the different variables proposed in Sec. 6.3.1. First the analysis is performed blindly using the Asimov dataset (apriori expectations for signal, backgrounds and corresponding uncertainties). The expected uncertainties for each variation of the fit are reported in Table B.1. We can observe that, as expected the fits in the muon channel have smaller statistical uncertainty than the electron channel (due to looser selection), while the systematics in the electron channel tend to be smaller (smaller background due to tighter cuts). Given that tighter cuts would however lead to an increase of the extrapolation uncertainty. we prefer to keep the selection in the muon channel as loose as possible. The change in the ranking of the light jet candidates does not lead, with this amount of integrated luminosity, to a significantly better uncertainty. However, after applying requirement on the maximum ΔR between the jets a decrease in the systematic uncertainty is overall observed, at the cost of a higher statistical uncertainty. Overall, the best performant analysis is expected to be the one in which the ΔR distribution of the two light jet candidates is fit. Besides discriminating clearly signal from background, it is also robust to jet energy scale/resolution uncertainties given it's based on angular quantities. The gain in final uncertainty over the baseline cut-in-categories is estimated to be $\approx$12%, as

such we shall use it for the final result to be reported.

Table B.1: Expected results for the signal strength fit using different variations of the analysis. The statistical and systematics components are reported as well as the final relative uncertainty, after symmetrization, in parenthesis.

Analysis	Channel e+jets	μ+jets	ℓ+jets
cut-in-categories	$^{+0.18}_{-0.16}(stat)^{+0.18}_{-0.13}(sys)(23\%)$	$^{+0.13}_{-0.12}(stat)^{+0.28}_{-0.12}(sys)(24\%)$	$^{+0.10}_{-0.10}(stat)^{+0.19}_{-0.11}(sys)(18\%)$
$M(j,j')$, by P_T	$^{+0.18}_{-0.16}(stat)^{+0.17}_{-0.13}(sys)(23\%)$	$^{+0.13}_{-0.12}(stat)^{+0.27}_{-0.11}(sys)(23\%)$	$^{+0.10}_{-0.10}(stat)^{+0.18}_{-0.10}(sys)(17\%)$
$M(j,j')$, by ΔR	$^{+0.18}_{-0.16}(stat)^{+0.17}_{-0.12}(sys)(23\%)$	$^{+0.13}_{-0.12}(stat)^{+0.26}_{-0.11}(sys)(23\%)$	$^{+0.10}_{-0.10}(stat)^{+0.19}_{-0.11}(sys)(18\%)$
$M(j,j')$, by $\Delta R < 2$	$^{+0.20}_{-0.18}(stat)^{+0.16}_{-0.11}(sys)(23\%)$	$^{+0.15}_{-0.14}(stat)^{+0.26}_{-0.11}(sys)(23\%)$	$^{+0.12}_{-0.11}(stat)^{+0.17}_{-0.09}(sys)(18\%)$
$\Delta R(j,j')$	$^{+0.17}_{-0.16}(stat)^{+0.15}_{-0.11}(sys)(21\%)$	$^{+0.13}_{-0.12}(stat)^{+0.25}_{-0.10}(sys)(22\%)$	$^{+0.10}_{-0.10}(stat)^{+0.17}_{-0.09}(sys)(16\%)$

B.0.1 Fit results

We now compare the results obtained applying the fit procedure optimized in the previous section to the data. We compare two results:

cut-in-categories - events are counted in different categories containing different levels of $t\bar{t}$purity. The categories are defined by the number of b-tagged jets in addition to the two non b-tagged jets expected to stem from the $W \to qq'$ decay.

shape analysis - for the same categories defined above we perform a combined fit of ΔR of the closest non b-tagged dijet system.

Table B.2: Expected and observed results for the signal strength fit. The total uncertainty (statistics+systematics) is reported.

Analysis		Channel e	μ	combined
cut	exp.	$1.00^{+0.18}_{-0.16}(stat)^{+0.18}_{-0.13}(sys)(23\%)$	$1.00^{+0.13}_{-0.12}(stat)^{+0.28}_{-0.12}(sys)(24\%)$	$1.00^{+0.10}_{-0.10}(stat)^{+0.19}_{-0.11}(sys)(18\%)$
	obs.	$1.08^{+0.18}_{-0.17}(stat)^{+0.19}_{-0.14}(sys)(24\%)$	$1.00^{+0.13}_{-0.12}(stat)^{+0.26}_{-0.11}(sys)(23\%)$	$1.03^{+0.10}_{-0.10}(stat)^{+0.21}_{-0.11}(sys)(19\%)$
shape	exp.	$1.00^{+0.17}_{-0.16}(stat)^{+0.15}_{-0.11}(sys)(21\%)$	$1.00^{+0.13}_{-0.12}(stat)^{+0.25}_{-0.10}(sys)(22\%)$	$1.00^{+0.10}_{-0.10}(stat)^{+0.17}_{-0.09}(sys)(16\%)$
	obs.	$1.05^{+0.17}_{-0.16}(stat)^{+0.12}_{-0.10}(sys)(20\%)$	$0.97^{+0.12}_{-0.12}(stat)^{+0.10}_{-0.10}(sys)(15\%)$	$1.00^{+0.10}_{-0.09}(stat)^{+0.09}_{-0.08}(sys)(13\%)$

The addition of the distance between the two light jets opens the possibility to trace the jet counting from a background-dominated region to the signal region and

is able to constrain the backgrounds, and some of the signal uncertainties. With respect to the invariant mass variable, it is found to be less prone to jet energy scale/resolution, hadronization and parton shower related uncertainties. However, due to low statistics of the dataset, the constraints obtained aren't as strong as they could be.

Figure B.1 displays the full correlation matrix between all nuisance parameters and freely floating parameters in the fit. Most parameters are found to be uncorrelated after the fit is performed. Some noticeable correlations are however found between the QCD scale choices in the W+jets simulation, and between the jet energy scale uncertainties and the W+jets QCD scale choices.

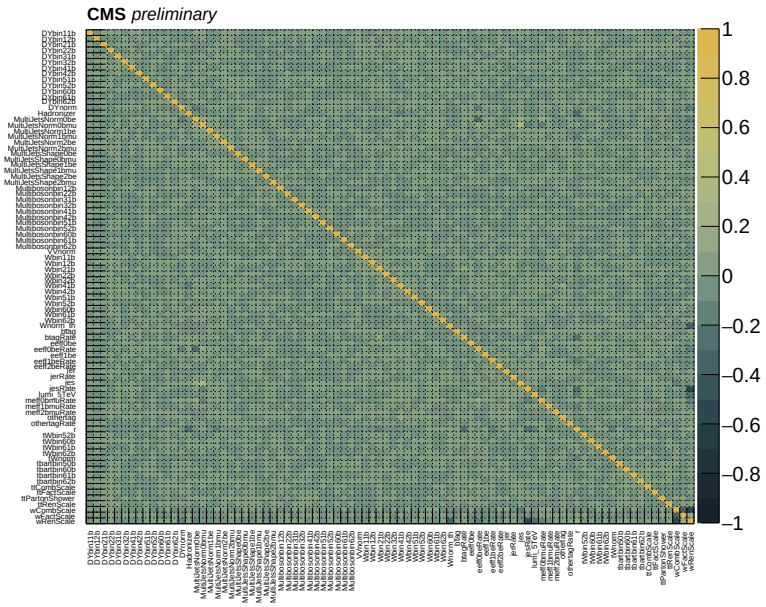

Figure B.1: Post-fit correlation matrix between the free parameters in the fit.

We have furthermore compared the observed central value and total uncertainty with the expectations from simulation, using toy experiments where the yields and

systematic variations are considered. Fig. B.2 shows the distribution of the signal strength (left) and total uncertainty (right) in the toy experiments. The expected signal strength is correctly centred at 1, as expected from an unbiased fit. The total uncertainty, is expected to be in average larger than the one observed. The p-value for the observed uncertainty is estimated to be 14%.

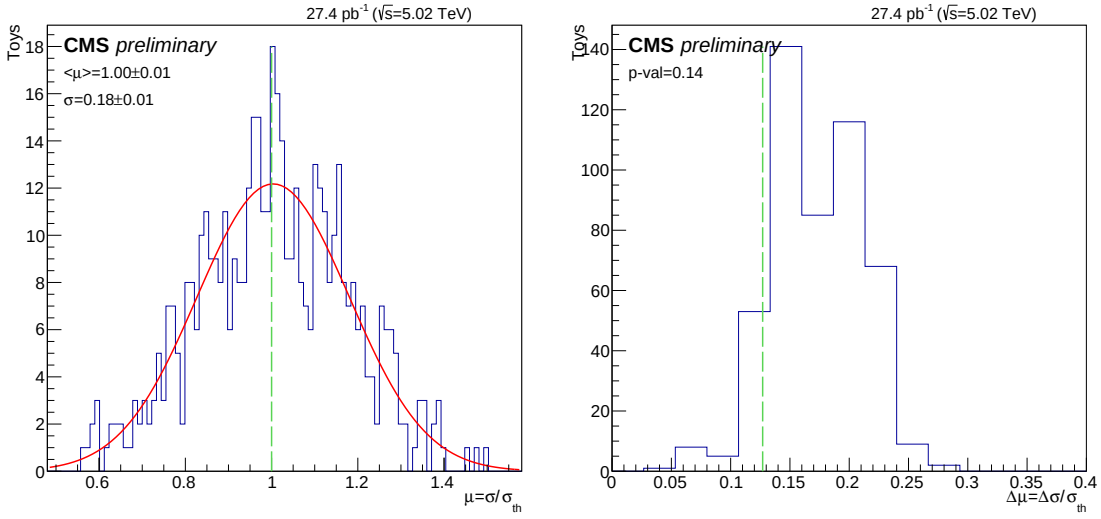

(a) (b)

Figure B.2: Expected signal strength (a) and total uncertainty (b) from the fit to the distributions using toy experiments.

In order to estimate the impact of the uncertainties on the signal strength fit repeat the fit fixing one nuisance at the time at its post fit $\pm 1\sigma$ value. The impact on the signal strength fit is then evaluated from the difference induced in the final result from this procedure. The result obtained is reported in Table 7.2.

With respect to the cut-in-categories analysis, the shape analysis seems to be less prone to the uncertainties in the QCD background, jet energy resolution and signal

modelling (hadronizer and PS scale). In both cases the signal modelling uncertainties (hadronizer and PS scales) and the b-tagging efficiency are the leading uncertainties.

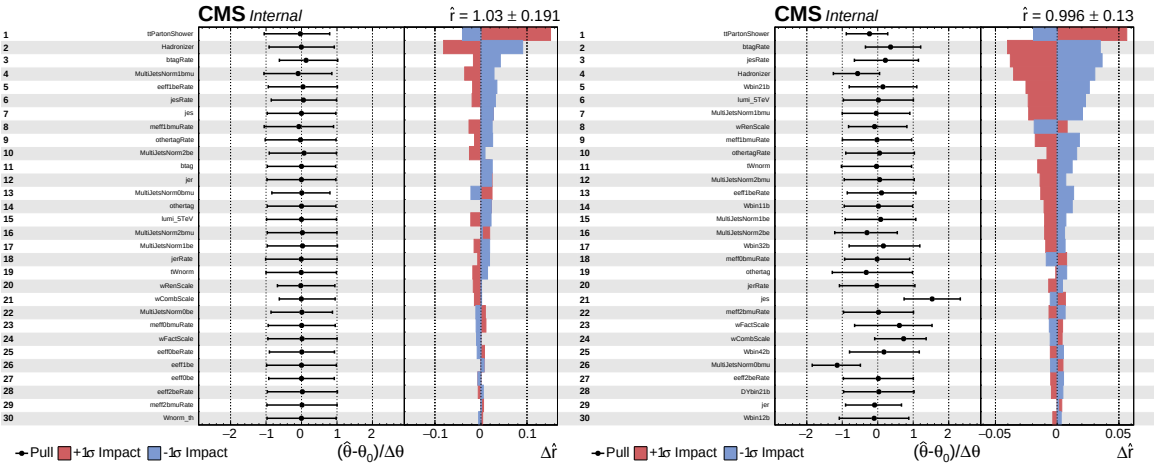

(a) (b)

Figure B.3: Representation of the nuisances with most significant impact on the fit in the cut-in-categories (a) and shape (b) analyses. In each plot, the left pad shows the name of the nuisances, the center pad represents the post-fit uncertainties and value of the nuisances. The right pad represents the variation induced in the signal strength extracted when the nuisance is fixed at $\pm 1\sigma$ of its postfit value.

Appendix C
Lepton Trigger Efficiencies

In order to determine the electron trigger efficiency and the scale factor to correct the simulated one, we have made use of $Z \rightarrow e^+e^-$ events and the tag-and-probe method [119]. The Tag and Probe ("TnP") method utilizes two-body decays of a well established resonance (J/ψ, Υ, Z bosons) to identify a high purity region around the pole mass, where particles of the desired type can be selected with looser criteria than the ones applied in the analysis. One of the legs of the decay (the "tag") is selected with a tight criteria, while the second leg (the "probe") is typically selected applying solely an invariant mass requirement on the system formed with the tag and without requesting any further, e.g. identification or isolation, criteria. The efficiency can then be sequentially measured in-situ by counting the candidates which pass the necessary reconstruction, identification and isolation cuts. For our analysis, $Z \rightarrow e^+e^-$ decays are used as a high-purity, unbiased source of electrons from which to extract their selection efficiencies [120]. Some fit examples are illustrated in Fig. C.2

Fig. C.1 shows the trigger efficiencies measured in data and the scale factor, with respect to the simulated efficiency.

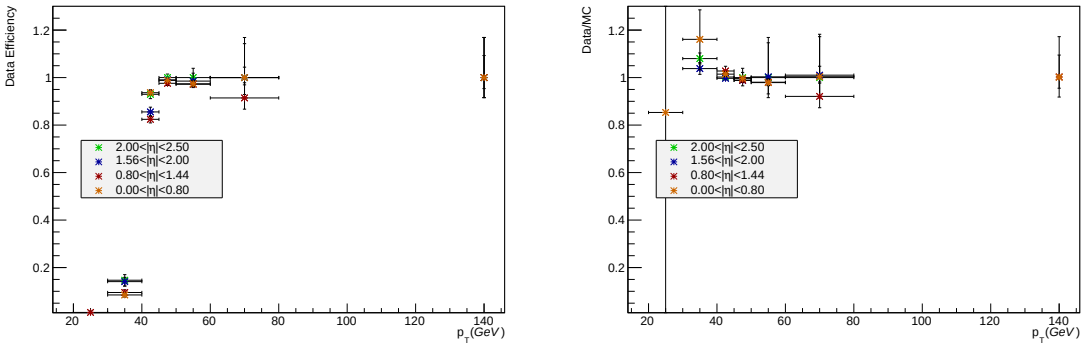

Figure C.1: Left: Trigger efficiency, as function of the electron P_T and different pseudo-rapidity ranges, measured in data. Right: data to simulation ratio of the efficiency (scale factor) as a function of the electron P_T.

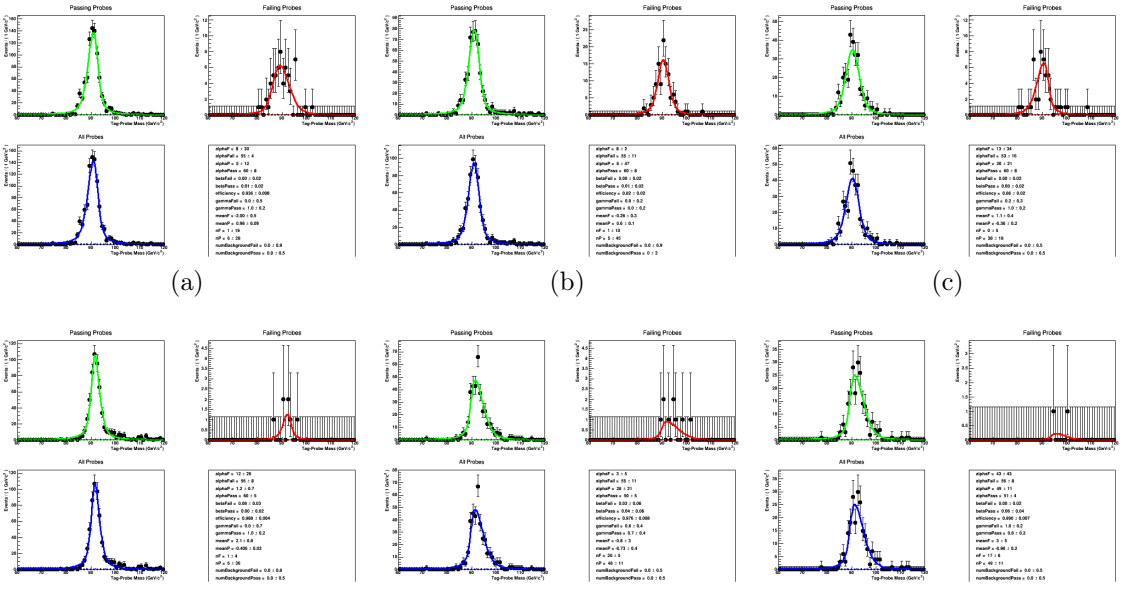

Figure C.2: Fit results used to extract the electron trigger efficiency for different $P_T - \eta$ ranges. Top: $40 < P_T < 50\ GeV$. Bottom: $50 < P_T < 60\ GeV$. From left to right: $|\eta| < 0.8$, $0.8 < |\eta| < 1.442$ and $1.56 < |\eta| < 2$

Appendix D
Selected Publications During PhD

- **Measurement of the inclusive $t\bar{t}$ cross section in pp collisions at $\sqrt{s} = 5.02\ TeV$ using final states with at least one charged lepton**

  J. High Energ. Phys.

  https://doi.org/10.1007/JHEP03(2018)115

- **Measurement of the $t\bar{t}$ production cross section using events with one lepton and at least one jet in pp collisions at $\sqrt{s} = 13\ TeV$**

  J. High Energ. Phys.

  https://doi.org/10.1007/JHEP09(2017)051

- **First results of CMS RPC performance at 13 TeV**

  JINST, 2016

  http://stacks.iop.org/1748-0221/11/i=12/a=C12003

- **Performance of the CMS muon detector and muon reconstruction with proton-proto collisions at $\sqrt{s} = 13\ TeV$**

  Submitted to JINST

  https://arxiv.org/abs/1804.04528

- **The CMS RPC detector performance during LHC Run-II data taking**

  SISA, 2017

  https://pos.sissa.it/314/804/pdf

- **TDR for the Phase-2 Upgrade of the CMS Muon Detectors**

  CMS-TDR-17-003

- **R&D towards the CMS RPC Phase-2 upgrade**

  JINST, 2017 11 C09017

Appendix E

Major Talks and Posters Presented During PhD

- **CMS RPC Operation and Performance stability during LHC RUN II Data taking**

  XIV Workshop on Resistive Plate Chambers and related detectors (RPC2018), 19-23 February 2018 Puerto-Vallarta-Mexico

- **CMS RPC Status and Performance during RUN II**

  European Society of Physics conference of High Energy Physics, EPS-HEP-2017, Venice-Italy

- **Comparison of CMS RPC performance during RUNi and RUN II**

  XIII Workshop on Resistive Plate Chambers and related detectors (RPC2016), 22-26 February 2016 Ghent-Belgium

- **First results of CMS RPC at 13 TeV Data taking.**

  38th International Nathiagali Summer College 2015, National Center for Physics,

August, 2015, Islamabad-Pakistan

E.1 Other Schools/Workshops Attended During PhD

- CERN Fermilab Hadron Collider Physics School 2014 at CERN-Geneva
- CERN Fermilab Hadron Collider Physics School 2012 at FermiLab Chicago, USA
- First Asia Europe Pacific School of High Energy Physics on October 13-27, 2012. Fukuoka-Japan

Appendix F

CMS RPC Achievement Award, 2016

XIII Workshop on
Resistive Plate Chambers and Related Detectors
Ghent University, Belgium
February 22-26, 2016

RPC 2016

UNIVERSITEIT GENT

Best Young Researcher Poster Award
Certificate

The Best Young Researcher Poster Award has been offered to

Mehar Ali SHAH

for the poster entitled

"Comparison of CMS RPC performance during LHC Run1 and Run 2"

presented at the ***XIII Workshop on Resistive Plate Chambers and Related Detectors***, held at Ghent University – Het Pand, Ghent, Belgium, from 22 to 26 February, 2016.

Ghent, 26 February, 2016

Dr. Michael Tytgat
Workshop Chair

Prof. Rinaldo Santonico
International Advisory Committee Chair

Prize sponsored by the Belgian Physical Society

Bibliography

[1] G. Kane. The dawn of physics beyond the standard model. *Scientific American, vol. Sp 15, pp. 4−11*, 2006.

[2] E. Drexler. Elementary particle interactions in the standard model. *Wikipedia*, April 2014.

[3] F. Marcastel. CERN Accelerator Complex. La chaîne des accélérateurs du CERN. October 2013. `http://cds.cern.ch/record/1621583.`

[4] J. Stirling. Tevatron and lhc parton luminosity comparison plots. `http://www.hep.ph.ic.ac.uk/~wstirlin/plots/plots.html.`

[5] CMS Collaboration. CMS Luminosity Measurement for the 2015 Data Taking Period. 2016.

[6] M.I. Pedraza-Morales, M.A. Shah, and M. Shopova. First results of cms rpc performance at 13 *tev*. *Journal of Instrumentation*, 11(12):C12003, 2016.

[7] CMS collaboration. The performance of the cms muon detector in proton-proton collisions at $\sqrt{s} = 7$ tev at the lhc. *Journal of Instrumentation*, 8(11):P11002, 2013.

[8] CMS Collaboration. The Muon Project, Technical Design Report,. *CERN/LHCC 97-32*, 1997.

[9] Vardan Khachatryan et al. Measurement of the $t\bar{t}$ production cross section in the eμ channel in proton-proton collisions at $\sqrt{s} = 7$ and 8 TeV. *JHEP*, 08:029, 2016.

[10] Vardan Khachatryan et al. Measurements of the $t\bar{t}$ production cross section in lepton+jets final states in pp collisions at 8 TeV and ratio of 8 to 7 TeV cross sections. *Eur. Phys. J. C*, 77:15, 2017.

[11] Vardan Khachatryan et al. Measurement of the $\mathrm{t\bar{t}}$ production cross section using events in the eμ final state in pp collisions at $\sqrt{s} = 13$ TeV. *Eur. Phys. J. C*, 77:172, 2017.

[12] Albert M. Sirunyan et al. Measurement of the $\mathrm{t\bar{t}}$ production cross section using events with one lepton and at least one jet in pp collisions at $\sqrt{s} = 13\,\mathrm{TeV}$. *JHEP*, 09:051, 2017.

[13] M. Czakon, P. Fiedler and A. Mitov. Total Top-Quark Pair-Production Cross Section at Hadron Colliders Through $\mathrm{O}(\alpha_S^4)$. *Phys. Rev. Lett.*, 110:252004, 2013.

[14] Richard D. Ball et al. Parton distributions for the LHC Run II. *JHEP*, 04:040, 2015.

[15] L. A. Harland-Lang, A. D. Martin, P. Motylinski, and R. S. Thorne. Parton distributions in the LHC era: MMHT 2014 PDFs. *Eur. Phys. J.*, C75(5):204, 2015.

[16] Sayipjamal Dulat, Tie-Jiun Hou, Jun Gao, Marco Guzzi, Joey Huston, Pavel Nadolsky, Jon Pumplin, Carl Schmidt, Daniel Stump, and C. P. Yuan. New parton distribution functions from a global analysis of quantum chromodynamics. *Phys. Rev.*, D93(3):033006, 2016.

[17] Serguei Chatrchyan et al. Determination of the top-quark pole mass and strong coupling constant from the $t\bar{t}$ production cross section in pp collisions at $\sqrt{s} = 7TeV$. *Phys. Lett. B*, 728:496, 2013. [Erratum: 10.1016/j.physletb.2014.08.040].

[18] Georges Aad et al. Measurement of the $t\bar{t}$ production cross-section using eμ events with b-tagged jets in pp collisions at $\sqrt{s} = 7$ and 8 TeV with the ATLAS detector. *Eur. Phys. J. C*, 74:3109, 2014.

[19] Morad Aaboud et al. Measurement of the $t\bar{t}$ production cross-section using eμ events with b-tagged jets in pp collisions at $\sqrt{s} = 13$ TeV with the ATLAS detector. *Phys. Lett. B*, 761:136, 2016.

[20] Vardan Khachatryan et al. Measurement of the top quark pair production cross section in proton-proton collisions at $\sqrt{s} = 13$ TeV. *Phys. Rev. Lett.*, 116:052002, 2016.

[21] M. Thomson. Modern Particle Physics. *Cambridge University Press*, 2013.

[22] D. McMahon. Quantum Field Theory Demystified. *Rept. Prog*, 2005.

[23] G. Shaw B. R. Martin. Particle Physics. *Third edition, Wiley Publisher*, 2008.

[24] D. H. Perkins. Introduction to high energy physics. *Cambridge University Press*, 2000.

[25] G. Zweig. An SU(3) Model for Strong Interaction Symmetry and its Breaking. *CERN Report No.8182/TH.401*, 1964.

[26] The CDF experiment. Observation of Top Quark Production in $p\bar{p}$ Collisions. *Phys. Rev. Lett. 74*, 1995.

[27] The D0 experiment. Observation of the Top Quark. *Phys. Rev. Lett.*, 1995.

[28] CMS D0 ATLAS, CDF. First combination of Tevatron and LHC measurements of the top-quark mass. *arXiv1403.4427*, 2014.

[29] CMS twiki. . *https://twiki.cern.ch/twiki/bin/view/LHCPhysics/TtbarNNLO*.

[30] The D0 Collaboration. Observation of single top-quark production. *Phys. Rev. Lett.*, 2009.

[31] G. Degrassi et al. Higgs Mass and Vacuum Stability in the Standard Model at NNLO. *JHEP*, 2012.

[32] The ATLAS Collaboration. Measurement of Spin Correlation in $t\bar{t}$ Production from pp Collisions at $\sqrt{s} = 7$ TeV using the ATLAS Detector. *ATLAS-CONF*, 2011.

[33] W. Bernreuther and Z. G. SI. Distributions and Correlations for Top Quark Pair Production and Decay at the Tevatron and LHC. *hep-ph*, 2010.

[34] Stefano Frixione, Paolo Nason, and Carlo Oleari. Matching NLO QCD computations with parton shower simulations: the POWHEG method. *JHEP*, 11:070, 2007.

[35] Simone Alioli, Paolo Nason, Carlo Oleari, and Emanuele Re. A general framework for implementing NLO calculations in shower Monte Carlo programs: the POWHEG BOX. *JHEP*, 06:043, 2010.

[36] David d'Enterria, Krisztian Krajczar, and Hannu Paukkunen. Top-quark production in proton-nucleus and nucleus-nucleus collisions at LHC energies and beyond. *Phys. Lett.*, B746:64–72, 2015.

[37] CMS Collaboration. Projections for Heavy Ions with HL-LHC. CMS Physics Analysis Summary CMS-PAS-FTR-13-025, 2013.

[38] G. Aad et al. The ATLAS Experiment at the CERN Large Hadron Collider. *JINST*, 3:S08003, 2008.

[39] S. Chatrchyan et al. The CMS experiment at the CERN LHC. *JINST*, 3:S08004, 2008.

[40] ALICE Collaboration. The CMS experiment at the CERN LHC. *J. Instrum.*, 3, 2008.

[41] LHCb Collaboration. The LHCb Detector at the CERN LHC. *J. Instrum.*, 3, 2008.

[42] H. Geiger E. Rutherford and J. Harling. An Electrical Method of Counting the Number of α Particles from Radio-Active Substances. *Royal Society of London Proceedings Series A, vol. 81, pp. 141−161*, Aug. 1908.

[43] F. Sauli. Gaseous radiation detectors: fundamentals and applications. *Cambridge monographs on particle physics, nuclear physics and cosmology, Cambridge: Cambridge Univ. Press*, 2014.

[44] G. Charpak et al. The use of multiwire proportional counters to select and localize charged particles. *Nuclear Instruments and Methods, vol. 62, no. 3, pp. 262 − 268*, 1968.

[45] E. Cerron Zeballos et al. High Rate Resistive Plate Chambers. *Nucl. Instr. and Meth. A 367 388−393*, 1995. `https://edms.cern.ch/nav/CERN-0000011111`.

[46] K. Olive et al. Review of Particle Physics 2014-2015. *Chin. Phys. C, vol. 38, p. 090001*, 2014.

[47] M. Abbrescia et al. The simulation of resistive plate chambers in avalanche mode: Charge spectra and efficiency. *Nucl. Instrum. Meth., vol. A431, pp. 413 − 427*, 1999.

[48] A. Fridman and L. A. Kennedy. Plasma Physics and Engineering. *Taylor and Francis, New York.*

[49] C. Lippmann W. Riegler and R. Veenhof. Detector physics and simulation of resistive plate chambers. *Nucl. Instrum. Meth., vol. A500, pp. 144−162*, 2003.

[50] S. Ramo. Currents induced by electron motion. *Proceedings of the IRE, vol. 27, pp. 584 − 585*, Sept. 1939.

[51] M. Abbrescia et al. Resistive plate chambers performances at cosmic rays fluxes. *Nucl. Instrum. Meth., vol. A359, pp. 603 − 609*, 1995.

[52] M. Abbrescia et al. Resistive plate chambers performances at low pressure. *Nucl. Instrum. Meth., vol. A394, pp. 341− 348*, 1997.

[53] G. Pugliese. The RPC System for the CMS Experiment. *IEEE Conference, San Diego*, November 2006.

[54] M.Abbrescia et al. Effect of the Linseed Oil Treatment on the Performance of the Resistive Plate Counters. *CMS NOTE-1997/018*, 1997.

[55] J. Shiers. The Worldwide LHC Computing Grid (worldwide LCG). *Computer Physics Communications 177, 219 - 223 (2007), no. 1-2.*

[56] G. Pugliese on behalf of the CMS Collaboration. The RPC system for the CMS experiment. *2006 IEEE Nuclear Science Symposium Conference Record.*

[57] M. Abbrescia et al. Properties of $C_2H_2F_4$ based gas mixtures for avalanche mode operation of Resistive Plate Chambers. *CMS Note 97/004*, 1997.

[58] P.Camarri et al. Streamer suppression with SF6 in RPCs operated in avalanche mode. *Nucl. Instr. and Meth. A 414*, 1998.

[59] G. Iasselli et al. Study of the detailed Geometry of the Barrel RPC Strips. *CMS IN 2000/044.*

[60] J. Krolikowski et al. Acceptance of the Baseline and Modified RPC System Geometry. *CMS IN 2001/026.*

[61] CMS Collaboration. The performance of the CMS muon detector in proton-proton collisions at $\sqrt{s} = 7TeV$ at the LHC. *JINST 8 P11002 [arXiv:1306.6905]*, 2013.

[62] Camilo Andrés Carrillo Montoya. Search for Heavy Stable Charged Particles in the CMS Experiment using the RPC Detectors. *Andes U., Bogota, CMS-TS-2011-018, CERN-THESIS-2011-032*, 2010.

[63] http://cmssw.cvs.cern.ch/cgi-bin/cmssw.cgi/CMSSW/RecoLocalMuon/RPCRecHit/.

[64] M.A. Shah [CMS Collaboration]. Performance of CMS Resistive Plate Chambers in CRAFT and early 2015 collisions at 13 TeV. *CMS DP-2015/032*, 2015.

[65] G. Abbiendi et al. Muon Reconstruction in the CMS Detector. *CMS AN-2008/097*, 2008.

[66] C. Camilo [CMS Collaboration]. The CMS Resistive Plate Chambers system-detector performance during 2011. *WSPC, 10.1142/9789814405072-0068.*, 2012.

[67] M. Abbrescia [CMS Collaboration]. Cosmic ray test of double-gap resistive plate chambers for the CMS experiment. *Nucl. Instrum. Meth. A550 116*, 2005.

[68] CMS Collaboration. Operation, performance and upgrade of the CMS Resistive Plate Chamber system at LHC. *Nucl. Instrum. Meth. A 732 195*, 2013.

[69] Costantini et al. Uniformity and Stability of the CMS RPC Detector at the LHC. *PoS(RPC2012)005 [JINST 8 P03017] arXiv:1209.1989*, 2013.

[70] CMS Collaboration. The CMS muon project :Technical Design Report. *CERN-LHCC-97-032.*, 1997.

[71] M.A. Shah M.I. Pedraza-Moralesb and M. Shopova. First results of CMS RPC performance at 13 TeV. *JINST 11 C12003*, 2016.

[72] CMS Luminosity Calibration for the pp Reference Run at $\sqrt{s} = 5.02$ TeV. Technical Report CMS-PAS-LUM-16-001, CERN, 2016.

[73] Torbjörn Sjöstrand, Stephen Mrenna, and Peter Skands. PYTHIA 6.4 physics and manual. *JHEP*, 05:026, 2006.

[74] Torbjörn Sjöstrand, Stefan Ask, Jesper R. Christiansen, Richard Corke, Nishita Desai, Philip Ilten, Stephen Mrenna, Stefan Prestel, Christine O. Rasmussen, and Peter Skands. An introduction to $PYTHIA$8.2. *Comput. Phys. Commun.*, 191:159, 2015.

[75] Peter Skands, Stefano Carrazza, and Juan Rojo. Tuning PYTHIA 8.1: the Monash 2013 Tune. *Eur. Phys. J. C*, 74(8), 2014.

[76] J. Alwall, R. Frederix, S. Frixione, V. Hirschi, F. Maltoni, O. Mattelaer, H.-S. Shao, Stelzer T., P. Torrielli, and M. Zaro. The automated computation of tree-level and next-to-leading order differential cross sections, and their matching to parton shower simulations. *JHEP*, 07:079, 2014.

[77] Rikkert Frederix and Stefano Frixione. Merging meets matching in MC@NLO. *JHEP*, 12:061, 2012.

[78] Kirill Melnikov and Frank Petriello. Electroweak gauge boson production at hadron colliders through $O(\alpha_s^2)$. *Phys. Rev. D*, 74:114017, 2006.

[79] Simone Alioli, Paolo Nason, Carlo Oleari, and Emanuele Re. NLO single-top production matched with shower in POWHEG: s- and t-channel contributions. *JHEP*, 09:111, 2009. [Erratum: 10.1007/JHEP02(2010)011].

[80] Emanuele Re. Single-top Wt-channel production matched with parton showers using the POWHEG method. *Eur. Phys. J. C*, 71:1547, 2011.

[81] Nikolaos Kidonakis. Top Quark Production. In *Proceedings, Helmholtz International Summer School on Physics of Heavy Quarks and Hadrons (HQ 2013)*, page 139, Hamburg, 2014. Verlag Deutsches Elektronen-Synchrotron.

[82] John M. Campbell and R. K. Ellis. for the Tevatron and the LHC. *Nucl. Phys. Proc. Suppl.*, 205:10, 2010.

[83] S. Agostinelli et al. – a simulation toolkit. *Nucl. Instrum. Meth. A*, 506:250, 2003.

[84] Michal Czakon and Alexander Mitov. Top++: a program for the calculation of the top-pair cross-section at hadron colliders. *Comput. Phys. Commun.*, 185:2930, 2014.

[85] Jorg Wenninger and Ezio Todesco. Large Hadron Collider momentum calibration and accuracy. Technical Report CERN-ACC-2017-0007, CERN, Geneva, Feb 2017.

[86] CMS Collaboration. Particle-flow event reconstruction in cms and performance for jets, taus, and . CMS Physics Analysis Summary CMS-PAS-PFT-09-001, 2009.

[87] Vardan Khachatryan et al. Performance of electron reconstruction and selection with the CMS detector in proton-proton collisions at $\sqrt{s} = 8\,\text{TeV}$. *JINST*, 10:P06005, 2015.

[88] Serguei Chatrchyan et al. Performance of CMS muon reconstruction in *pp* collision events at $\sqrt{s} = 7\,\text{TeV}$. *JINST*, 7:P10002, 2012.

[89] Serguei Chatrchyan et al. The performance of the CMS muon detector in proton-proton collisions at $\sqrt{s} = 7\,TeV$ at the LHC. *JINST*, 8:P11002, 2013.

[90] Matteo Cacciari, Gavin P. Salam, and Gregory Soyez. The anti-k_{T} jet clustering algorithm. *JHEP*, 04:063, 2008.

[91] Matteo Cacciari, Gavin P. Salam, and Gregory Soyez. FastJet user manual. *Eur. Phys. J. C*, 72:1896, 2012.

[92] Vardan Khachatryan et al. Measurements of inclusive W and Z cross sections in pp collisions at $\sqrt{s} = 7\,TeV$. *JHEP*, 01:080, 2011.

[93] S. Chatrchyan et al. Determination of jet energy calibration and transverse momentum resolution in CMS. *JINST*, 6:P11002, 2011.

[94] Vardan Khachatryan et al. First Measurement of the Cross Section for Top-Quark Pair Production in Proton-Proton Collisions at $\sqrt{s} = 7$ TeV. *Phys. Lett.*, B695:424–443, 2011.

[95] Manuel Bähr, Stefan Gieseke, Martyn A. Gigg, David Grellscheid, Keith Hamilton, Oluseyi Latunde-Dada, Simon Plätzer, Peter Richardson, Michael H. Seymour, Alexander Sherstnev, and Bryan R. Webber. $HERWIG{+}{+}$ physics and manual. *Eur. Phys. J. C*, 58:639, 2008.

[96] Glen Cowan, Kyle Cranmer, Eilam Gross, and Ofer Vitells. Asymptotic formulae for likelihood-based tests of new physics. *Eur.Phys.J.*, C71:1554, 2011.

[97] Andrea Valassi and Roberto Chierici. Information and treatment of unknown correlations in the combination of measurements using the BLUE method. *Eur. Phys. J.*, C74:2717, 2014.

[98] Luca Lista. The bias of the unbiased estimator: a study of the iterative application of the BLUE method. *Nucl. Instrum. Meth.*, A764:82–93, 2014. [Erratum: Nucl. Instrum. Meth.A773,87(2015)].

[99] H. Abramowicz et al. Combination of measurements of inclusive deep inelastic $e^{\pm}p$ scattering cross sections and QCD analysis of HERA data. *Eur. Phys. J. C*, 75:580, 2015.

[100] Vardan Khachatryan et al. Measurement of the differential cross section and charge asymmetry for inclusive pp $\rightarrow W^{\pm} + X$ production at $\sqrt{s} = 8$ TeV. *Eur. Phys. J.*, C76(8):469, 2016.

[101] S. Alekhin et al. HERAFitter, Open source QCD fit project. *Eur. Phys. J. C*, 75:304, 2015.

[102] `http://www.xfitter.org`.

[103] V. N. Gribov and L. N. Lipatov. Deep inelastic ep scattering in perturbation theory. *Sov. J. Nucl. Phys.*, 15:438, 1972.

[104] Guido Altarelli and G. Parisi. Asymptotic freedom in parton language. *Nucl. Phys. B*, 126:298, 1977.

[105] G. Curci, W. Furmanski, and R. Petronzio. Evolution of parton densities beyond leading order: The non-singlet case. *Nucl. Phys. B*, 175:27, 1980.

[106] W. Furmanski and R. Petronzio. Singlet parton densities beyond leading order. *Phys. Lett. B*, 97:437, 1980.

[107] S. Moch, J. A. M. Vermaseren, and A. Vogt. The three-loop splitting functions in QCD: the non-singlet case. *Nucl. Phys. B*, 688:101, 2004.

[108] A. Vogt, S. Moch, and J. A. M. Vermaseren. The three-loop splitting functions in QCD: the singlet case. *Nucl. Phys. B*, 691:129, 2004.

[109] M. Botje. QCDNUM: Fast QCD evolution and convolution. *Comput. Phys. Commun.*, 182:490, 2011.

[110] M. Aliev, H. Lacker, U. Langenfeld, S. Moch, P. Uwer, and M. Wiedermann. HATHOR: HAdronic Top and Heavy quarks crOss section calculatoR. *Comput. Phys. Commun.*, 182:1034–1046, 2011.

[111] A. D Martin, W. J. Stirling, R. S. Thorne, and G. Watt. Parton distributions for the LHC. *Eur. Phys. J. C*, 63:189, 2009.

[112] Serguei Chatrchyan et al. Measurement of the muon charge asymmetry in inclusive pp $\rightarrow$ W + X production at $\sqrt{s} = 7\,TeV$ and an improved determination of light parton distribution functions. *Phys. Rev. D*, 90:032004, 2014.

[113] Walter T. Giele and Stephane Keller. Implications of hadron collider observables on parton distribution function uncertainties. *Phys. Rev. D*, 58:094023, 1998.

[114] Walter T. Giele, Stephane A. Keller, and David A. Kosower. Parton distribution function uncertainties. 2001.

[115] Silva, P. and Hassan, Q. Topljets2015 github repository. github repository, 2015.

[116] CMS Collaboration. Underlying event tunes and double parton scattering. CMS Physics Analysis Summary CMS-PAS-GEN-14-001, 2016.

[117] Federico Demartin, Stefano Forte, Elisa Mariani, Juan Rojo, and Alessandro Vicini. The impact of PDF and alphas uncertainties on Higgs Production in gluon fusion at hadron colliders. *Phys. Rev. D*, 82, 2010.

[118] S. Agostinelli et al. GEANT4: A simulation toolkit. *Nucl. Instrum. Meth.*, A506:250–303, 2003.

[119] K. Mishra et al. Tag and probe. twiki, 2014.

[120] Electron reconstruction and identification for pbpb and reference pp collisions at 5 TeV. *CMS Analysis Note*, AN2016-110, 2016.